RUPRECHT-KARLS-UNIVERSITÄT HEIDELBERG

Gabriel Anders

Absolute luminosity determination for the ATLAS experiment

Dissertation

HD-KIP 13-21

KIRCHHOFF-INSTITUT FÜR PHYSIK

Dissertation

submitted to the
Combined Faculties of the Natural Sciences and Mathematics
of the Ruperto-Carola-University of Heidelberg, Germany
for the degree of

Doctor of Natural Sciences

Put forward by

Dipl. Phys. Gabriel Anders
born in Waldbröl, Germany

Oral examination: July 25, 2013

Absolute luminosity determination for the ATLAS experiment

Referees: Prof. Dr. Hans-Christian Schultz-Coulon
Dr. Thilo Pauly

Zusammenfassung

ATLAS ist eines der vier großen Experimente am Large Hadron Collider (LHC). Präzise Messungen von Wirkungsquerschnitten erfordern eine genaue Kenntnis der integrierten Luminosität. Die relative Luminosität wird mit verschiedenen Detektoren und Algorithmen gemessen. Letztere wandeln die von den Detektoren gemessenen Raten in eine zur Luminosität proportionale Größe um. In dieser Arbeit werden drei Algorithmen kalibriert, die auf den zwei primären Luminositäts-Detektoren basieren: BCMH_EventOR, BCMV_EventOR und LUCID_EventOR. Die Kalibrierung beruht auf Van der Meer (VdM) Scans, die in den Monaten Juli und November 2012 durchgeführt wurden. Die statistischen Fehler dieser Methode sind klein und die Genauigkeit ist durch systematische Unsicherheiten begrenzt, welche abgeschätzt werden. Die Kalibrierungskonstanten der Juli VdM Scans haben eine Unsicherheit von 5.40 %, die der November Scans eine von 2.50 %. Die November-Kalibrierung ist die Grundlage zur Bestimmung der integrierten Luminosität, deren Unsicherheit auf 3.30 % geschätzt wird. Die vorläufige offizielle ATLAS Luminosität und deren Unsicherheit für Proton-Proton Kollisionen bei $\sqrt{s} = 8\,\text{TeV}$ im Jahr 2012 basieren auf dieser Arbeit.

Summary

ATLAS is one of the four big experiments at the Large Hadron Collider (LHC). In order to accurately measure cross sections, the precise knowledge of the integrated luminosity is a prerequisite. The relative luminosity is measured with various detectors and algorithms. The purpose of the algorithms is to convert raw rates measured by a detector into a quantity which is proportional to the luminosity. In this work, three algorithms linked to the two main ATLAS luminosity detectors are absolutely calibrated: BCMH_EventOR, BCMV_EventOR, and LUCID_EventOR. The determination of the calibration constants is based on Van der Meer (VdM) scans, which were carried out in July and November 2012. The statistical errors of this method are negligible and the precision is limited by systematic uncertainties. The different uncertainty sources are quantitatively estimated. The overall uncertainty on the calibration constants is estimated to be 5.40 % for the July VdM scans and 2.50 % for the November VdM scans. The November calibration is used to determine the integrated luminosity in 2012, its overall uncertainty is evaluated to be 3.30 %. The preliminary official ATLAS luminosity and its uncertainty for proton-proton collisions at $\sqrt{s} = 8\,\text{TeV}$ in the year 2012 are based on this work.

Contents

1. Introduction

In order to find answers to some of the main open questions of particle physics, accelerators are employed for colliding particles at unprecedented centre of mass energies. In the year 2012, the Large Hadron Collider (LHC) at CERN near Geneva achieved proton-proton collisions at centre of mass energies of up to 8 TeV. The analysis of the collisions delivers insights into the characteristics of subatomic particles and the forces acting on them.

The theory concerned with the description of these basic interactions is called the Standard Model of particle physics (SM). The interactions are described by three fundamental forces: the electromagnetic, weak and strong force. The electromagnetic force is mediated by photons, the weak force by the W^+, W^-, and Z boson, and the strong force by gluons. It was developed during the last decades and its quantitative predictions were verified in numerous experiments. The recent discovery of a new particle at the LHC, consistent with the Higgs boson, is one of the major successes of particle physics [1, 2]. It was the last missing piece of the SM and mediates the interaction of particles with the Higgs field, thus giving them mass.

Even though the SM can predict many features of subatomic particles to a high precision, it can not explain the existence of dark matter[1] and has a high number of free parameters[2]. The search for new physics phenomena beyond the Standard Model (BSM) is one of the primary goals of the LHC experiments, one of them being the ATLAS experiment.

The number of the inelastic proton-proton interactions occurring in a detector is proportional to a quantity called luminosity. The luminosity is a measure for the ability of an accelerator to produce particle interactions. While the instantaneous luminosity is an important parameter for the operation of the LHC and the detectors, the precise knowledge of the integrated luminosity is a prerequisite for accurate cross section measurements corresponding to an interaction process.

Many possible new BSM physics phenomena are predicted to enhance certain process cross sections, thus searches for new phenomena are often based on comparisons of mea-

[1] The properties of dark matter were derived from observational cosmology.
[2] The free SM parameters were experimentally determined with a high precision.

sured cross sections to the ones predicted by the SM. The sensitivity of these searches depends directly on the precision of the integrated luminosity. Furthermore, accurate experimental cross sections decrease the theoretical uncertainties on cross section calculations via confining the uncertainties on the input parameters of the calculations [3].

In the ATLAS experiment, the relative luminosity is measured with various detectors and algorithms. The purpose of luminosity algorithms is to convert raw rates measured by a detector into a quantity which is proportional to the luminosity. The redundancy from having multiple independent measurements allows detailed studies of systematic uncertainties.

The topic of this thesis is the absolute luminosity calibration of three algorithms linked to the two main luminosity detectors: BCM[3] and LUCID[4]. The former was built primarily for monitoring the beam background, while the latter is a dedicated luminosity detector. The calibration procedure is based on Van der Meer (VdM) scans. An integral part of the scans is to measure the dependency of the interaction rate on the transverse beam separation.

Chapter 2 of this thesis gives a brief overview of the LHC and the four main experiments. Chapter 3 introduces the ATLAS detector, the main subdetectors and the trigger and data acquisition system. Special focus is given to the detectors employed for luminosity measurements.

The concept of luminosity is introduced in chapter 4. Different ways to measure luminosity are presented. The theory of VdM scans is derived in chapter 5. Chapter 6 highlights the instrumentation of importance for VdM scans.

The analysis of the 2012 VdM scans is carried out in chapter 7. The central calibration constants are determined and the systematic uncertainties impacting the calibration precision are estimated.

Chapter 8 presents a partially complementary method to the common VdM scan procedure which is based on reconstructed interaction vertices.

Chapter 9 covers the determination of the integrated luminosity in ATLAS and its uncertainty. The main results are summarised in chapter 10.

[3] *Beam Condition Monitor*
[4] *LUminosity measurement using Cerenkov Integrating Detector*

2. The Large Hadron Collider

The Large Hadron Collider (LHC) is a circular particle accelerator at CERN[1] near Geneva which collides bunches of protons. Since one of its primary goals is the search for new physics, the LHC is designed for unprecedented centre of mass energies of 14 TeV. The nominal design number of protons per bunch is $1.15 \cdot 10^{11}$, the nominal design peak luminosity is $10^{34}\,\mathrm{cm}^{-2}\mathrm{s}^{-1}$. The time between successive bunch collisions is designed to be 25 ns.

By the end of the year 2012, the LHC reached a maximum energy of 4 TeV per beam and was operated with a bunch spacing of 50 ns. After an approximately two year long shutdown required for maintenance and upgrades, the LHC will increase the energy per beam to 6.5 TeV or 7 TeV.

The LHC was built in an already existing tunnel which former accommodated the Large Electron-Positron Collider. It has a circumference of 26.7 km and is located between 45 m and 170 m below ground level. A schematic layout of the LHC is shown in figure 2.1. The LHC is divided into octants, each of which contains a straight section of approximately 528 m length. Interjacent arcs connect the straight sections among each other. Because the counter-rotating beams require opposite dipole fields, they circulate in two separate rings.

Prior to injection into the LHC, the proton bunches run through an injection chain consisting of several accelerators which have different energy ranges and successively increase the proton energy. When the proton bunches have obtained an energy of 450 GeV, they are injected into the LHC. After completion of the injection sequence, the LHC accelerates the protons to maximum energy. Once the proton bunches have obtained the maximum energy, the beams are brought into collision at four different interaction points (IP), also known as insertions.

Two high luminosity insertions provide collisions for the ATLAS experiment (Point 1) and for the CMS experiment (Point 5). Both insertions are similarly constructed except that the beams at Point 1 cross in the vertical plane, whereas they cross in the horizontal plane at Point 5. Point 1 and 5 sit at exactly opposite locations of the ring, hence particle

[1] European Organisation for Nuclear Research, founded in 1954.

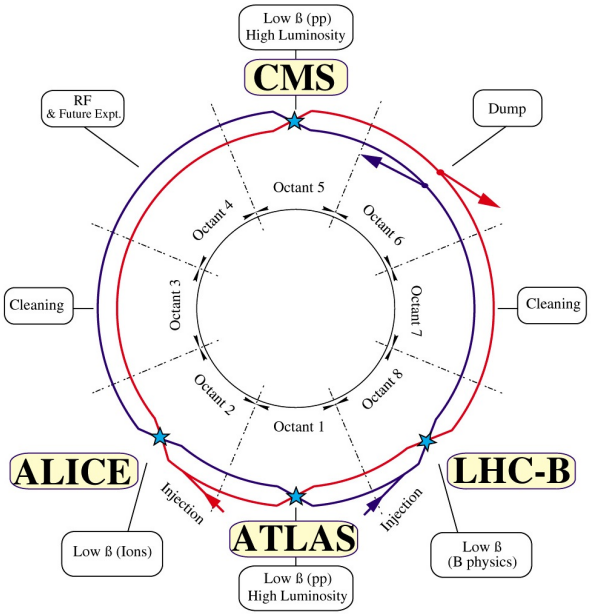

Figure 2.1.: Layout of the LHC machine [4]

bunches colliding in ATLAS also collide in the CMS experiment and vice versa. The other two experimental insertions provide collisions for the ALICE (Point 2) and the LHCb experiment (Point 8).

Due to the proton-proton collisions and other beam losses, the number of circulating protons and hence the interaction rates at the IPs slowly decrease over time. Once they drop below a given threshold, the beams are extracted from the LHC in order to inject new proton bunches. A cycle of injection, energy ramp-up and collision of the beams is referred to as an LHC fill. Each fill is identified by a unique integer number. The duration of a fill is typically a few hours.

The main limiting factor in the LHC energy is the magnetic field required to keep the particles on track within the beam pipe. The 1232 main LHC dipoles must maintain a magnetic field of 8.33 T at peak energy. The high currents require superconducting magnets which are operated at a temperature below 2 K. At Point 4, the protons are accelerated by a radio frequency (RF) acceleration system made up of two independent sets of cavities per beam. The cavities operate at a frequency of 400.8 MHz. Combined with the revolution frequency of 11.245 kHz, this results in 35640 different locations (RF buckets) around the ring which can be occupied by proton bunches [5]. Only every tenth RF bucket is filled, hence 3564 possible bunch positions exist. Further operational constraints limit the maximum number of bunches to 2808.

Due to the high stored energy, the beams can cause severe damage in case the magnet

system breaks down. As a safety precaution or at the end of a fill, the beams can be extracted within a short time to an external absorber by the beam dumping system. To allow for a loss-free extraction of the beams, the circulating bunches must have a sufficiently wide gap during which fast extraction kicker magnets can ramp up their magnetic fields. The beam dump is located at Point 6. The description of the LHC given here is based on [6] and [7].

The four main experiments pursue different goals, which in the following are briefly summarised :

- ALICE[2] is optimised for heavy ion collisions and aims at studying the properties of strongly interacting matter at high energy densities [8].
- ATLAS[3] is a general purpose detector designed for searching for physics beyond the Standard Model and the Higgs boson [9].
- CMS[4] pursues the same goals as ATLAS. It shall give independent measurements and enables crosschecks between both experiments [10].
- LHCb[5] aims at studying decays containing b-quarks in order to precisely measure the nature of CP violation [11].

[2] *A Large Ion Collider Experiment*
[3] *A Toroidal LHC ApparatuS*
[4] *Compact Muon Solenoid*
[5] *Large Hadron Collider beauty*

3. The ATLAS experiment

This chapter gives a general overview of the ATLAS detector, its main subdetectors and the performance requirements motivated by its physics programme. The trigger and data acquisition system is introduced, followed by a discussion of the main luminosity detectors.

3.1. The ATLAS detector

The ATLAS detector is a general purpose detector optimised for studying proton-proton collisions at instantaneous luminosities of $10^{34}\,\mathrm{cm}^{-2}\mathrm{s}^{-1}$. The detector was designed and built in a collaboration of several thousand people over a period of fifteen years. The design was driven by the goal to observe new physics phenomena and to probe the predictions of the Standard Model of particle physics in the TeV energy regime. The main performance benchmark was the search for the Standard Model Higgs boson.

Coordinate system and nomenclature

The origin of the right-handed ATLAS coordinate system is given by the nominal interaction point. The beam axis defines the z axis and its positive part is pointing to the A-side; consequently, the C-side has negative z coordinates. The x-y plane is the plane orthogonal to the beam axis. The positive x axis is pointing from the nominal interaction point to the centre of the LHC ring. The positive y axis is pointing from the interaction point upwards. The azimuthal angle ϕ defines the direction in the x-y plane and the polar angle θ is given with respect to the beam axis. The definition of the pseudorapidity η is $-\ln\tan(\theta/2)$. Within the ATLAS experiment, the 3564 different LHC bunch positions are labelled consecutively by integer values called BCIDs[1].

[1] *Bunch Crossing IDentifier*

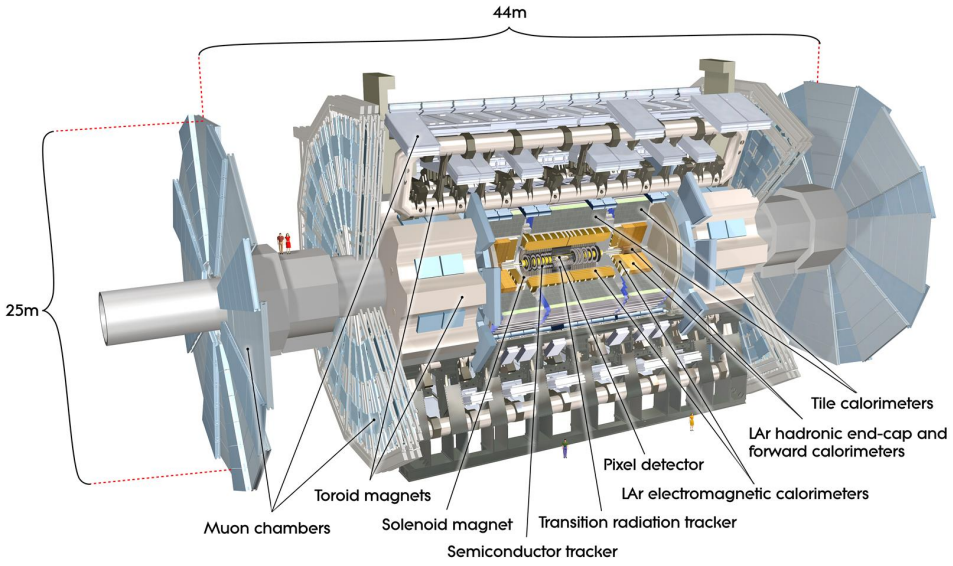

Figure 3.1.: Schematic view of the ATLAS detector [12]

General performance requirements

In accordance with the physics goals one can derive a set of basic requirements [9]. In order to fully reconstruct the inelastic proton-proton interactions, the detector must have a broad acceptance range in azimuthal angle and pseudorapidity. Furthermore, it needs good momentum-resolution for charged particles and a high reconstruction efficiency of the inner tracking system. In order to identify secondary vertices caused by long-lived b-quarks and to identify τ-leptons, the tracking system must have detectors close to the interaction region. To identify and measure electrons and photons as well as jets and missing transverse energy, the detector must have electromagnetic and hadronic calorimetry components with high angular acceptance and good energy (E) resolution. A good identification of muons and the precise measurement of their transverse momentum (p_T) over a broad momentum range is important for the study of many physics processes. For the same reason, the charge identification for high transverse momentum muons is required to be reliable.

An efficient trigger system with high background rejection is crucial for the detection of processes involving low transverse momentum particles. At nominal luminosity, approximately 10^9 inelastic interactions take place every second. In each bunch collision many different proton-proton interactions may occur, called in-time pile-up. In order to be able to attribute all detector signals to the correct interaction, the detector must have a fine granularity. To minimise the effect of overlapping detector signals originating from

	Resolution	η **coverage**
Inner detector	$\sigma_{p_T}/p_T = 0.05\% p_T \oplus 1\%$	± 2.5
Electromagnetic calorimetry	$\sigma_E/E = 10\%/\sqrt{E} \oplus 0.7\%$	± 3.2
Hadronic calorimetry		
barrel and end-cap	$\sigma_E/E = 50\%/\sqrt{E} \oplus 3\%$	± 3.2
forward	$\sigma_E/E = 100\%/\sqrt{E} \oplus 10\%$	$3.1 < \lvert\eta\rvert < 4.9$
Muon spectrometer	$\sigma_{p_T}/p_T = 10\%$ at $p_T = 1\,\mathrm{TeV}$	± 2.7

Table 3.1.: Performance requirements for the main ATLAS subdetectors [9].

consecutive BCIDs, called out-of-time pile-up, the subdetectors are required to possess fast electronics. Additionally, due to the high particle flux, the subdetector electronics must be radiation-hard.

Detector overview

Figure 3.1 illustrates the structure and dimensions of the ATLAS detector. It has a length of 44 m, a diameter of 25 m and is symmetric with respect to the plane perpendicular to the beam direction. The most inner component is the inner detector which carries out the particle tracking and comprises several layers of semiconductor pixel and strip detectors as well as straw-tube tracking detectors. The calorimetry is based on liquid argon (LAr) and scintillator-tile sampling calorimeters. It has barrel components covering the central region and end-cap and forward components covering regions of higher pseudorapidity. The calorimetry is surrounded by a muon spectrometer which is immersed in a toroidal magnetic field and accounts for the overall detector dimensions. The required resolution and angular coverage of the main sub-systems are listed in table 3.1.

In the subsequent paragraphs, the main detector components are described in more detail based on [9].

The magnet system

The ATLAS magnet system is made up of four superconducting magnet systems. A solenoid encloses the inner detector and creates an axial magnetic field of 2 T. The axial length of the solenoid is 5.8 m, the inner diameter is 2.46 m, the outer 2.56 m. In order to enable a good performance of the calorimeters, the radiative thickness of the solenoid was minimised. The magnetic flux on the outer side of the solenoid returns through elements of the hadronic calorimeters. The magnetic fields required by the muon system

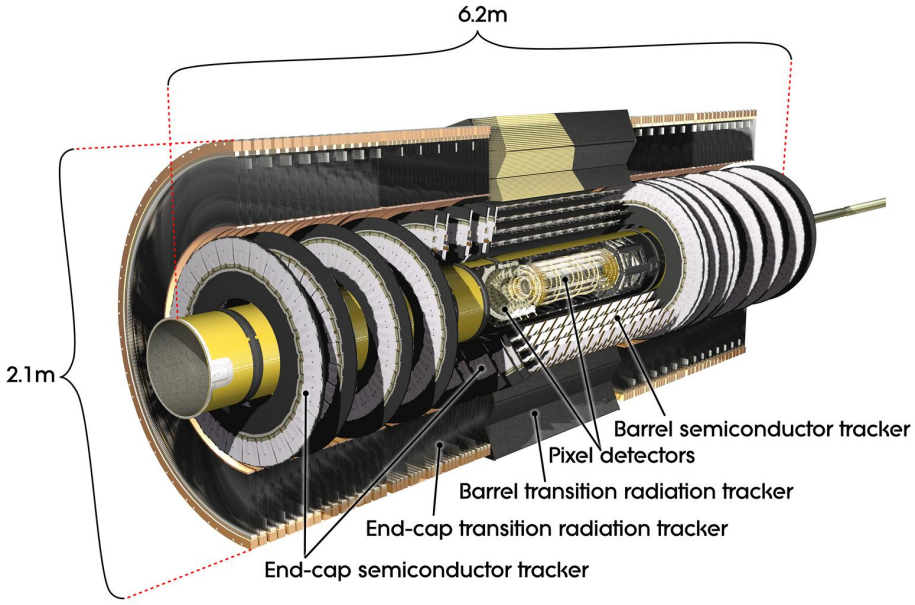

Figure 3.2.: Schematic view of the inner detector [12]

are created by one barrel and two end-cap toroids. The barrel toroid provides a magnetic field of 0.5 T in the central region, while the end-cap toroids produce magnetic fields of 1 T in the more forward region. The magnet system has a length of 26 m and a diameter of 22 m.

The inner detector

The inner detector measures particle tracks. At nominal LHC luminosity, about a thousand particles are expected within $|\eta| < 2.5$ in each bunch crossing. The high particle flux and the proximity to the interaction region require a fine granularity as well as fast electronics with high resistance to radiation damage. The inner detector measures the transverse momentum and identifies primary and secondary vertices for charged particles with $p_T > 0.5\,\text{GeV}$ and $|\eta| < 2.5$. Charged particles with $|\eta| < 2.0$ are identified as electrons over a broad energy range. A schematic view of the inner detector is shown in figure 3.2. The innermost component is the high-resolution pixel detector. Further out is the Semiconductor Tracker (SCT) which is surrounded by the Transition Radiation Tracker (TRT). The pixel detector and the SCT cover the region $|\eta| < 2.5$ over the full azimuthal angle, both are built up of barrel and end-cap components. All three systems are independent.

The pixel detector comprises three barrel layers and three end-cap disks on either side

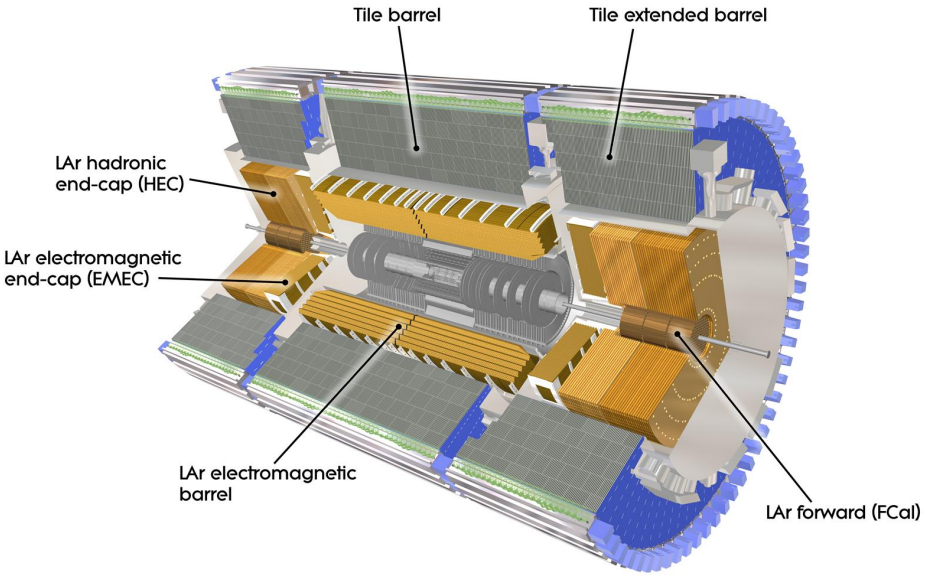

Figure 3.3.: Schematic view of the calorimetry [12]

of the IP. A charged particle typically causes three hits, thus giving three space points. The barrel layers have an accuracy of 10 μm (R-ϕ) and 115 μm (z), the disks have an accuracy of 10 μm (R-ϕ) and 115 μm (R). The pixel detector has the finest granularity among the three inner detector subsystems and possesses 80.4 million readout channels.

The SCT comprises four barrel layers and nine end-cap disks on either side of the IP. A particle typically leaves four space points, each of which is defined by hits in two adjacent strip layers which are rotated by ninety degrees with respect to each other. The barrel layers have an accuracy of 17 μm (R-ϕ) and 580 μm (z), the disks have an accuracy of 10 μm (R-ϕ) and 580 μm (R). The SCT possesses 6.3 million readout channels.

The TRT covers tracks in the region $|\eta| < 2.0$ and is equipped with straw tubes of 4 mm diameter. The straw tubes run parallel to the beam axis in the barrel region and are placed radially in higher pseudorapidity regions. A charged particle typically hits 36 straw tubes, each of which has an accuracy of 130 μm in R-ϕ. The space points measured at high radii significantly enhance the precision of the momentum measurements. The detection of transition-radiation photons improves the identification of electrons. The TRT possesses 0.35 million readout channels.

The calorimeters

The calorimeter system surrounds the inner detector and carries out the identification and energy measurements of leptons, photons and jets. The calorimeters cover the region $|\eta| < 4.9$ and therefore enable the measurement of missing transverse energy with the precision required by the physics analyses. A schematic view of the calorimetry is shown in figure 3.3. The measurements in the central region, corresponding to the pseudorapidity coverage of the inner detector, have a higher precision than the ones at higher pseudorapidity values. The more inner components are electromagnetic calorimeters and fully absorb electromagnetic showers. Hadronic calorimeters are used further out and absorb hadronic showers. To ensure a clean measurement of muons, the penetration of electromagnetic and hadronic showers into the muon system must be avoided. This is also important for the reason, that leaking energy degrades the accuracy of the energy measurements. The containment of electromagnetic and hadronic showers within the calorimeters is ensured by the choice of appropriate radiation thicknesses. The latter are given in units of radiation lengths (X_0) and interaction lengths (λ). The electromagnetic calorimeter has a radiation thickness of at least 22 X_0 in the barrel and at least 24 X_0 in the end-caps. Taking the support structure into account, the total calorimeter thickness in the barrel and end-caps is about 11 λ.

Electromagnetic calorimeter

The EM calorimeter is a sampling calorimeter based on active layers of liquid argon (LAr) and lead absorber plates. The choice of LAr as active medium was motivated by its linear behaviour and radiation hardness. The latter ensures the stability of the detector response over time. To avoid azimuthal cracks in the acceptance, the geometry of the electrodes and absorber plates is accordion-like over the full η-coverage. The EM calorimeter comprises three components: one barrel component covers the central region $|\eta| < 1.475$ and two endcap wheels (EMEC) cover the region $1.375 < |\eta| < 3.2$. The barrel component is built up of two identical halves which are separated at $\eta = 0$ by a 4 mm wide gap. The end-cap wheels comprise an inner and outer wheel which cover the region $2.5 < |\eta| < 3.2$ and $1.375 < |\eta| < 2.5$, respectively.

The energy measurements for $|\eta| < 2.5$ are most precise, since in this region three active layers of LAr are employed, whereas two layers are used elsewhere. To correct for energy losses of central electrons and photons prior to the calorimeter system, a presampler system consisting of one active LAr layer was installed in the region $|\eta| < 1.8$.

Hadronic calorimeters

The hadronic calorimeter system is arranged around the electromagnetic one and employs different types of sampling calorimeters. The barrel part (TileCal) is divided into a central component covering $|\eta| < 1.0$ and two extended components covering $0.8 < |\eta| < 1.7$. All barrel components use scintillating tiles as active medium, interleaved with steel absorber plates. The scintillation photons are read out with wavelength-shifting fibres on the tile edges. Multiple fibres are grouped into pseudo-projective read-out cells with respect to the interaction region and are connected to photomultiplier tubes which produce electric signals proportional to the number of photons.

The end-cap components comprise the hadronic LAr end-cap calorimeter (HEC) and the LAr forward calorimeter (FCal). The former covers the region $1.5 < |\eta| < 3.2$, the latter $3.1 < |\eta| < 4.9$. The different components slightly overlap to ensure a homogeneous material density in pseudorapidity. The HEC employs copper as absorber material and consists of two disks on either side which are placed next to the EMEC. Each of the four disks is structured azimuthally in 32 wedges.

The FCal comprises three modules: the module closest to the interaction region is optimised for measurements of electromagnetic showers and uses copper as absorber material, the other two modules use tungsten as absorber material and measure hadronic showers. All three modules employ LAr as active medium.

The muon system

Muons have a much higher mass than electrons and lose less energy due to bremsstrahlung when traversing matter. Hence muons penetrate the inner detector and calorimetry nearly unaffected before they reach the muon system. A schematic view of the muon system is shown in figure 3.4. The bending of the muon trajectories in the toroidal magnetic field allows to measure the transverse momentum with a high precision. To achieve the desired performance, the magnetic field is as orthogonal as possible to the muon flight direction over a wide η-range. Design goal was a stand-alone measurement of the transverse momentum with a precision of 10 % for a 1 TeV muon and the ability to trigger on high transverse momentum muons. Muon tracks typically pass three stations equipped with muon chambers. The barrel chambers are installed on cylindrical shells around the beam axis and are aligned in parallel to the beam axis, the end-cap chambers are placed on wheels and are aligned perpendicular to the beam axis.

Subject to the requirements, the muon chambers are based on different technologies. Monitored Drift Tubes (MDTs) provide precision measurements in the bending plane with an accuracy of 35 μm per chamber over the range $|\eta| < 2.7$. The Cathode Strip

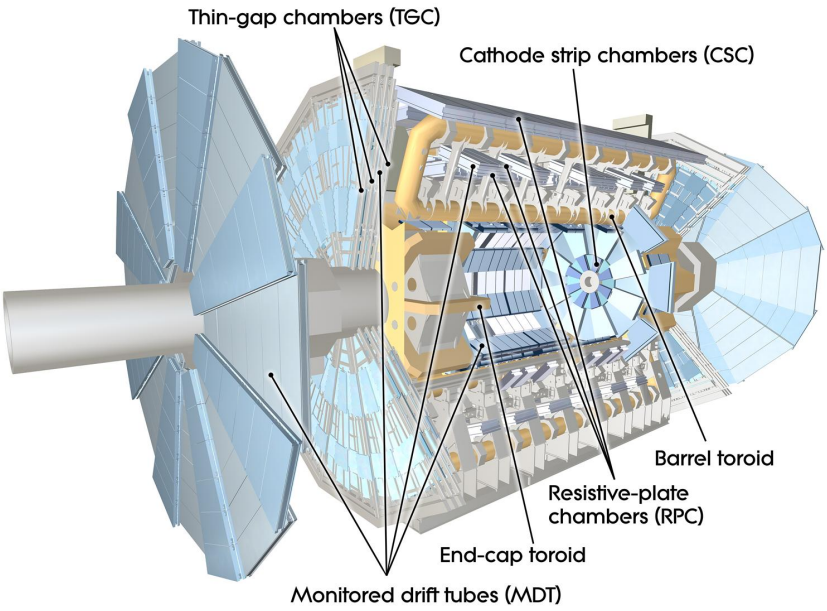

Figure 3.4.: Schematic view of the muon system [12]

Chambers (CSCs) are multiwire proportional chambers. They are used in the range $2 < |\eta| < 2.7$ because of the demanding background conditions. Each CSC has a precision of 5 mm in the non-bending plane and 40 μm in the bending plane. Fast Resistive Plate Chambers (RPCs) cover the range $|\eta| < 1.05$ and are used for triggering as well as for measuring the coordinate of muon tracks in the non-bending plane. Thin Gap Chambers (TGC) in the range $1.05 < |\eta| < 2.7$ serve the same purposes. The muon triggering is based on data from the region $|\eta| < 2.4$ only.

3.2. The trigger and data acquisition system

The high mean number of inelastic interactions per bunch crossing combined with the 40 MHz collision rate are a challenge for the trigger and data acquisition system. To select only the potentially interesting events for permanent storage and subsequent analysis, ATLAS makes use of a three-staged online filtering process, called triggering. A diagram of the trigger system is shown in figure 3.5.

The first stage trigger (Level-1) uses information of reduced granularity to decide within a latency of 2.5 μs whether an event is rejected or accepted. The latency is defined by the shortest front-end buffer length among the various subdetectors. Because of the strict timing requirements, the Level-1 trigger is made up of custom-built electronics. High transverse momentum muons are triggered using information from the RPCs and

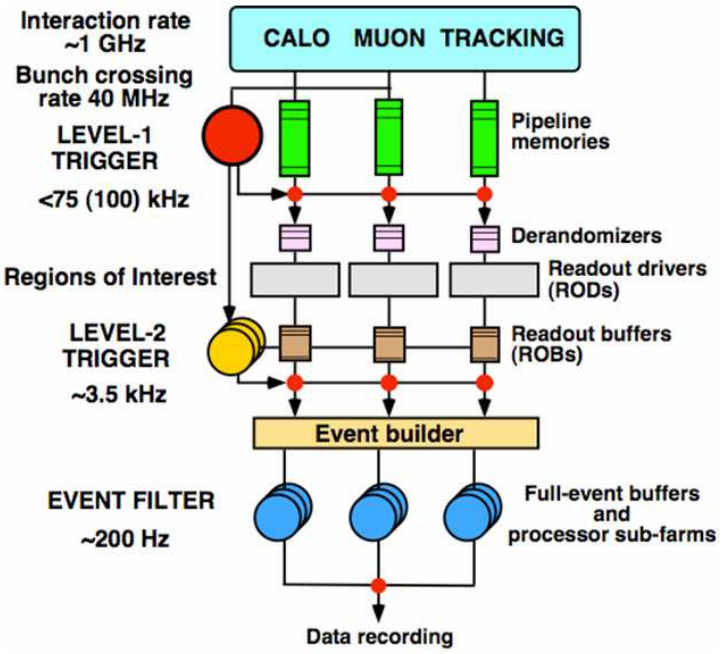

Figure 3.5.: Diagram of the three-staged ATLAS trigger [13]

TGCs. Triggers for electrons, photons, jets and τ-leptons are based on information from the calorimetry. The triggering on properties like missing transverse energy or high overall transverse energy is rendered possible by specialised hardware which sums up signals coming from different calorimeter regions. If an event is accepted, it is passed on to the second stage trigger (Level-2). The maximum Level-1 accept rate is 100 kHz and limited by the performance of the readout systems. During the year 2012, the Level-1 accept rate was typically about 75 kHz.

The Level-2 trigger decision is based on Region-of-Interests (RoIs) only; these are detector regions in which the Level-1 trigger found potentially interesting trigger objects. The RoI concept reduces the traffic between the Readout Systems (ROS) and the Level-2 processing units. The Level-2 trigger is implemented in software and uses the full data recorded in the RoIs. On average, events are processed within approximately 40 ms. The Level-2 output rate is about 3.5 kHz.

The final selection is done by the event filter which reconstructs the events based on the full detector data using offline algorithms. Like the Level-2 trigger, the event filter is implemented in software running on a computer farm. The events passing all selection criteria are permanently stored for offline analysis. Typically, each event is processed within four seconds. During the year 2012, the rate of recorded events was about 400 Hz, which is twice the value of the design specification.

3.3. Luminosity detectors and online infrastructure

This section introduces the ATLAS online infrastructure for luminosity measurements and gives an overview of the different subdetectors which are used to measure the luminosity.

Online luminosity infrastructure

The online luminosity infrastructure must fulfil two basic requirements: 1. it must monitor the luminosity in realtime, 2. for subsequent analysis and determination of the integrated luminosity it must permanently store the measured luminosity values. The realtime luminosity is important for bringing the beams into collision and for luminosity optimisations during the fills. Furthermore the realtime luminosity allows to set the trigger system configuration according to the rate of expected collision events.

In general, one has to distinguish between the delivered and the recorded luminosity: the delivered luminosity is the total integrated luminosity provided by the LHC and independent of the state of the ATLAS detector; the recorded luminosity is the integrated luminosity during which the ATLAS detector was fully operational and recorded collision data. Whereas the recorded luminosity is important for physics analyses, the ratio of recorded to delivered luminosity is an important value for quantifying the data taking efficiency. The main sources of inefficiencies are:

- Some of the subdetectors are fully operational with some delay only, after the LHC declares stable beams. One example is the inner detector, which does not ramp up its high voltage before the beams are well controlled. In that way, the risk of potential detector damage is minimised. The collisions, which have happened before the nominal voltage is reached, are lost for physics analyses.

- One of the subdetectors or parts of the data acquisition system fail during a fill. This can be due to a wrong configuration or a hardware-related issue.

- In order to protect the subdetector front-end buffers, the Level-1 trigger occasionally introduces trigger dead time. During the dead time no new events are accepted. There are three types of dead time: the simple dead time is introduced for a given number of bunch crossings after each triggered event and the complex dead time limits the overall number of triggered events in a given time interval. The third dead time type is called RODBusy and is a general dataflow feedback signal originating from the subdetectors. The RODBusy throttles the Level-1 accept rate when the readout buffers become full.

For the listed reasons, the ATLAS online luminosity infrastructure is running independently of the main data acquisition system and dead time free. It gathers the luminosity data from different subdetectors, applies a calibration and afterwards publishes the luminosity in a uniform format with a time granularity of approximately one second. Additionally, the luminosity is integrated over time intervals of a predefined length and then archived. The corresponding time slices are called Luminosity Block (LB) and typically have a length of sixty seconds. The detector and luminosity conditions during the duration of a LB are assumed to be constant. If the data quality of a subdetector is found to be bad at a given time, the corresponding LBs can be marked for exclusion in subsequent physics analyses. When deciding on the length of a LB two things must be considered: a short integration time increases the amount of luminosity data needed to be stored and a long integration time reduces the time granularity with which the data quality can be assessed. Even in case of very short subdetector failures, at least one complete LB is lost for physics analyses. For more information about the ATLAS online luminosity infrastructure it is referred to [14].

Luminosity detectors

ATLAS employs different subdetectors for luminosity measurements, some were built primarily for this purpose and others measure the luminosity as a by-product. All detectors have different geometrical acceptances and efficiencies. The advantage of having many independent luminosity measurements is, that their internal consistency provides an important check of the long-term stability and linearity of a detector response. The subdetectors used for luminosity measurements and their location are shown in figure 3.6. The two main luminosity detectors BCM and LUCID can measure bunch-by-bunch luminosities, whereas the other detectors measure the overall luminosity summed over all colliding bunch pairs (BCID-blind). After being absolutely calibrated, BCM and LUCID are able to measure the luminosity at any point in time. The other detectors are cross-calibrated to BCM or LUCID and thus provide only independent measurements of the relative luminosity. The absolute calibration of BCM and LUCID is topic of this thesis.

BCM

The BCM comprises one detector station on either side of the ATLAS detector at $|\eta| = 4.2$. The stations are located about 1.84 m away from the interaction region and are made up of four modules, which are arranged in a cross pattern around the beam axis at a radius of about 55 mm. The BCM was designed for monitoring the beam

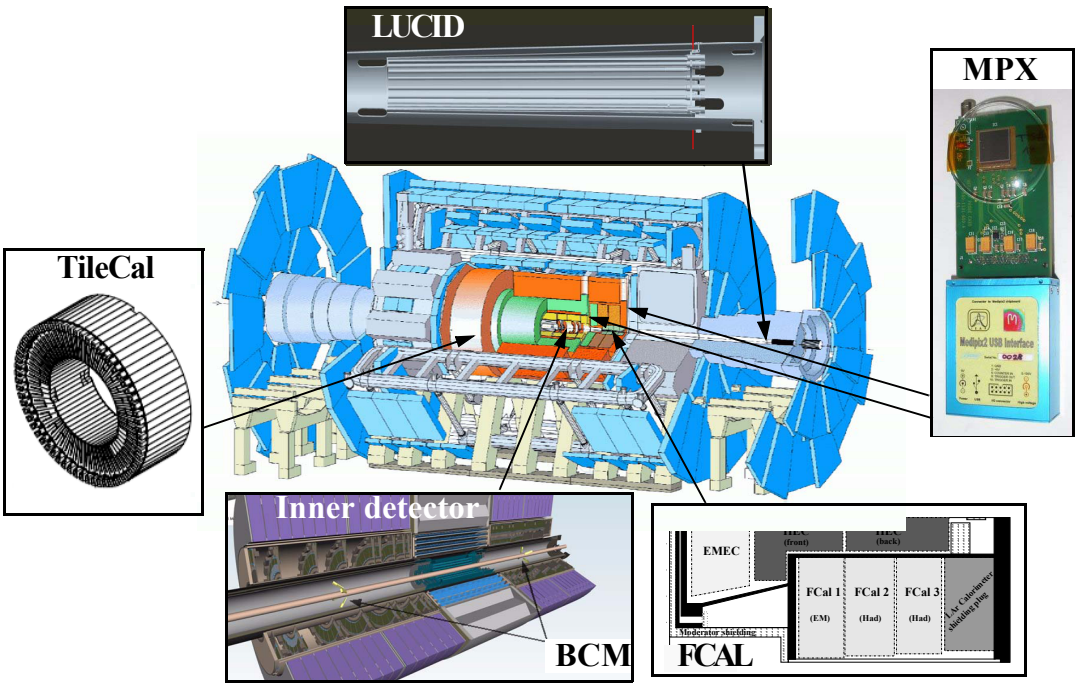

Figure 3.6.: Location of the ATLAS subdetectors used for luminosity measurements [15]. Not shown are the ALFA detectors which are located about 200 m away from the interaction point.

background conditions within the inner detector and to protect the ATLAS detector from damage due to severe beam losses. In order to fulfil this purpose, the BCM is included in the beam abort logic and can trigger a beam dump. Another operational area of the BCM are bunch-by-bunch luminosity measurements. The BCM can distinguish between background particles and particles created in collisions by means of their detection time. Particles emerging from the collision point hit both BCM stations at the same time; background particles hit both stations with a time difference of $(2 \cdot 1.84\,\mathrm{m})/c = 12.23\,\mathrm{ns}$, where c is the speed of light. This value is close to the ideal value of 12.5 ns for 25 ns bunch spacing. The BCM modules are made of CVD[2] diamond sensors which are placed between two electrodes. The sensor material was chosen due to its radiation hardness and its fast signal rise time. A charged particle traversing the sensor ionises the diamond and generates a signal which first is amplified on the module and then transmitted for digitisation to the readout electronics about 15 m away. The two vertical and two horizontal modules on each side are read out independently and the corresponding luminosity measurements are labelled BCMV and BCMH, respectively. Even though both luminosity measurements are treated as independent, they are corre-

[2]Abbreviation of *Chemical Vapour Deposited*

lated to a high degree because of the modules common design. More information about the BCM is available in [16].

LUCID

LUCID is a dedicated luminosity detector which measures inelastic proton-proton interactions in the forward direction, thus providing bunch-by-bunch luminosity and beam background information. It consists of one radiation hard detector station covering the range $5.6 < |\eta| < 6.0$ on either side of the ATLAS detector, 17 m away from the IP. Each station comprises twenty aluminium tubes which point towards the interaction region and are arranged symmetrically around the beam axis at a radius of approximately 10 cm. The tubes have a length of 1.5 m and a diameter of 15 mm. A common aluminium vessel guarantees that all tubes are filled with the gas C_4F_{10} at a constant pressure of 1.2-1.4 bar. A charged particle passing a tube causes the production of Cerenkov photons which are emitted with an angle of 3° with respect to the particles flight direction. On average, the photons are reflected three times by the inner shell of the tubes before they are converted into electrical signals by a photomultiplier tube (PMT) at the back end of the aluminium tube. The PMTs are separated from the gas via quartz windows which produce additional Cerenkov photons. The PMT pulse height allows to count the number of particles traversing a tube and the signals are fast enough to clearly associate them to a bunch crossing. If the signal of a tube exceeds a predefined threshold, the tube generates a "hit". During the year 2012, LUCID was operated without gas and Cerenkov photons were only produced by the quartz window in front of the PMTs. More details are available in [9, 17].

FCal and TileCal

The calorimeters measure the relative luminosity summed over all bunches with a time granularity of a few seconds [17]. The underlying principle for both FCal and TileCal is, that currents drawn in particular calorimeter regions are proportional to the particle flux in that region. The FCal measurements are based on the currents used to provide a stable electric field across the LAr cells in the modules closest to the interaction region. The TileCal measurements are based on the currents drawn by the PMTs in order to convert the scintillator photons into electrical signals. The consistency of different readout channels in FCal and TileCal is used as an internal cross check and helps to identify malfunctioning channels. Only channels satisfying several quality requirements are used for luminosity measurements.

MPX

The MPX system consists of Medipix2 detectors installed at different places within the ATLAS detector [18]. Medipix2 detectors are silicon-based radiation detectors developed at CERN. The primary goal of the MPX system is to measure the radiation field and its composition within ATLAS. It can be used for relative luminosity measurements, since the number of particles detected by the MPX detectors is assumed to be proportional to the luminosity. Like FCal and TileCal, the MPX system measures the luminosity summed over all colliding bunch pairs.

ALFA

The ALFA[3] detector comprises two roman pot stations on either side of ATLAS, located about 240 m away from the IP, and employs scintillating-fibre trackers to measure elastic scattering rates at very low momentum transfer. The roman pot technique was used the first time at the ISR at CERN [19]. It is characterised by detectors mounted on movable holding devices which can be driven very close to the beam. Absolute luminosity measurements via scattering rates in the Coulomb interference regime are only possible in dedicated LHC fills with special beam optics as detailed in section 4.4. Even though ALFA is not able to measure the luminosity under typical LHC running conditions, it can be used to cross-calibrate other detectors.

Others

For consistency checks, ATLAS aims at commissioning as many independent luminosity detectors as possible. Methods currently under study are primary vertex counting, vertexing based event counting and current measurements of the RPCs. The counting of primary vertices is challenging, because it requires a good understanding of the dependence of the vertex reconstruction efficiency on the number of vertices per event.

[3] *Absolute Luminosity For ATLAS*

4. Theory of luminosity

The luminosity is a parameter describing the ability of an accelerator to produce particle interactions and is defined as

$$\mathcal{L} = \frac{dR}{dt} \cdot \frac{1}{\sigma_p} \tag{4.1}$$

where dR/dt is the number of interactions per unit time and σ_p the interaction cross section. The luminosity is given in units of $\mathrm{cm}^{-2}\mathrm{s}^{-1}$, the cross section in units of barn[1]. In general, the discovery and analysis of rare particles requires a large number of events to be statistically significant. In terms of luminosity, this is expressed with the integrated luminosity, defined as

$$\mathcal{L}_{int} = \int \mathcal{L}\, dt \tag{4.2}$$

and measured in units of inverse barn. In the following, a general luminosity expression for the collision of particle bunches is presented. Then the luminosity for the collision of particle bunches with Gaussian density profiles is deduced, followed by a discussion of various effects which reduce the luminosity compared to the case of ideal head-on collisions without crossing angle. Finally, different methods for measuring the luminosity are presented. The first part of this chapter is structured in a similar way to [20].

4.1. Luminosity for particle bunches

Figure 4.1 illustrates the collision of two particle bunches. The corresponding luminosity can be expressed as a function of beam properties:

$$\mathcal{L} = K\, n_1 n_2 f_r n_b \iiiint_{-\infty}^{\infty} \rho_1(x,y,z,t)\rho_2(x,y,z,t)dxdydzdt \tag{4.3}$$

where K is the kinematic factor, n_b the number of colliding bunch pairs, and n_1 and n_2 the number of particles per bunch in beam 1 and beam 2. For a circular collider,

[1] $1\,\mathrm{barn} = 1\,\mathrm{b} = 10^{-28}\,\mathrm{m}^{-2}$

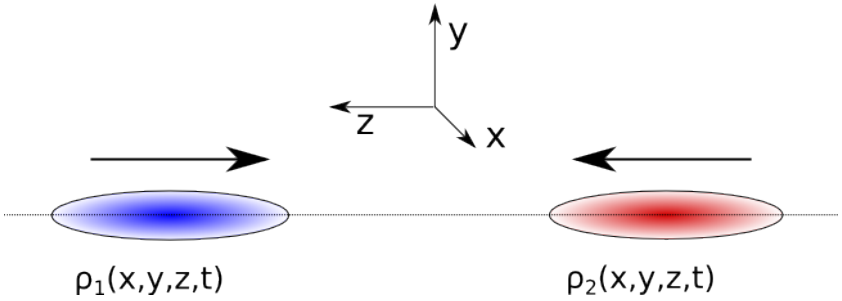

Figure 4.1.: Head-on collision of two particle bunches.

the collision frequency f_r per colliding bunch pair is identical to the revolution frequency. $\rho_1(x, y, z, t)$ and $\rho_2(x, y, z, t)$ are the normalised particle densities of the bunches in beam 1 and beam 2, respectively. The normalisation of the particle densities ensures that, independent of time t, the following condition holds true:

$$\iiint_{-\infty}^{\infty} \rho(x, y, z, t) dx dy dz = 1 \tag{4.4}$$

The kinematic factor K[21] is defined as

$$K = \sqrt{(\vec{v_1} - \vec{v_2})^2 - \frac{(\vec{v_1} \times \vec{v_2})^2}{c^2}} \tag{4.5}$$

where c is the speed of light, and $\vec{v_1}$ and $\vec{v_2}$ denote the velocity of beam 1 and beam 2, respectively. K takes the movement of both beams with respect to each other into account. In the following it is assumed, that the beams are collinear and have speed of light, and K becomes $2c$. If furthermore the particle densities of the bunches factorise into independent x, y and z components, i.e.

$$\rho(x, y, z, t) = \rho_x(x)\rho_y(y)\rho_z(z \pm ct) \tag{4.6}$$

one can write:

$$\mathcal{L} = n_1 n_2 f_r n_b \iint_{-\infty}^{\infty} \rho_{1x}(x)\rho_{1y}(y)\rho_{2x}(x)\rho_{2y}(y) dx dy \tag{4.7}$$

Here the z components of the integral vanished, since the beams are assumed to be collinear.

4.2. Luminosity for bunches with Gaussian profiles

Often it is a good approximation to assume that the bunches have a Gaussian density profile in all dimensions. However, the widths of the Gaussian profiles in the x and y plane and between both colliding bunches can be different and the density functions are given by

$$\rho_{ix}(x) = \frac{1}{\sqrt{2\pi}\sigma_{ix}} \exp\left(-\frac{x^2}{2\sigma_{ix}^2}\right) \tag{4.8}$$

$$\rho_{iy}(y) = \frac{1}{\sqrt{2\pi}\sigma_{iy}} \exp\left(-\frac{y^2}{2\sigma_{iy}^2}\right) \tag{4.9}$$

σ denotes the width of the Gaussians and $i \in 1, 2$ corresponds to beam 1 and beam 2. Using the identity

$$\int_{-\infty}^{\infty} \exp\left(-\left(at^2 + bt + c\right)\right) dt = \sqrt{\pi/a} \exp\left(\frac{b^2 - ac}{a}\right) \tag{4.10}$$

one can solve equation (4.7) and obtains for the luminosity:

$$\mathcal{L} = \frac{n_1 n_2 f_r n_b}{2\pi\sqrt{\sigma_{1x}^2 + \sigma_{2x}^2}\sqrt{\sigma_{1y}^2 + \sigma_{2y}^2}} \tag{4.11}$$

For the simplified case of $\sigma_{1x} = \sigma_{2x}$ and $\sigma_{1y} = \sigma_{2y}$, this expression reduces to

$$\mathcal{L} = \frac{n_1 n_2 f_r n_b}{4\pi\sigma_x\sigma_y} \tag{4.12}$$

With this well-known expression one can easily identify the beam properties needed for high luminosities: a large product of the number of protons in the colliding bunches ($n_1 n_2$), a high collision frequency, a large number of colliding bunches and small transverse beam sizes at the interaction point.

4.3. Luminosity reducing effects

There are various effects which reduce the luminosity for colliding particle bunches with respect to the case of ideal head-on collisions without crossing angle, namely: collisions of imperfectly centred beams, collisions of beams with a crossing angle and collisions considering the hourglass effect. The formulae presented in this section are for particle bunches with Gaussian density profiles in the simplified case of $\sigma_{1x} = \sigma_{2x}$ and $\sigma_{1y} = \sigma_{2y}$.

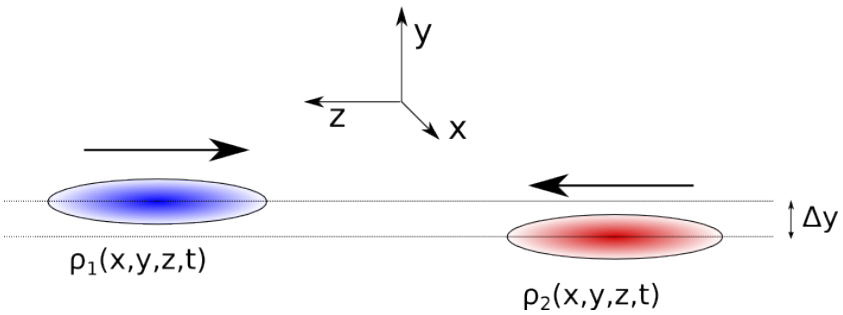

Figure 4.2.: Collision of two particle bunches with a transverse offset.

Collisions of imperfectly centred beams

In reality, beams never collide perfectly head-on. Instead there is always a small transverse offset as depicted in figure 4.2. Without loss of generality, it is assumed that the beams are offset by Δy in the y-plane and centred in the x-plane. While the horizontal densities of the particle bunches remain unchanged, the vertical densities are slightly altered with respect to equation (4.9):

$$\rho_{1y/2y}(y) = \frac{1}{\sqrt{2\pi}\sigma_y} \exp\left(-\frac{(y \pm \Delta y/2)^2}{2\sigma_y^2}\right) \tag{4.13}$$

where beam 1 is offset by $+\Delta y/2$ and beam 2 by $-\Delta y/2$. Then, the vertical bunch density product is given by

$$\rho_{1y}(y) \cdot \rho_{2y}(y) = \left[\frac{1}{\sqrt{2\pi}\sigma_y} \exp\left(-\frac{y^2}{2\sigma_y^2}\right)\right]^2 \cdot W \tag{4.14}$$

where W is defined as

$$W = \exp\left(-\frac{\Delta y^2}{4\sigma_y^2}\right) \tag{4.15}$$

The factor W only depends on Δy and σ_y. It is therefore treated as a constant in the luminosity equation (4.7), and its evaluation yields

$$\mathcal{L} = \frac{n_1 n_2 f_r n_b}{4\pi\sigma_x\sigma_y} \cdot W \tag{4.16}$$

This expression is identical to the head-on case in equation (4.12) with the exception of the factor W.

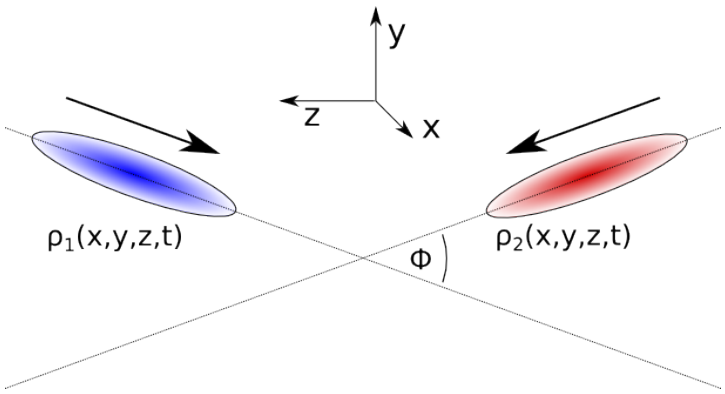

Figure 4.3.: Collision of two particle bunches with a crossing angle.

Collisions of beams with a crossing angle

If the colliding beams have a crossing angle Φ with respect to each other as illustrated in figure 4.3, the longitudinal bunch length σ_z must not be ignored anymore. For small Φ and $\sigma_z \gg \sigma_x, \sigma_y$ the luminosity can be approximated by

$$\mathcal{L} = \frac{n_1 n_2 f_r n_b}{4\pi\sigma_x\sigma_y} \cdot S \tag{4.17}$$

with S being

$$S \approx \left[1 + \left(\frac{\sigma_z}{\sigma_y}\frac{\Phi}{2}\right)^2\right]^{-\frac{1}{2}} \tag{4.18}$$

A detailed derivation of this result is available in [20]. Nominally the LHC is operated with a crossing angle of $\Phi = 285\,\mu$rad at Point 1. Assuming a typical transverse beam size of $\sigma_x = \sigma_y = 17\,\mu$m and a bunch length of $\sigma_z = 8\,$cm, the luminosity reduction factor S evaluates to 0.83. Even though the crossing angle implies a sizeable loss of luminosity, it is required by the LHC experiments. Without crossing angle and in case of a short bunch spacing, there would be unwanted collisions of particle bunches at displaced locations within the detectors. The factor S is also known as the geometric factor.

Collisions of transversely offset beams with a crossing angle

If the beams are transversely offset in the crossing plane and collide with a vertical crossing angle as illustrated in figure 4.4, the luminosity is given by

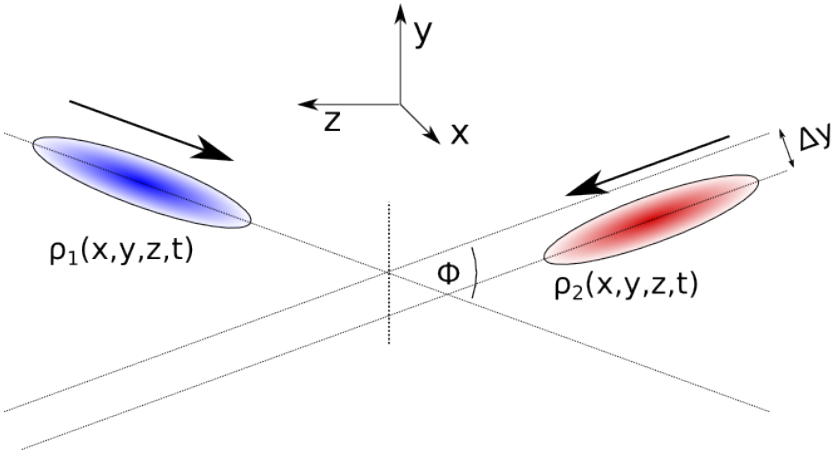

Figure 4.4.: Collision of two bunches with a transverse offset and crossing angle

$$\mathcal{L} = \frac{n_1 n_2 f_r n_b}{4\pi\sigma_x\sigma_y} \cdot W \cdot S \cdot e^{\frac{B^2}{A}}\,, \tag{4.19}$$

$$\text{where} \quad A = \frac{\sin^2\frac{\Phi}{2}}{\sigma_y^2} + \frac{\cos^2\frac{\Phi}{2}}{\sigma_z^2} \quad \text{and} \quad B = \frac{\Delta y \sin\frac{\Phi}{2}}{2\sigma_y^2}\,. \tag{4.20}$$

W and S are the reduction factors which were derived for the case of offset beams and for the case of a non-zero crossing angle, respectively. A derivation is available in [20]. The factor $e^{\frac{B^2}{A}}$ only deviates from unity, if the beams collide with a transverse offset and a non-zero crossing angle. This can be easily seen, since B evaluates to zero for either $\Phi = 0$ or $\Delta y = 0$. It should be noted, that for collisions with a crossing angle, a timing mismatch of the bunches is equivalent to imperfectly centred beams in the crossing plane.

Hourglass effect

So far it was assumed, that the particle densities of the bunches factorise into independent transverse and longitudinal components; in general, this is only an approximation. Of special relevance in this context is the hourglass effect, which arises from the transverse focussing of the beams at the IP.

In order to keep the beams inside the beam pipe they must be steadily focussed. This is done with a lattice of alternating focussing and defocussing magnet elements, resulting in a net-focussing effect. The transverse focussing along the path of the particle beam is described by the β-function. More precisely, it is the envelope of all possible particle trajectories in the accelerator and defined via the relation

$$\sigma\left(z\right) = \sqrt{\epsilon\,\beta(z)} \tag{4.21}$$

where ϵ is the transverse bunch emittance and $\sigma(z)$ the transverse bunch size along the beam trajectory at position z. The bunch emittance is a measure of the spread in the position-momentum phase space of the particles and an intrinsic bunch property. From equation (4.21) follows that in order to achieve small transverse bunch sizes, one needs small emittances as well as strong focussing. Typically, the bunch emittance in a proton accelerator like the LHC only slowly increases during a fill.

The β-function has its minimum at the IP ($\beta(0) = \beta^*$) and can be approximated at a distance z from the IP by the expression:

$$\beta\left(z\right) = \beta^* \cdot \left[1 + \left(\frac{z}{\beta^*}\right)^2\right] \tag{4.22}$$

The combination of equation (4.21) and (4.22) yields the relative increase of the transverse bunch size at position z with respect to the one at $z = 0$:

$$\frac{\sigma(z)}{\sigma^*} = \sqrt{1 + \left(\frac{z}{\beta^*}\right)^2} \tag{4.23}$$

where $\sigma^* = \sigma(0)$ is the transverse bunch size at the IP. The increase and its dependency on z is illustrated in figure 4.5 for two different values of β^*. $\beta^* = 0.6\,\mathrm{m}$ was the default at the LHC in 2012 for proton-proton collisions, while $\beta^* = 11\,\mathrm{m}$ corresponds to the LHC injection beam optics. Whereas the hourglass effect, named after the hourglass like shape of the β-function near the interaction region, is negligible for $\beta^* = 11\,\mathrm{m}$, it is more pronounced for $\beta^* = 0.6\,\mathrm{m}$.

The analytical expression for the luminosity reduction due to the hourglass effect is not discussed here, but can be found in [20]. As a rule of thumb, the reduction in luminosity due to the hourglass effect increases with the bunch length σ_z, and becomes significant when σ_z is close to β^*. For nominal design LHC parameters ($\beta^* = 0.55\,\mathrm{m}$, $\Phi = 285\,\mu\mathrm{rad}$, $\sigma_z = 7.7\,\mathrm{cm}$, $\sigma^* = 16.7\,\mu\mathrm{m}$), the decrease is less than 1% [20] and hence much smaller than the reduction originating from the crossing angle. The parameters used during typical LHC operation in 2012 are slightly different from the nominal design values, but result in a very similar luminosity reduction.

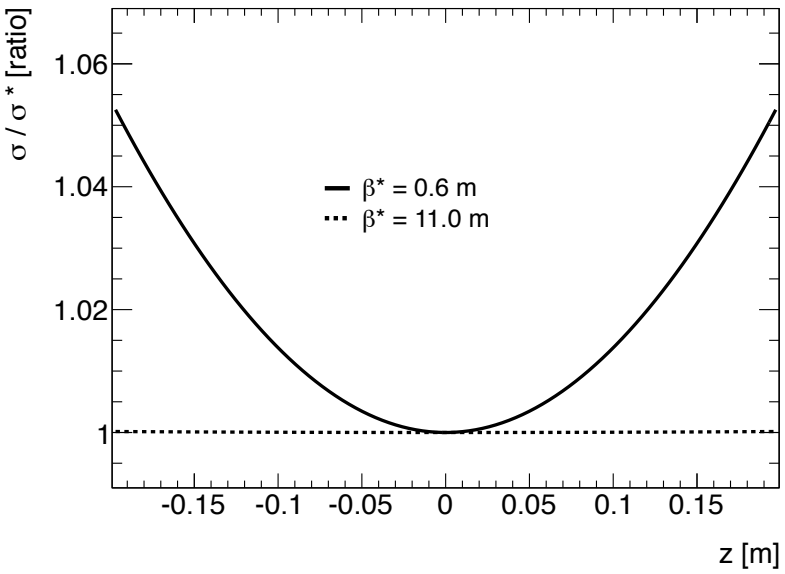

Figure 4.5.: Relative increase of the transverse bunch size near the IP for two different values of β^*.

4.4. Measuring absolute luminosity

There are different possibilities to measure the absolute luminosity; which method is suited best and results in the highest precision depends on many factors. For that reason, the primary method for determining the absolute luminosity can vary among different particle physics accelerators. In this section an overview of the different methods and their advantages and limitations is given, all with special focus on the LHC.

Luminosity from theoretically well-known cross sections

One way to measure the absolute luminosity relies on the fact that the luminosity is the proportionality factor between the rate of a process dR/dt and its cross section σ, see equation (4.1). If σ is well known from theory, the measurement of the luminosity becomes equivalent to the measurement of dR/dt. The requirements on a suited process are: σ can be theoretically precisely calculated, clear signature which the detector can identify with a known efficiency, dR/dt is large enough to neglect statistical uncertainties.

The most promising processes for luminosity measurements at the LHC are the production of lepton pairs in elastic proton-proton scattering processes and the production of $W^{\pm}$ or Z bosons [22].

The production of lepton pairs in elastic proton-proton scattering processes can be precisely calculated via quantum electrodynamics and its usage for luminosity measure-

ments was first proposed in [23]; even though the theoretical cross sections have an accuracy of better than 1 % [24], it is challenging to distinguish the process signatures from other processes involving lepton pairs.

The theoretical $W^{\pm}$ or Z boson production cross sections have a precision of 2-3 % and are limited by the knowledge on the parton distribution functions [25]. If the PDFs can be confined with LHC measurements, the achievable luminosity precision was estimated by the ATLAS experiment to be 1-3 % [25].

Luminosity from Optical Theorem and Coulomb scattering

The optical theorem relates the total cross section σ_{tot} to the elastic scattering amplitude f_{el} in forward direction:

$$\sigma_{tot} = 4\pi \cdot \mathrm{Im}\left[f_{el}(t=0)\right] \tag{4.24}$$

where t is the squared 4-momentum transfer and $f_{el}(t=0)$ the scattering amplitude for zero momentum transfer. Based on the optical theorem, the luminosity can be written as

$$\mathcal{L} = \frac{1}{16\pi} \frac{R_{tot}^2(1+\rho^2)}{\frac{dR_{el}}{dt}\big|_{t=0}} \tag{4.25}$$

where R_{tot} is the total interaction rate and R_{el} the rate of elastic interactions. The value of $dR_{el}/dt|_{t=0}$ can be obtained via extrapolating the derivative of R_{el} with respect to t to zero momentum transfer. ρ is given by

$$\rho = \left.\frac{\mathrm{Re}\, f_{el}(t)}{\mathrm{Im}\, f_{el}(t)}\right|_{t=0} \tag{4.26}$$

and theoretically known to a precision which translates into a luminosity uncertainty of less than 0.5 % [26]. For small scattering angles θ and known beam momentum p, one can determine t by measuring θ:

$$t = -\left(p\theta\right)^2 \tag{4.27}$$

The challenge of using the optical theorem for luminosity measurements is threefold: Firstly, the determination of R_{tot} requires a detector with good pseudorapidity coverage. Secondly, the measurement of elastic interactions with small momentum transfer requires detectors close to the beam. Thirdly, special beam optics are required in order to make the particle trajectories at the IP as parallel as possible, since a large beam diver-

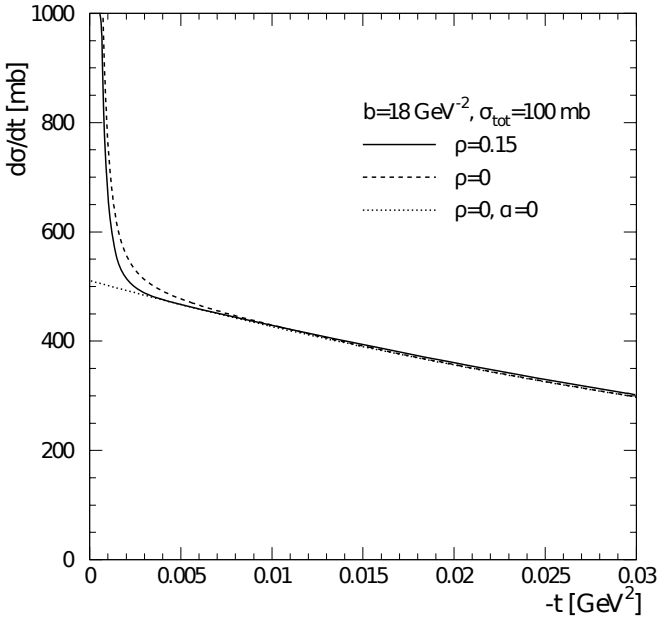

Figure 4.6.: Differential cross section $d\sigma/dt$ as a function of t for different parameter sets and for a beam energy of 7 TeV [26].

gence would make the determination of small scattering angles impossible. At the LHC, the luminosity determination based on the optical theorem is pursued by the TOTEM experiment [27]. The accomplished precision in 2012 was 4 % [28].

The absolute luminosity can also be determined by measuring elastic scattering rates in the Coulomb interference regime at even smaller values of t. Simplified, the scattering rates in this region of t can be parameterised as

$$\frac{dN}{dt} = \mathcal{L}\pi|f_C + f_N|^2 \approx \mathcal{L}\pi \left| -\frac{2\alpha}{|t|} + \frac{\sigma_{tot}}{4\pi}(i+\rho)e^{-b|t|/2} \right|^2 \tag{4.28}$$

where f_C is the Coulomb scattering amplitude and f_N the nuclear one. For illustration purposes, the dependence of the differential cross section $d\sigma/dt$ on t is shown in figure 4.6 for different parameter sets. For $\rho = \alpha = 0$ the differential cross section is purely given by nuclear scattering; for other parameter sets ($\alpha > 0$) one can identify the Coulomb interference region. At very low values of t the scattering process is dominated by the electromagnetic force, which the colliding particles exert on each other. A fit of equation (4.28) to the measured data determines $\mathcal{L}$, σ_{tot}, ρ and b and does not depend on further input since the Coulomb cross section is well known. At the LHC, this method is used by the ALFA detector [26, 29] which is part of the ATLAS experiment. The beam

optics needed for accessing the Coulomb interference regime are very demanding and require dedicated fills and studies. Hence they have not been fully commissioned, yet. The achievable precision on the absolute luminosity is expected to be approximately 3 % [26].

Luminosity from beam parameters

The luminosity for collisions of particle bunches derived in equation (4.12)

$$\mathcal{L} = \frac{n_1 n_2 f_r n_b}{2\pi\sqrt{\sigma_{1x}^2 + \sigma_{2x}^2}\sqrt{\sigma_{1y}^2 + \sigma_{2y}^2}} \tag{4.29}$$

can be used to measure the absolute luminosity based on beam parameters. The revolution frequency f_r can be precisely measured and the number of colliding bunches n_b is known. The product of the number of protons in the colliding bunches $n_1 n_2$ can be measured with dedicated beam instrumentation and different ways exist to determine the transverse bunch sizes at the interaction point:

- The transverse bunch profiles can be determined at suitable locations around the ring with invasive (e.g. with scintillating screens or wire scanners) or non-invasive methods (e.g. via synchrotron light). If the β-function around the ring is known, the bunch sizes can be transferred from the measurement location to the IP. The disadvantage of this method is, that it relies on an accurate beam optics model which to obtain usually is challenging.

- From equation (4.29) follows that the knowledge of the individual bunch sizes is not necessary for the purpose of luminosity determination. Instead a measurement of the convolved bunch sizes, given by $\sqrt{\sigma_{1x}^2 + \sigma_{2x}^2}$ and $\sqrt{\sigma_{1y}^2 + \sigma_{2y}^2}$, is sufficient. The convolved bunch sizes can be determined in VdM scans, which is described in detail in chapter 5. The luminosity determination carried out in this thesis is based on VdM scans.

- A more recent method was proposed in [30] and makes use of the interactions of beam particles with residual gas in the beam pipe. By analysing the tracks originating from beam-gas interactions, one can reconstruct the location of each interaction vertex. This method is also called beam-gas imaging. Assuming a homogeneous density of the residual gas, the transversely projected density of the beam-gas vertices is identical to the transverse beam profile. In order to distinguish

beam-gas from beam-beam interactions, dedicated triggers must be employed. Luminosity measurements based on beam-gas imaging were first performed by the LHCb experiment [31], which is well suited to this method due to its high vertexing capability. The advantage compared to other beam profile measurements is that the measurements are done directly at the IP and therefore no knowledge of the β-function is required. However, the method is subject to various uncertainties, and not competitive to VdM scans.

5. Absolute luminosity calibration with Van der Meer scans

The measurement of the absolute luminosity in dedicated beam separation scans was first proposed by Simon van der Meer in the year 1968 [32], hence this type of scan is commonly referred to as Van der Meer scan, or abbreviated: VdM scan. The key idea of a VdM scan is to determine the overlap integral of the transverse profile densities of the colliding beams through the dependency of the luminosity on the transverse separation of the beams. The dependency can be experimentally assessed with a detector which generates counts proportional to the interaction rate. Even though Simon van der Meer originally proposed this method for the ISR at CERN, which had beams without a longitudinal substructure, the procedure is also applicable to beams made up of particle bunches as shown by Carlo Rubbia in [33].

In the past, VdM scans were successfully carried out at HERA [34], at RHIC [35], at the Tevatron [36] and recently also at the LHC [37, 38]. At the time of writing, VdM scans are the primary method for luminosity determination in the four main LHC experiments. In this chapter, the main VdM scan formulae are deduced, starting from the luminosity formula for colliding particle bunches derived in chapter 4. It is important to note, that the density profiles of the bunches are assumed to be uncorrelated in the x and y plane. Afterwards three convolved beam profile models are introduced, all of which are of importance for the VdM scan evaluation carried out in this thesis. In conclusion, a few remarks are made on the generalisation of the VdM scan procedure.

5.1. Theory of Van der Meer scans

Based on equation (4.1) the luminosity can be written as

$$\mathcal{L} = \frac{R_{inel}}{\sigma_{inel}} = \frac{\mu \, n_b \, f_r}{\sigma_{inel}} \tag{5.1}$$

where μ is the mean number of inelastic interactions per bunch crossing, the other quantities are defined as in chapter 4. At LHC energies, the inelastic proton-proton

cross section σ_{inel} is not precisely known, neither from theoretical predictions nor from independent measurements. Since it is furthermore challenging to measure μ, equation (5.1) is not well suited for luminosity measurements. Instead one must consider a luminosity detector which measures the quantity μ_{vis}, defined as μ multiplied by the detector efficiency ϵ:

$$\mathcal{L} = \frac{\mu_{vis}\, n_b\, f_r}{\sigma_{vis}} \tag{5.2}$$

where σ_{vis} is the visible cross section and given by $\sigma_{vis} = \epsilon \cdot \sigma_{inel}$. The detector efficiency ϵ is the overall efficiency, accounting for the geometrical acceptance as well as the detection efficiency. A VdM scan allows to calibrate the luminosity detector, or equivalently, to determine σ_{vis}. Once calibrated, the detector can monitor the luminosity at any times.

The luminosity for head-on collisions of particle bunches without crossing angle in case of uncorrelated particle densities in the x and y plane is given in equation (4.7):

$$\mathcal{L} = n_1 n_2 f_r n_b \iint_{-\infty}^{\infty} \rho_{1x}(x)\rho_{1y}(y)\rho_{2x}(x)\rho_{2y}(y)dxdy. \tag{5.3}$$

After rearranging the terms and integrals one can write

$$\mathcal{L} = n_1 n_2 f_r n_b \int_{-\infty}^{\infty} \rho_{1x}(x)\rho_{2x}(x)dx \int_{-\infty}^{\infty} \rho_{1y}(y)\rho_{2y}(y)dy \tag{5.4}$$

Even though this formula is valid for head-on collisions only, one can easily adapt it to transversely offset beams:

$$\mathcal{L}(\Delta x_0, \Delta y_0) = n_1 n_2 f_r n_b \int_{-\infty}^{\infty} \rho_{1x}(x)\rho_{2x}(x + \Delta x_0)dx \int_{-\infty}^{\infty} \rho_{1y}(y)\rho_{2y}(y + \Delta y_0)dy \tag{5.5}$$

where Δx_0 and Δy_0 are the transverse beam offsets in the x and y plane, respectively. Since the vertical bunch overlap integral is independent of Δx, it follows, that for a given vertical separation Δy_0 the luminosity is proportional to the horizontal bunch overlap integral:

$$\mathcal{L}(\Delta x, \Delta y_0) = C_y \int_{-\infty}^{\infty} \rho_{1x}(x)\rho_{2x}(x + \Delta x)dx \tag{5.6}$$

where C_y is a constant. With a luminosity detector one can measure the rate of beam-beam interactions:

$$\mathcal{R}(\Delta x, \Delta y_0) = \sigma_{vis}\, \mathcal{L}(\Delta x, \Delta y_0) = \sigma_{vis}\, C_y \int_{-\infty}^{\infty} \rho_{1x}(x)\rho_{2x}(x + \Delta x)dx \tag{5.7}$$

The idea of Simon van der Meer was to determine $\sigma_{vis}C_y$ from the dependency of $\mathcal{R}$ on the transverse beam separation. The integration of both sides of equation 5.7 over the horizontal separation Δx yields:

$$\int_{-\infty}^{\infty} \mathcal{R}(\Delta x, \Delta y_0)d(\Delta x) = \sigma_{vis}C_y \iint_{-\infty}^{\infty} \rho_{1x}(x)\rho_{2x}(x + \Delta x)dx\, d(\Delta x) \tag{5.8}$$

After changing the integration order

$$\int_{-\infty}^{\infty} \mathcal{R}(\Delta x, \Delta y_0)d(\Delta x) = \sigma_{vis}C_y \iint_{-\infty}^{\infty} \rho_{1x}(x)\rho_{2x}(x + \Delta x)d(\Delta x)\, dx \tag{5.9}$$

one can make use of the following identity:

$$\int_{-\infty}^{\infty} \rho_{2x}(x + \Delta x)d(\Delta x) = \int_{-\infty}^{\infty} \rho_{2x}(x)dx \tag{5.10}$$

Then equation 5.9 can be written as

$$\int_{-\infty}^{\infty} \mathcal{R}(\Delta x, \Delta y_0)d(\Delta x) = \sigma_{vis}C_y \int_{-\infty}^{\infty} \rho_{1x}(x)dx \cdot \int_{-\infty}^{\infty} \rho_{2x}(x)dx \tag{5.11}$$

Since the beam densities are normalised, i.e. $\int \rho_{1x}(x)dx = 1$ and $\int \rho_{2x}(x)dx = 1$, one can finally express $\sigma_{vis}C_y$ in terms of rates only:

$$\sigma_{vis}C_y = \int_{-\infty}^{\infty} \mathcal{R}(\Delta x, \Delta y_0)d(\Delta x) \tag{5.12}$$

Combining this result with equation 5.7 yields the relation:

$$\mathcal{R}(\Delta x_0, \Delta y_0) = \int_{-\infty}^{\infty} \mathcal{R}(\Delta x, \Delta y_0)d(\Delta x) \cdot \int_{-\infty}^{\infty} \rho_{1x}(x)\rho_{2x}(x + \Delta x_0)dx \tag{5.13}$$

After dividing by the rate integral, the equation reads:

$$\frac{\mathcal{R}(\Delta x_0, \Delta y_0)}{\int_{-\infty}^{\infty} \mathcal{R}(\Delta x, \Delta y_0)d(\Delta x)} = \int_{-\infty}^{\infty} \rho_{1x}(x)\rho_{2x}(x + \Delta x_0)dx \tag{5.14}$$

This identity relates the horizontal bunch overlap integral to an experimentally easily accessible observable. The analogous expression for the vertical bunch overlap integral is:

$$\frac{\mathcal{R}(\Delta x_0, \Delta y_0)}{\int_{-\infty}^{\infty} \mathcal{R}(\Delta x_0, \Delta y) d(\Delta y)} = \int_{-\infty}^{\infty} \rho_{1y}(y) \rho_{2y}(y + \Delta y_0) dy \tag{5.15}$$

Substituting the horizontal and vertical bunch overlap integrals in equation 5.5, one obtains:

$$\mathcal{L}(\Delta x_0, \Delta y_0) = n_1 n_2 f_r n_b \frac{\mathcal{R}(\Delta x_0, \Delta y_0)}{\int_{-\infty}^{\infty} \mathcal{R}(\Delta x, \Delta y_0) d(\Delta x)} \frac{\mathcal{R}(\Delta x_0, \Delta y_0)}{\int_{-\infty}^{\infty} \mathcal{R}(\Delta y, \Delta x_0) d(\Delta y)} \tag{5.16}$$

This formula is a fundamental result for extracting the luminosity for a given transverse beam separation $(\Delta x_0, \Delta y_0)$ from beam parameters:

- $n_1 n_2$ is the product of the number of protons in the colliding bunches. It can be measured with dedicated beam instrumentation. From now on, this product is referred to as bunch current product, even though in the strict sense the number of protons is not equivalent to a current.
- the collision frequency f_r and number of colliding bunch pairs n_b are known,
- the fraction $\mathcal{R}(\Delta x_0, \Delta y_0) / \int_{-\infty}^{\infty} \mathcal{R}(\Delta x, \Delta y_0) d(\Delta x)$ can be determined via stepwise separating the beams in the horizontal plane and measuring the rate as a function of Δx, known as x scan,
- the fraction $\mathcal{R}(\Delta x_0, \Delta y_0) / \int_{-\infty}^{\infty} \mathcal{R}(\Delta y, \Delta x_0) d(\Delta y)$ can be determined via stepwise separating the beams in the vertical plane and measuring the rate as a function of Δy, known as y scan.

In the following, equation (5.16) is transformed to a slightly different form. After defining the convolved bunch sizes Σ_x and Σ_y as

$$\Sigma_x = \frac{1}{\sqrt{2\pi}} \cdot \frac{\int_{-\infty}^{\infty} \mathcal{R}(\Delta x, \Delta y_0) d(\Delta x)}{\mathcal{R}(0, \Delta y_0)} \tag{5.17}$$

$$\Sigma_y = \frac{1}{\sqrt{2\pi}} \cdot \frac{\int_{-\infty}^{\infty} \mathcal{R}(\Delta x_0, \Delta y) d(\Delta y)}{\mathcal{R}(\Delta x_0, 0)} \tag{5.18}$$

one can write equation (5.16) as

$$\mathcal{L}(\Delta x_0, \Delta y_0) = \frac{n_1 n_2 f_r n_b}{2\pi \Sigma_x \Sigma_y} \frac{\left[\mathcal{R}(\Delta x_0, \Delta y_0)\right]^2}{\mathcal{R}(0, \Delta y_0) \mathcal{R}(\Delta x_0, 0)} \tag{5.19}$$

Accordingly, σ_{vis} is given by

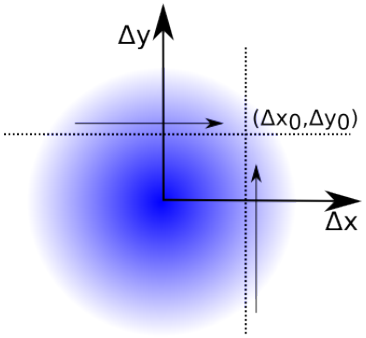

Figure 5.1.: Illustration of a possible VdM scan setup. The dotted lines represent the horizontal and vertical separations scans. The crossing point $(\Delta x_0, \Delta y_0)$ of the dotted lines is called the working point.

$$\sigma_{vis} = \frac{\mathcal{R}(\Delta x_0, \Delta y_0)}{\mathcal{L}(\Delta x_0, \Delta y_0)} = \frac{2\pi\Sigma_x\Sigma_y}{n_1 n_2 f_r n_b} \frac{\mathcal{R}(0, \Delta y_0)\mathcal{R}(\Delta x_0, 0)}{\mathcal{R}(\Delta x_0, \Delta y_0)} \tag{5.20}$$

For bell shaped density profiles, $\mathcal{R}(0, \Delta y_0)$ and $\mathcal{R}(\Delta x_0, 0)$ are the peak rates during the x scan and y scan, respectively. It is important to note, that the VdM procedure is independent of the working point $(\Delta x_0, \Delta y_0)$ and valid for any bunch densities as long as those factorise into independent x and y components. A possible scan setup is illustrated in figure 5.1.

In practice, it is desirable to choose the working point close to $(0, 0)$ for two reasons: high rates keep the statistical uncertainties small, and the uncertainty on the knowledge of the working point translates to a smaller uncertainty on $\mathcal{L}$, and hence σ_{vis}, for head-on collisions than for offset collisions. For the latter argument, one again makes the reasonable assumption that the transverse density profiles of the bunches are well described by a bell shape. The formulae for $\mathcal{L}$ and σ_{vis} are well-known for the case of head-on collisions, i.e. Δx_0=0 and Δy_0=0. Equation (5.19) and (5.20) then reduce to:

$$\mathcal{L}(0, 0) = \frac{n_1 n_2 f_r n_b}{2\pi\Sigma_x\Sigma_y} \quad \text{and} \quad \sigma_{vis} = \frac{2\pi\Sigma_x\Sigma_y}{n_1 n_2 f_r n_b}\mathcal{R}(0, 0) \tag{5.21}$$

The quantities Σ_x and Σ_y are interesting observables as they purely depend on the shape of the scan curves and are independent of the detector efficiency ϵ. Given the beam densities factorise into independent x and y components, which was assumed so far, Σ_x and Σ_y are independent of the separation in the non-scan plane. This can be seen when making use of the relation $\mathcal{R}(\Delta x, \Delta y) = \mathcal{R}_x(\Delta x)\mathcal{R}_y(\Delta y)$:

$$\Sigma_x = \frac{1}{\sqrt{2\pi}} \cdot \frac{\int_{-\infty}^{\infty} \mathcal{R}(\Delta x, \Delta y_0) d(\Delta x)}{\mathcal{R}(0, \Delta y_0)} = \frac{1}{\sqrt{2\pi}} \cdot \frac{\int_{-\infty}^{\infty} \mathcal{R}_x(\Delta x) d(\Delta x)}{\mathcal{R}_x(0)} \tag{5.22}$$

The consistency of Σ_x and Σ_y measured by different luminosity detectors is important for the understanding and quantification of the systematic uncertainties originating from the detector response. In the subsequent paragraphs, the functions $\mathcal{R}(\Delta x, \Delta y_0)$ and $\mathcal{R}(\Delta x_0, \Delta y)$ are referred to as the horizontal and vertical scan curves, respectively.

5.2. Scan curve models

The measurement of the horizontal and vertical scan curves in VdM scans is based on a limited number of scan points. In principle, increasing the number of scan points improves the precision of the scan curve integral determination. In reality, different factors have to be considered when deciding on the number of scan points:

- More scan points increase the overall duration of the scan at the expense of integrated luminosity available for physics analyses. Furthermore, it may be advantageous to repeat a VdM scan a few times in a given fill, in order to verify the reproducibility of the calibration results. The latter only is possible, if the overall duration of a VdM scan is kept short compared to the duration of a fill.
- The VdM scan procedure assumes, that the beam densities are constant over the duration of the scan. This assumption holds the better, the shorter the scan duration is. At the LHC, particular attention needs to be paid to emittance growth over time.
- If the overall uncertainties of a VdM scan are dominated by uncertainties not related to the precision of the scan curve integral, increasing the number of scan points is not meaningful.

In order to determine the scan curve integrals, the scan points are fitted with suitable functions. It does not matter what the functions are, as long as they fit well. The following section introduces three different scan curve models used in the context of this thesis. The corresponding functions and formulae are written down for the horizontal scan curves only; the ones for the vertical scan curves are analogous.

Gaussian scan curves

The most elementary scan curve shape corresponds to a Gaussian distribution. Gaussian scan curves originate from bunches which have a Gaussian density profile, since the convolution of two Gaussian profiles again is a Gaussian profile. The rate as a function of beam separation is

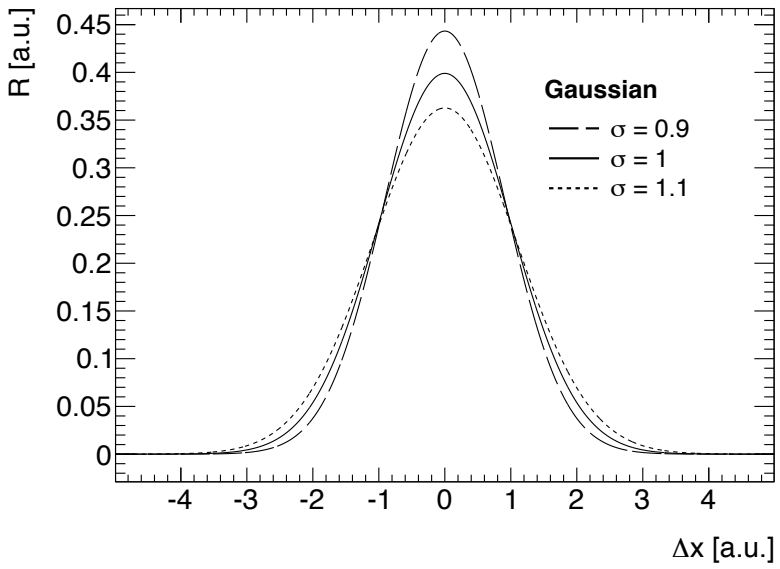

Figure 5.2.: Examples of Gaussian scan curves ($A = 1$, σ varying).

$$\mathcal{R}(\Delta x) = \frac{A}{\sqrt{2\pi}\sigma}\exp\left(-\frac{\Delta x^2}{2\sigma^2}\right) \tag{5.23}$$

where σ is the width of the Gaussian and A an arbitrary scale factor. When evaluating Σ_x, one finds that it is identical to the Gaussian width of the scan curve:

$$\Sigma_x = \frac{1}{\sqrt{2\pi}} \cdot \frac{\int_{-\infty}^{\infty} \mathcal{R}(\Delta x) d(\Delta x)}{\mathcal{R}(0)} = \sigma \tag{5.24}$$

Figure 5.2 illustrates Gaussian scan curves for different parameters.

Double Gaussian scan curves

Another model describes scan curves by a sum of two Gaussians having a common mean but different widths [39]:

$$\mathcal{R}(\Delta x) = A \cdot \left[f_a \cdot \frac{1}{\sqrt{2\pi}\sigma_a}\exp\left(-\frac{\Delta x^2}{2\sigma_a^2}\right) + (1 - f_a) \cdot \frac{1}{\sqrt{2\pi}\sigma_b}\exp\left(-\frac{\Delta x^2}{2\sigma_b^2}\right)\right] \tag{5.25}$$

where $f_a \in [0, 1]$ describes the fractional contribution of the first Gaussian, having width σ_a, to the total scan curve integral and, accordingly, $(1 - f_a)$ the contribution of the second Gaussian, having width σ_b. If the individual transverse bunch profiles are not well modelled by a common Gaussian, they are often adequately described by a Double

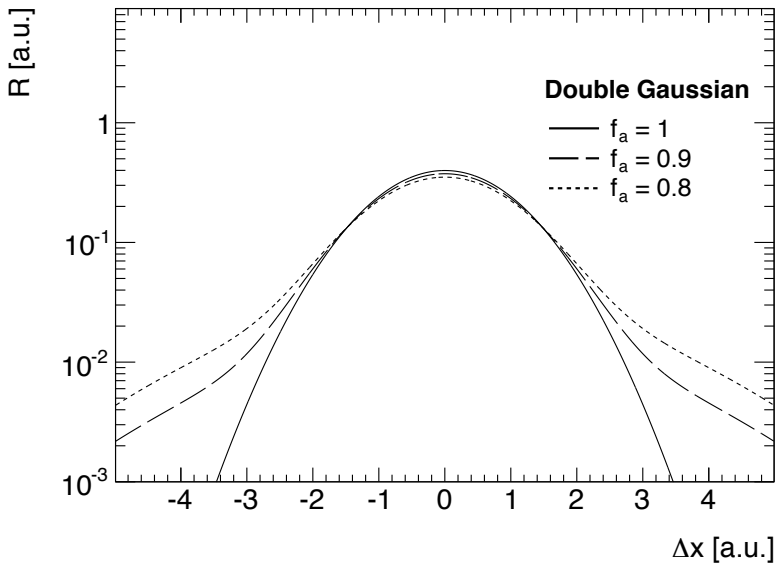

Figure 5.3.: Examples of Double Gaussian scan curves ($A = 1$, $\sigma_a = 1$, $\sigma_b = 2.5$, f_a varying).

Gaussian: the core is modelled by a narrow Gaussian and the tails by a wider Gaussian. Although in the strict sense, the convolution of two Double Gaussians results in a sum of four Gaussians, the scan curves are often also well described by Double Gaussians. Given that

$$\int_{-\infty}^{\infty} \mathcal{R}(\Delta x) d(\Delta x) = A \quad \text{and} \quad \mathcal{R}(0) = \frac{A}{\sqrt{2\pi}} \left(\frac{f_a}{\sigma_a} + \frac{1 - f_a}{\sigma_b} \right) \tag{5.26}$$

the evaluation of Σ_x is straightforward:

$$\Sigma_x = \frac{1}{\sqrt{2\pi}} \cdot \frac{\int_{-\infty}^{\infty} \mathcal{R}(\Delta x) d(\Delta x)}{\mathcal{R}(0)} = \left(\frac{f_a}{\sigma_a} + \frac{1 - f_a}{\sigma_b} \right)^{-1} \tag{5.27}$$

Figure 5.3 depicts Double Gaussian scan curves for different parameter sets. One can see how the wider Gaussian components change the shape of the tails compared to the common Gaussian case (f_a=1).

Super Gaussian scan curves

The third scan curve model is the Super Gaussian model. Its usage in accelerator physics is motivated in [40] and it only was recently proposed to employ it for describing scan curves [41]. The corresponding fit function is an extension of a common Gaussian:

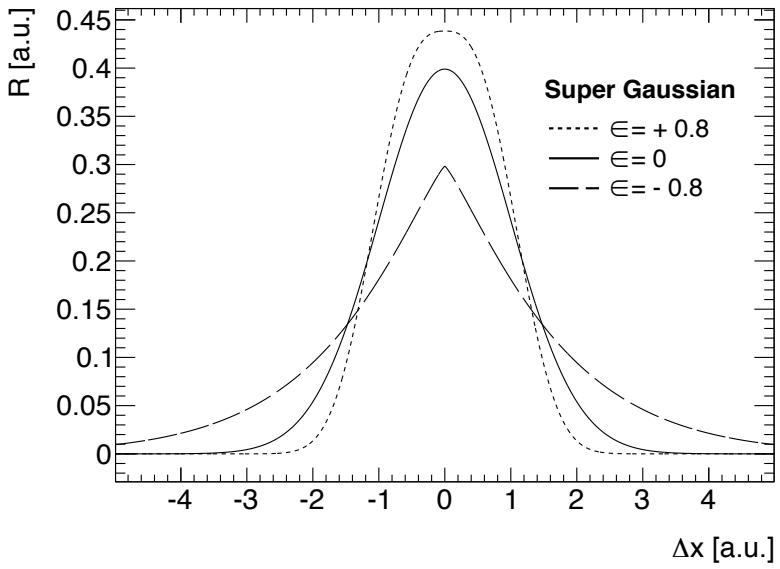

Figure 5.4.: Examples of Super Gaussian scan curves ($A = 1$, $\sigma = 1$, ϵ varying).

$$\mathcal{R}(\Delta x) = A\frac{2^{-\frac{3+\epsilon}{2+\epsilon}}}{\sigma\,\Gamma\left(1+\frac{1}{2+\epsilon}\right)}\exp\left(-\frac{1}{2}\left(\frac{\Delta x^2}{\sigma^2}\right)^{1+\frac{\epsilon}{2}}\right) \tag{5.28}$$

where Γ is the gamma function and $\epsilon > -1$. Considering that

$$\int_{-\infty}^{\infty}\mathcal{R}(\Delta x)d(\Delta x) = A \quad \text{and} \quad \mathcal{R}(0) = A\frac{2^{-\frac{3+\epsilon}{2+\epsilon}}}{\sigma\,\Gamma\left(1+\frac{1}{2+\epsilon}\right)} \tag{5.29}$$

the evaluation of Σ_x yields

$$\Sigma_x = \frac{1}{\sqrt{2\pi}}\cdot\frac{\int_{-\infty}^{\infty}\mathcal{R}(\Delta x)d(\Delta x)}{\mathcal{R}(0)} = \frac{2^{\frac{1}{2}+\frac{1}{2+\epsilon}}}{\sqrt{\pi}}\sigma\,\Gamma\left(1+\frac{1}{2+\epsilon}\right) \tag{5.30}$$

Figure 5.4 illustrates Super Gaussian scan curves for different parameter sets. For ϵ=0 the function reduces to a common Gaussian. For larger ϵ the edges of the distribution become more steep, ultimately resulting in a rectangular shape. For smaller ϵ the function developes a sharp peak.

5.3. Generalisation

In the previous sections, the main VdM scan formulae were derived under the assumption of uncorrelated particle densities of the bunches in the x and y plane. However, the VdM scan procedure can be generalised to arbitrary density profiles as proved in [33]. The

generalised version of equation (5.16) reads:

$$\mathcal{L}(\Delta x_0, \Delta y_0) = n_1 n_2 f_r n_b \frac{\mathcal{R}(\Delta x_0, \Delta y_0)}{\iint_{-\infty}^{\infty} \mathcal{R}(\Delta x, \Delta y) d(\Delta x) d(\Delta y)} \tag{5.31}$$

and, correspondingly, the expression for σ_{vis} is:

$$\sigma_{vis} = \frac{\mathcal{R}(\Delta x_0, \Delta y_0)}{\mathcal{L}(\Delta x_0, \Delta y_0)} = \frac{\iint_{-\infty}^{\infty} \mathcal{R}(\Delta x, \Delta y) d(\Delta x) d(\Delta y)}{n_1 n_2 f_r n_b} \tag{5.32}$$

One should note, that Σ_x and Σ_y are not well defined anymore since they may depend on the transverse separation in the non-scan plane. In general, the determination of the rate integral requires a time-consuming grid scan over the two-dimensional separation plane. Grid scans are considered impractical at the LHC because of their duration. Therefore the change of the density profiles over time can not be neglected anymore like for common VdM scans.

Crossing angle

The VdM scan procedure remains valid for collisions with a crossing angle, if the luminosity equation (5.31) is slightly modified [42]:

$$\mathcal{L}(\Delta x_0, \Delta y_0) = \gamma_\perp n_1 n_2 f_r n_b \frac{\mathcal{R}(\Delta x_0, \Delta y_0)}{\iint_{-\infty}^{\infty} \mathcal{R}(\Delta x, \Delta y) d(\Delta x) d(\Delta y)} \tag{5.33}$$

where the factor $\gamma_\perp$ is given by

$$\gamma_\perp = \left[1 - \left(\frac{v \sin \Phi/2}{c}\right)^2\right]^{-\frac{1}{2}} \tag{5.34}$$

All variables are defined as in chapter 4. For nominal design LHC parameters ($\Phi = 285\,\mu$rad and $v \approx c$) the factor $\gamma_\perp$ evaluates to $1 + 10^{-8}$. In chapter 4 the luminosity reduction for a crossing angle of $\Phi = 285\,\mu$rad was found to be 17 %. Although it may seem contradictory that $\gamma_\perp$ and the luminosity reduction factor are not identical, the VdM procedure still works for the following reason: the drop of $\mathcal{L}(\Delta x_0, \Delta y_0)$ caused by the crossing angle is reflected in a VdM scan by a widening of the scan curve measured in the crossing plane. The VdM scans evaluated in this thesis were carried out with a nominal crossing angle of zero. Hence the impact of a possible residual crossing angle is negligible.

6. Important instrumentation during Van der Meer scans

This chapter gives an overview of the important LHC beam instrumentation in the context of VdM scans. Additionally, it is explained how the raw counting rates measured by the main ATLAS luminosity detectors, BCM and LUCID, are converted to a quantity proportional to the luminosity. The VdM luminosity formula for beams made up of particle bunches is given in equation (5.19):

$$\mathcal{L}(0,0) = \frac{n_1 n_2 f_r n_b}{2\pi \Sigma_x \Sigma_y} \tag{6.1}$$

This formula allows to calculate the total luminosity for n_b colliding bunch pairs, which on average have the convolved profiles Σ_x and Σ_y and current product $n_1 n_2$. Because equation (5.19) relies on bunch-averaged parameters, it is applicable only to BCID-blind detectors. Since the emittances and hence the transverse sizes at the IP vary among the bunches, and since furthermore each bunch contains a different number of protons, it is important for the purpose of absolute luminosity determination to treat each bunch individually. Correspondingly to equation (5.19), the luminosity for a single colliding bunch pair is

$$\mathcal{L}^{(i)}(0,0) = \frac{n_1^{(i)} n_2^{(i)} f_r}{2\pi \Sigma_x^{(i)} \Sigma_y^{(i)}} \tag{6.2}$$

where the index (i) denotes the integer labelled colliding bunch pair i. The per-bunch visible cross sections are given by:

$$\sigma_{vis}^{(i)} = \frac{2\pi \Sigma_x^{(i)} \Sigma_y^{(i)}}{n_1^{(i)} n_2^{(i)} f_r} \mathcal{R}^{(i)}(0,0) = \frac{2\pi \Sigma_x^{(i)} \Sigma_y^{(i)}}{n_1^{(i)} n_2^{(i)}} \mu_{vis}^{(i)}(0,0) \tag{6.3}$$

Even though per-bunch measurements are technically more challenging than bunch-integrating ones, they enable simultaneous and independent measurements of the same quantity σ_{vis}. Because σ_{vis} should be independent of the bunch properties, the consistency of the different $\sigma_{vis}^{(i)}$ among the colliding bunch pairs is a valuable piece of infor-

mation for estimating the systematic uncertainties of a VdM scan calibration performed in a given LHC fill.

6.1. Bunch current measurements

The systematic uncertainties of all VdM scan calibrations carried out at the LHC in 2010 were dominated by the uncertainty on the bunch currents [43]. This triggered a major effort from the LHC and the four big LHC experiments to better understand and improve the bunch current measurements. This thesis follows the nomenclature and recommended procedures compiled by this venture as documented in [43, 44].

The LHC is equipped with eight dedicated bunch current monitors, two identical DC current transformers (DCCT) and two identical fast beam current transformers (FBCT) per ring. Typically, one system per ring and type is declared operational and the other system serves as a spare system or is used for development. The operational system is labelled system A and the other one system B. The currents used throughout this thesis are based on FBCT_A measurements, and, since all DCCT systems were operational at the times of the VdM scans, on DCCT_A and DCCT_B measurements.

The DCCT measures the total circulating current with high precision and is insensitive to its structure. The FBCT performs bunch-by-bunch measurements, but is not as precise as the DCCT in absolute terms. For each per-bunch measurement, the FBCT integrates all protons contained within a 25 ns time window (bunch slot) centred on the nominally filled RF bucket. Due to instrumental noise, the FBCT applies a threshold to all bunch slot measurements and only slots with a signal exceeding the threshold are considered to be occupied by real proton bunches. The protons which populate nominally empty slots and are invisible to the FBCT are called *ghost charge*. As detailled in chapter 2, only every tenth RF bucket within a bunch slot is nominally occupied by protons.

The protons which are located inside a nominally filled bunch slot, but outside the nominally filled RF bucket, are called *satellite bunches*. These protons increase the measured bunch slot charge and have to be treated with care: depending on the crossing angle at the IP, these protons may or may not contribute to the luminosity. Given that the absolute FBCT calibration is less precise than the one of the DCCT, the former is only used for measuring the fractional currents and the latter one for defining the absolute scale. This method demands a measurement of the ghost charge, which is visible to the DCCT, but invisible to the FBCT. Expressing the outlined procedure in a formula, one writes for the individual bunch currents $n^{(j)}$:

$$n^{(j)} = (n_{total} - n_{ghost}) \cdot \frac{s^{(j)}}{\sum_{j=1}^{N} s^{(j)}} \tag{6.4}$$

where n_{total} is the total bunch current measured by the DCCT and n_{ghost} the ghost charge. Because the FBCT signal $s^{(j)}$ is assumed to be proportional to the current of bunch (j), $\frac{s^{(j)}}{\sum_{j=1}^{N} s^{(j)}}$ reflects the fractional bunch current. N is the total number of bunches, including colliding and non-colliding ones. Even though not explicitly indicated in equation (6.4), the formula must be applied independently to each beam.

The LHC DC current transformers

The DCCTs were built at CERN according to the specifications defined in [45] and measure the total circulating current based on the fluxgate magnetometer principle [46]. The front-end electronics does four measurements in parallel, each of which is optimised for a different intensity range [43, 47]. In that way, the DCCT measurements cover a wide dynamic range. Dependent on the beam intensity, only one range is selected at a given time by the back-end system. The measured currents are published with a frequency of 1 Hz and stored to the LHC Logging Database. During each technical stop, the DCCTs are calibrated using a precise external current source. The calibration procedure assumes a linear DCCT response plus a constant measurement offset which is independent of the injected current: first the offset is evaluated by a measurement of the DCCT signal in absence of beam, afterwards a scaling factor is determined for each range based on the DCCT response to a current corresponding to 80 % of the upper limit of the range. The stability of the scale factors over time and various other possible uncertainty sources were studied in detail in [48]. This document also contains a quantitative evaluation of the DCCT uncertainties under different beam conditions.

The LHC Fast Beam Current Transformers

Like the DCCTs, the FBCTs were designed according to the specifications in [45]. The bunch current measurements are based on a 40 MHz response which is proportional to the number of protons in a bunch slot. First the signal is split and processed in a dynamic low and high gain range; afterwards it is used for measurements in two bandwidths. Bunch-by-bunch currents are measured by the 200 MHz channel, and turn-based measurements are performed by the 2 MHz channel. The fractional bunch currents used in this thesis were taken with the low gain from the high bandwidth channel. The front-end controller was configured such that each published bunch current is averaged

over 900 consecutive turn-by-turn measurements. The main systematic uncertainties affecting the measurements are [49]:

Orbit position dependency In a study during a dedicated LHC fill, the dependency of the FBCT measurements on the beam orbit position was found to be 1 %/mm. Since the variation of the beam orbit at the location of the FBCTs during a VdM scan is typically about 0.1 mm, the uncertainty on the absolute FBCT measurements is approximately 0.1 %. Under the assumption, that all bunches are affected in the same way, the effect on the fractional currents is negligible.

Bunch length dependency Beginning of 2011, a dependency of the FBCT bunch current measurements on the longitudinal bunch length was observed. Later that year, the effect was understood and mitigated by improvements of the front-end electronics. As a consequence, its effect on the VdM scan calibrations in 2012 is negligible.

Clock phase dependency The FBCT measurements are synchronised to the beam structure based on the 40 MHz clock signal created by the RF system. Even though both system are located close to each other at Point 4, the clock signal is routed via the LHC control room to allow snapshots of the bunch currents synchronised to events like the injection of protons into the LHC. A consequence of the rerouting are slow drifts of the clock signals on the order of a few nano seconds. The origin of the drifts are temperature dependent cable lengths. Because the optimal clock phase is verified at the start of each VdM scan fill, its effect on the FBCT performance during VdM scans is negligible.

Non-linear response It may be possible that the FBCT has a non-linear response to the bunch currents. This would distort the absolute as well as the fractional current measurements.

In order to estimate the overall uncertainties originating from the FBCTs, especially the possible non-linear response, the FBCT measurements at the time of the VdM scans are compared to measurements of a completely independent system: the ATLAS BPTX system which is described in [50, 51]. For more information about the FBCTs, the reader is referred to [52, 49].

Ghost charge

The amount of present ghost charge during a VdM scan is measured by the LHCb experiment as detailled in [53, 54, 55]. The measurement is based on reconstructing

and counting interaction vertices of circulating protons with residual gas, also known as beam gas imaging. Through analysing the direction of participating tracks and the vertex coordinate along the z-axis, it is possible to distinguish beam-gas interactions from beam-beam interactions. Additionally, the overall orientation of tracks is utilised to decide on whether a beam-gas interaction was caused by a proton of beam 1 or beam 2. In the following two classes of bunch crossings are defined for beam 1: empty crossings are crossings of nominally empty bunch slots, unpaired beam 1 crossings are crossings of a nominally filled beam 1 bunch slot with a nominally empty beam 2 slot. Correspondingly, $R^{(1)}_{empty}$ is defined as the rate of beam 1-gas interactions summed over all empty crossings and $R^{(1)}_{unpaired}$ as the rate of beam 1-gas interactions summed over all beam 1 unpaired crossings. Under the premise, that the number of beam 1-gas interactions is proportional to the number of protons in beam 1, and that this proportionality is identical for empty and unpaired crossing, one can express the ghost charge in beam 1 as

$$n^{(1)}_{ghost} = \frac{R^{(1)}_{empty}}{R^{(1)}_{unpaired}} \cdot n^{(1)}_{unpaired} \tag{6.5}$$

where $n^{(1)}_{unpaired}$ can be measured by the FBCT and is the intensity summed over all unpaired beam 1 crossings. The expression for $n^{(2)}_{ghost}$ is analogous. The main uncertainties of this method originate from a dependency of the trigger efficiency on the vertex location and on the interaction time. The latter varies for different RF buckets and the interactions can have different phases with respect to the 40 MHz LHC clock. The clock period of 25 ns also is the reason, why satellite bunches are invisible to LHCb: this would require a timing resolution of 2.5 ns. To achieve better statistics, LHCb is able to degrade the vacuum at the IP by injecting small amounts of neon gas into the beam pipe, thus increasing the rate of beam-gas interactions.

Satellite bunches

The measurement of satellite bunches is based on the detection of synchrotron radiation (SR) with the LDMs[1] which are located at Point 4 [53, 56]. The principle of the measurement is that the time structure of the synchrotron photons is identical to the time structure of the longitudinal beam charge density. The SR is extracted from the beam pipe through a silica window. Using various optical elements, it is directed onto the silicon avalanche photo diode of the LDM. The photo diode is operated in Geiger mode and does single photon counting with a high time resolution. After each hit, the

[1] *Longitudinal Density Monitor*

LDM is not able to detect further photons for a dead time of 77 ns; taking this and other instrumental effects into account, the optimal average number of photons per bunch and turn was shown to be 0.5.

The determination of the longitudinal density profile of the beam corresponds to filling the arrival time of each detected photon into a histogram. Its bins have a width of 50 ps and many turns must be acquired before visible bunch profiles can develop. An integration time of 10 s allows to measure the longitudinal main bunch profiles; satellite bunch measurements require an integration time of more than 300 s. In order to quantify the fraction of satellite charges for a given bunch slot, one compares the number of SR photons corresponding to the RF bucket of the main bunch with the number of SR photons corresponding to satellite RF buckets. Various detector related effects limiting the LDM performance during VdM scans are discussed in [53].

6.2. Orbit drift monitoring

One key feature of the VdM scan procedure is the stepwise transverse separation of the beams. The separation at the IP is achieved via a local distortion of the beam orbits by a closed orbit bump. Technically, this is accomplished by pairs of two steering dipoles on either side of the IP: the incoming beam is deflected twice by two dipoles having opposite magnetic fields, such that at the IP the beam is in parallel to the undistorted orbit, but transversely displaced. The outgoing beam then passes the second dipole pair which exactly cancels the effect of the first one, hence the beam again follows the undistorted orbit. The amount of separation is controlled by the dipole strength which is adjusted by the currents running through the magnet.

The transverse position of the beam at the IP is given by the position of the undistorted orbit plus the separation introduced by the local orbit bump. Therefore, drifting orbits increase or decrease the beam separation at the IP, subject to the drift direction. Normally, the scan curves are evaluated based on the nominal separation, that is the separation caused by the orbit bumps. Hence the effect of drifting orbits on the VdM scan procedure is twofold:

- A drift in the scan plane leads to a deformation of the scan curve. If the orbits drift with a constant velocity and if the scan point measurements are equidistant in separation and time, the distortion is identical to a narrowing or widening of the scan curve. If the scan curve is widened or narrowed depends on whether the orbits drift in beam movement direction or opposed to it. In case of uniform drifts, one can correct the scan curve distortion via a linear scaling of the nominal separation

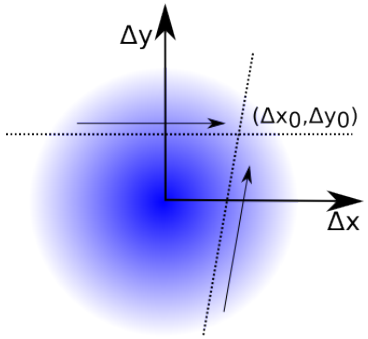

Figure 6.1.: Illustration of uniform orbit drifts in the x plane during a VdM scan. The dotted lines represent the effective horizontal and vertical separations in consideration of orbit drifts. While the drifts widen or narrow the scan curve in the horizontal scan, they tilt the vertical scan axis.

by a factor D. As a consequence, also Σ_x (or Σ_y) change by the factor D. Another interesting case is when both orbits drift alike: even though the interaction region is moving, the scan curves are not affected. In general, the impact of orbit drifts in the scan plane must be evaluated by a comparison of the distorted and undistorted scan curves. The latter is obtained by correcting the nominal separation for orbit drifts.

- A drift in the non-scan plane affects the measured scan curve in a more complicated way and is, for the case of uniform drifts, equivalent to a scan along a tilted scan axis in the $(\Delta x, \Delta y)$ separation plane as illustrated in figure 6.1. The impact of orbit drifts in the non-scan plane on the visible cross section is smaller for head-on scans than for offset scans, during which the beams are separated in the non-scan plane. This can be understood from the fact, that for bell shaped beam profiles the variation of luminosity with transverse beam separation is minimal for centred beams.

Because a VdM scan at the LHC always comprises a horizontal and a vertical scan, a drift in a given plane always takes place once in the scan plane and once in the non-scan plane. Therefore both effects discussed above have to be considered in a correction procedure. One defines $d_{1x}(t)$ and $d_{2x}(t)$ as functions of time t describing the horizontal orbit drifts of beam 1 and beam 2, respectively. Accordingly, the vertical orbit drifts are given by $d_{1y}(t)$ and $d_{2y}(t)$. Furthermore, one postulates that $d_{1x}(0) = d_{2x}(0) = d_{1y}(0) = d_{2y}(0) = 0$, where the time $t = 0$ corresponds to the time of the first scan point of the x scan. This condition can always be satisfied by adding a constant to the orbit measurements. The nominal separation is $\Delta x_{nominal} = \Delta x_1 - \Delta x_2$, where Δx_1 and

Δx_2 denote the orbit displacements of beam 1 and beam 2 introduced by the separation bump. A complication is that the nominal separation scale may be shifted with respect to the real separation and zero nominal separation does not correspond to perfectly centred beams. The global shift of the nominal separation scale in the x and y plane with respect to the real separation is labelled μ_x and μ_y. Adopting the definitions just made, one can correct each scan point for orbit drifts and for the shift of the nominal separation scale, and the real separations Δx and Δy are:

$$\Delta x = \Delta x_{nominal} + [d_{1x}(t) - d_{2x}(t)] - \mu_x \tag{6.6}$$

$$\Delta y = \Delta y_{nominal} + [d_{1y}(t) - d_{2y}(t)] - \mu_y \tag{6.7}$$

In this formula t must be chosen accordingly to the time of each scan point. μ_x is chosen such that the peak value of the corrected x scan curve at time t_1 corresponds to $\Delta x = 0$. Correspondingly, μ_y is chosen, such that the peak value of the corrected y scan curve at time t_2 corresponds to $\Delta y = 0$. Recalling equation (5.20), which is used for determining σ_{vis}

$$\sigma_{vis} = \frac{2\pi\Sigma_x\Sigma_y}{n_1 n_2 f_r n_b}\frac{\mathcal{R}(0,\Delta y_0)\mathcal{R}(\Delta x_0, 0)}{\mathcal{R}(\Delta x_0, \Delta y_0)} \tag{6.8}$$

one finds that the parameters Σ_x, Σ_y, $\mathcal{R}(0,\Delta y_0)$ and $\mathcal{R}(\Delta x_0, 0)$ can be directly obtained from the corrected scan curves: Σ_x and Σ_y are given by the shape of the scan curves and $\mathcal{R}(0,\Delta y_0)$ and $\mathcal{R}(\Delta x_0, 0)$ are the peak rates. The determination of the working point, and hence $\mathcal{R}(\Delta x_0, \Delta y_0)$, needs some extra thoughts. The average horizontal beam separation during the vertical scan is taken as

$$\Delta x_0 = \Delta x_{0,nominal} + [d_{1x}(t_2) - d_{2x}(t_2)] - \mu_x \tag{6.9}$$

and the average vertical beam separation during the horizontal scan as

$$\Delta y_0 = \Delta y_{0,nominal} + [d_{1y}(t_1) - d_{2y}(t_1)] - \mu_y \tag{6.10}$$

Therefore the working point $(\Delta x_0, \Delta y_0)$ corresponds to

$$\begin{aligned}(\Delta x_0, \Delta y_0) = \\ &(\Delta x_{0,nominal} + [d_{1x}(t_2) - d_{2x}(t_2)] - \mu_x \\ &, \Delta y_{0,nominal} + [d_{1y}(t_1) - d_{2y}(t_1)] - \mu_y)\end{aligned} \tag{6.11}$$

$R(\Delta x_0, \Delta y_0)$ is measured twice; during the x scan as well as during the y scan. It is obtained from the x scan as follows: the corrected scan curve is evaluated at the separation $(\Delta x_{0,nominal} + [d_{1x}(t_2) - d_{2x}(t_2)] - \mu_x)$. The determination of $R(\Delta x_0, \Delta y_0)$ from the y scan is analogous: the corrected scan curve is evaluated at the separation $(\Delta y_{0,nominal} + [d_{1y}(t_1) - d_{2y}(t_1)] - \mu_y)$. For the purpose of absolute luminosity calibration, one uses the mean of both measured rates as an input to equation (5.20).

The orbit correction presented here is an approximation based on the following simplification: even though during a scan the separation in the non-scan plane is drifting and not constant, we assume a constant effective non-scan plane separation which is given by the non-scan plane separation at the time of the scan curve peaks. The fully correct approach would involve a two-dimensional fit of the individually orbit drift corrected scan points in both planes.

A global shift of the nominal separation scale implies an offset in the non-scan plane, even if the non-scan plane offset is nominally zero. To correct for this displacement, the beams can be re-centred in the scan plane immediately after a scan. The correction is based on online scan curve fits and only performed when considered necessary. A re-centering in the horizontal plane between the x and y scan must be taken into account in the scan evaluation by adding the variable r_x to the working point derived in equation (6.11):

$$\begin{aligned}(\Delta x_0, \Delta y_0) = & \\ & (\Delta x_{0,nominal} + [d_{1x}(t_2) - d_{2x}(t_2)] - \mu_x + r_x \\ & , \Delta y_{0,nominal} + [d_{1y}(t_1) - d_{2y}(t_1)] - \mu_y)\end{aligned} \tag{6.12}$$

where r_x denotes the horizontal re-centering of the beams after the x scan. The re-centering in the vertical plane after a y scan is irrelevant for the scan evaluation, since at this time the scan is already completed.

At the LHC, orbit drifts at the IP are monitored based on data from the BPMs[2], which are devices specifically designed for measuring the transverse beam position at the BPM location. The procedure incorporates a fit to the readings of about fifty BPMs on either side of the IP in order to determine the orbit trajectory under consideration of betatron oscillations[3][57]. The beam orbit obtained from the fit is extrapolated to the IP with a magnetic model of the beam optics. The two independently obtained orbits, one from either side of the IP, allow an internal consistency check of the method and

[2] *Beam Position Monitor*

[3] Transverse oscillations of the particles about the equilibrium orbit.

are used for estimating the uncertainties associated with the orbit drift correction.

6.3. Luminosity algorithms

Based on equation (5.2), the luminosity for colliding bunch pair (i) can be written as

$$\mathcal{L}^{(i)} = \frac{\mu_{vis}^{(i)} f_r}{\sigma_{vis}} \tag{6.13}$$

where μ_{vis} is the mean visible number of interactions per bunch crossing (BC). μ_{vis} is identical to the mean number of interactions per BC μ, multiplied by the detector efficiency ϵ. The topic of this section is the conversion of raw rates measured by a detector to the quantity μ_{vis}. While the former are not necessarily proportional to the luminosity, the latter are. The conversion is done by so-called luminosity algorithms. In this thesis, the calibration constants σ_{vis} are determined for three algorithms:

BCMV_EventOR counts the events in which at least one hit is observed in any of the four vertical BCM modules, irrespective of the side.

BCMH_EventOR counts the events in which at least one hit is observed in any of the four horizontal BCM modules, irrespective of the side.

LUCID_EventOR counts the events in which at least one hit is observed in any of the LUCID tubes, irrespective of the side.

All three algorithms are BCID-aware, i.e. they allow per-bunch measurements. For both, BCM and LUCID, a hit is generated only if a signal surpasses a detector specific threshold. In case of BCM, a hit moreover is required to happen within a time window of 12.5 ns width, which is centred on the expected arrival time of particles coming from the IP. In order not to be sensitive to effects like migration, the thresholds are chosen considering signal sensitivity and noise rejection. Migration describes an effect, which causes the generation of a hit when two or more particles traverse the detector, even though none of the particle alone would have caused a signal above threshold. To avoid migration, the detector should be sensitive even in the lower range of the energy spectrum of the detectable particles and, additionally, the signal threshold should be low enough such that a particle traversing the detector reliably generates a hit.

The conversion of EventOR rates to μ_{vis} is based on two fundamental assumptions:

1. The distribution of the number of proton-proton interactions per BC is a Poisson distribution.

2. The efficiency to detect a single proton-proton interaction in a BC is independent of the total number of interactions in the BC. In that case, the efficiency ϵ_n for detecting an event with n proton-proton interactions is

$$\epsilon_n = 1 - (1 - \epsilon)^n \tag{6.14}$$

where ϵ is the efficiency to detect an event with exactly one proton-proton interaction. Because equation (6.14) is not valid in case of migration, migration effects for LUCID algorithms were studied by means of Monte Carlo simulations [58].

Using the Poisson distribution, the probability that n proton-proton interactions occur in a single BC is given by:

$$P(n, \mu) = \frac{\mu^n e^{-\mu}}{n!} \tag{6.15}$$

where μ is the mean number of interactions per BC. The probability of a BC, in which at least one interaction occurs, is identical to the zero interaction probability subtracted from unity:

$$P(n > 0, \mu) = 1 - P(0, \mu) = 1 - \frac{\mu^0 e^{-\mu}}{0!} = 1 - e^{-\mu} \tag{6.16}$$

However, given that a luminosity detector has a limited efficiency, the probabilities $P(0, \mu)$ or $P(n > 0, \mu)$ are difficult to determine experimentally. Instead one considers the probability P_{EventOR} for observing any interaction in a BC, taking the detection efficiency ϵ_n into account:

$$P_{\text{EventOR}} = \sum_{n=1}^{\infty} \epsilon_n \cdot P(n, \mu) \tag{6.17}$$

$$= \sum_{n=1}^{\infty} (1 - (1 - \epsilon)^n) \cdot \frac{\mu^n e^{-\mu}}{n!} \tag{6.18}$$

$$= 1 - e^{-\epsilon\mu} \tag{6.19}$$

A more detailed derivation of this result can be found in appendix A. Considering that $\epsilon\mu = \mu_{vis}^{OR}$, one is able express equation (6.17) in terms of μ_{vis}^{OR}:

$$P_{\text{EventOR}}(\mu_{vis}^{OR}) = 1 - e^{-\mu_{vis}^{OR}} \tag{6.20}$$

For $\mu_{vis}^{OR} \ll 1$, this probability is $P_{\text{EventOR}}(\mu_{vis}^{OR}) \approx \mu_{vis}^{OR}$. This complies with the

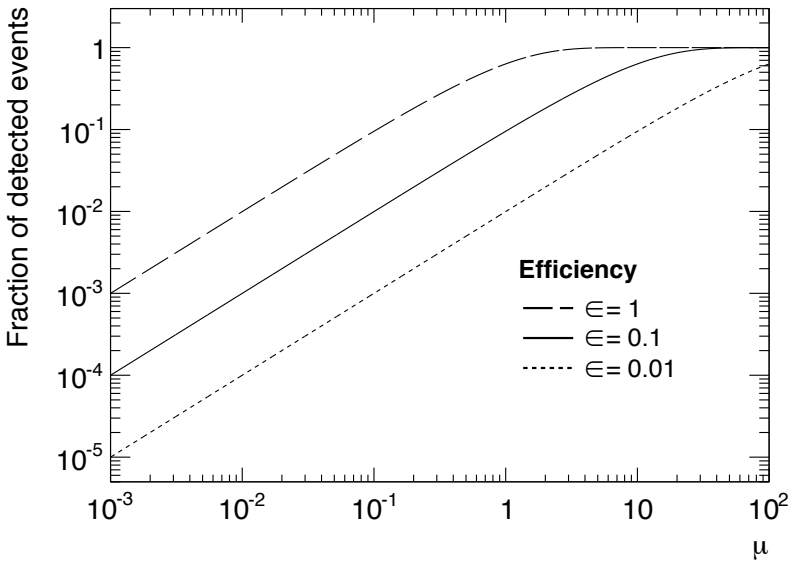

Figure 6.2.: Fraction of detected events with the EventOR algorithm for different detector efficiencies.

expectations, since for very small μ_{vis}^{OR} a double hit is unlikely. P_{EventOR} is experimentally determined through dividing the number of observed OR-events N_{OR} by the total number of bunch crossings N_{BC}:

$$P_{\text{EventOR}} = \frac{N_{OR}}{N_{BC}} \tag{6.21}$$

After combining equation (6.20) and (6.21) and solving for μ_{vis}^{OR}, one obtains the main result:

$$\mu_{vis}^{OR} = -\ln\left(1 - \frac{N_{OR}}{N_{BC}}\right) \tag{6.22}$$

Figure 6.2 illustrates the dependency of P_{EventOR} on μ for different detector efficiencies. A striking feature is the flattening of the curves for large values of μ. Dependent on ϵ, the flattening happens at different μ-values. This effect is called saturation and implies the loss of the algorithm precision. Low efficiency detectors saturate at higher pile-up levels than detectors having a high detection efficiency.

Besides the EventOR algorithms, also other type of algorithms were employed by ATLAS throughout the year 2012:

Single-sided EventOR Algorithms using only detector modules on either the A-side or the C-side of the IP. The conversion of event rates to $\mu_{vis}^{OR,Single}$ is analogous to the

double-sided case:

$$\mu_{vis}^{OR,Single} = -\ln\left(1 - \frac{N_{OR,Single}}{N_{BC}}\right) \tag{6.23}$$

EventAND Coincidence algorithms requiring at least one hit on the A-side and one hit on the C-side. For equal A-side and C-side efficiencies, the conversion of event rates to μ_{vis}^{AND} is based on the relation [58]:

$$\frac{N_{AND}}{N_{BC}} = 1 - 2e^{-(1+\sigma_{vis}^{OR}/\sigma_{vis}^{AND})\mu_{vis}^{AND}/2} + e^{-(\sigma_{vis}^{OR}/\sigma_{vis}^{AND})\mu_{vis}^{AND}} \tag{6.24}$$

where σ_{vis}^{OR} and σ_{vis}^{AND} are the visible cross sections corresponding to the EventOR and EventAND algorithms, respectively. The calculation of μ_{vis}^{AND} relies on a numerical inversion, since no analytical expression of μ_{vis}^{AND} in terms of $\frac{N_{AND}}{N_{BC}}$ is known. The main advantage of requiring a coincidence is the efficient beam background rejection. A consequence of requiring coincident hits is the efficiency decrease, defined by the ratio $\sigma_{vis}^{OR}/\sigma_{vis}^{AND}$. Hence the algorithm may be usable at higher μ-values, but also may lose precision in low pile-up conditions.

HitOR Algorithms counting the number of detector modules, which generate a hit in a BC. The summed number of hits during N_{BC} bunch crossings is denoted N_{HIT}, and the number of modules used for the hit counting is denoted $N_{Modules}$. Under the assumption, that the efficiency to register a hit in a given module is independent of the number of hits in other modules, the conversion of event rates to μ_{vis}^{HIT} can be done via a formula similar to the one used for EventOR algorithms:

$$\mu_{vis}^{HIT} = -\ln\left(1 - \frac{N_{HIT}}{N_{BC}N_{Modules}}\right) \tag{6.25}$$

All algorithms have different efficiencies and saturation levels. Additionally, they have different sensitivity to background. While their internal consistency in different pile-up conditions is important for quantifying the μ-dependence of the detector response, their internal consistency over time is a valuable tool for monitoring and quantifying the long-term stability.

7. Analysis of the 2012 Van der Meer scans

In the year 2010 and 2011 ATLAS successfully carried out VdM scans [58, 17, 59]. During the year 2012, ATLAS performed three luminosity calibration campaigns based on VdM scans: the first campaign took place on April 16, the second on July 19, and the third on November 22 and November 25.

The configuration of the April 2012 VdM scans differed in some fundamental aspects from the configuration of the two later 2012 scan campaigns: while the April scans were taken with physics beam optics ($\beta^* = 0.6\,\mathrm{m}$), the later scans were performed with injection beam optics ($\beta^* = 11\,\mathrm{m}$). The different β^* is of high relevance, since it accounts for much smaller transverse bunch sizes at the IP in the April scans compared to the July and November scans. Moreover, the peak rates during the April scans were higher than during the two later scan campaigns. Another difference is the non-zero crossing angle for the April scans; the July and November scans were carried out with a nominal crossing angle of zero.

In the context of this thesis, only the July 2012 and November 2012 VdM scans are exploited. This is motivated by the fact, that the precision of the April VdM scans can not keep up with the ones of July and November.

In this chapter, first a few comments on the April 2012 scans are made, followed by a discussion of the particle bunch configuration during the 2012 VdM scans. Afterwards the July and November VdM scans are evaluated and their systematic uncertainties are quantitatively assessed.

Comments on the April 2012 Van der Meer scans

In April 2012 ATLAS performed three VdM scans; all took place in the same fill and consisted of an x scan directly followed by a y scan. Albeit all three scans went according to plan, a significant non-reproducibility of the calibration constant σ_{vis} was observed. The variation pattern was similar among the luminosity algorithms based on either BCM or LUCID. After eliminating many sources of systematic uncertainties, the

non-reproducibility was attributed to non-factorisation of the transverse bunch density profiles into independent x and y components, or equivalent, to non-factorisation of the luminosity into independent Δx and Δy components. This suspicion was backed up by the outcome of the July VdM scans, for which the non-factorisation was assessed experimentally.

Two possibilities for studying transverse correlations are: 1. analysis of the luminous region and its dependency on the transverse separation via reconstructed interaction vertices, 2. comparison of the convolved bunch sizes Σ_x and Σ_y obtained in centred scans and in offset scans. While both kind of studies are feasible for the scans with injection optics, neither is possible for the April scans: the April scan campaign did not involve offset scans and many features of the luminous region were concealed by the vertex resolution. It is different for each vertex, but on average about $60\,\mu$m. This must be compared to the transverse size of the luminous region of about $12\,\mu$m in April and $70\,\mu$m in July and November.

In contrast to the July and November VdM scans, the small β^* and the non-zero crossing during the April scans imply two effects which are detailed below:

- The impact of the hourglass effect on VdM scans without a crossing angle for particle bunches with Gaussian density profiles is discussed in [60]. Qualitatively, the hourglass effect impacts the VdM scan procedure in the following way: the widened transverse beam profiles at coordinates with $|z| > 0$ cause a drop of the peak luminosity, but also cause an increase of the measured convolved bunch sizes Σ_x and Σ_y. The key parameter for describing the magnitude of the impact of the hourglass effect on the VdM scan procedure is the ratio β^*/σ_z, which was already introduced in chapter 4.

  An additional complication is a non-zero crossing angle, since the luminous region moves away from the nominal IP when separating the beams in the crossing plane. Within the ATLAS experiment, the luminous region is often referred to as beamspot. As no analytical expression is known for the impact of the hourglass effect on VdM scans with non-zero crossing angle, the bias must be evaluated based on simulations. Figure 7.1 illustrates the dependency of the position and size of the beamspot on the vertical separation for conditions similar to those during the April scans. The beamspot features are shown in two versions: one accounts for the hourglass effect, and one neglects it. The beamspot simulation is based on numerical integration.

  One observes, that the transverse size of the luminous region increases with separation when taking the hourglass effect into account. This can be understood

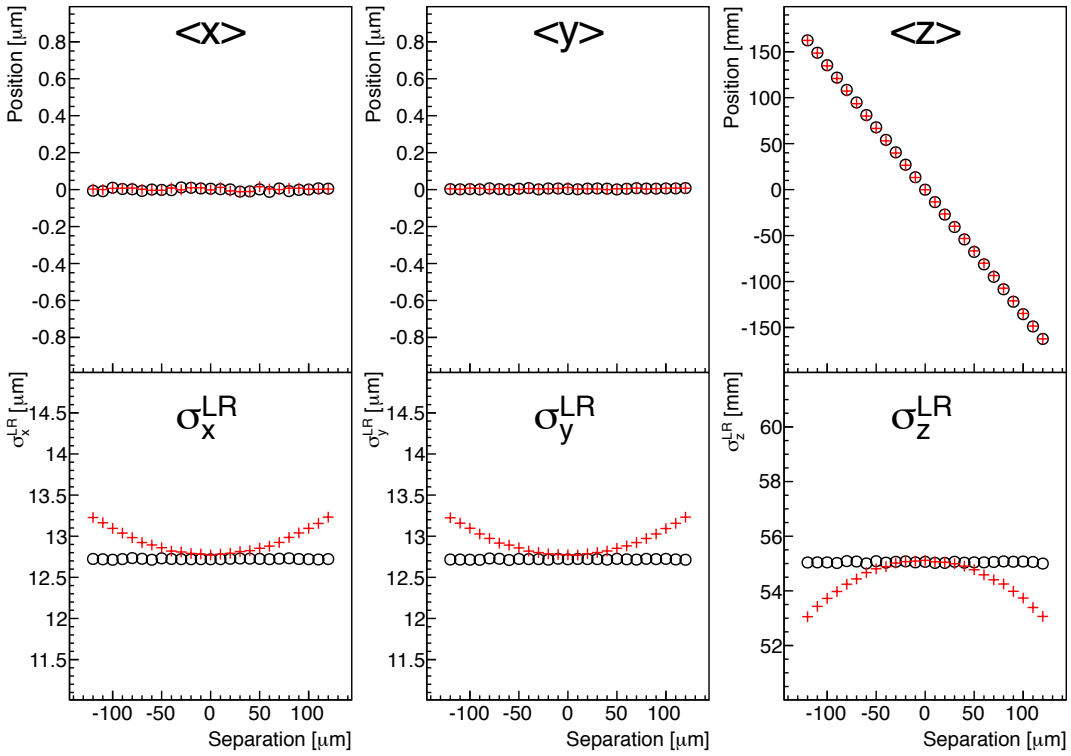

Figure 7.1.: Beamspot position and size during a simulated y scan for colliding particle bunches with Gaussian density profiles. The simulation parameters were chosen according to the April scan conditions in ATLAS. The black open circles correspond to data neglecting the hourglass effect, the red crosses to data taking it into account. $\langle x \rangle$, $\langle y \rangle$, $\langle z \rangle$ denote the coordinates of the beam spot centroid; σ_x^{LR}, σ_y^{LR}, σ_z^{LR} denote the standard deviations of the luminous region along the x, y and z-axis. Main simulation parameters: $\sigma_{1x}^* = \sigma_{2x}^* = \sigma_{1y}^* = \sigma_{2y}^* = 18\,\mu$m, $\sigma_{1z}^* = \sigma_{2z}^* = 10\,$cm, $\Phi_{x\text{-}z} = 290\,\mu$rad, $\beta^* = 0.6\,$m.

from the fact, that for non-zero separation the beams collide in a region of less strong focussing; the upper right plot of figure 7.1 demonstrates, that the beamspot centroid moves during the scan in the crossing plane up to 15 cm away from the nominal interaction point.

The non-optimal focussing also impacts the interaction rate, which decreases compared to the case of neglected hourglass effect. Therefore, the scan curves in the crossing plane widen. Based on the simulation results, an upper limit for the bias on the April calibration constants introduced by the hourglass effect is 0.1 %. For calculating the bias, the luminosity at zero transverse separation was compared to the luminosity derived via the VdM scan procedure. The former is directly obtained from the simulation and the latter is based on the simulated scan curves.

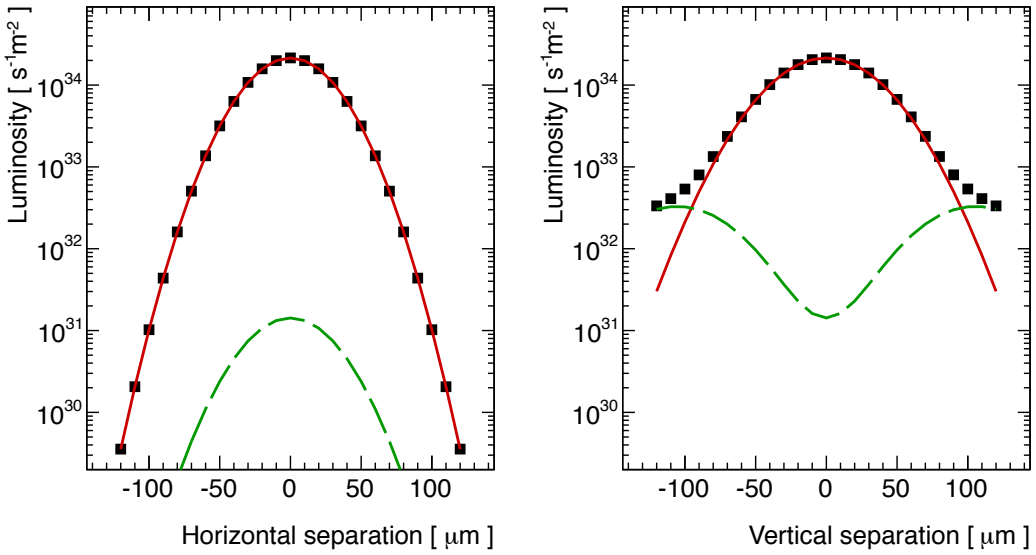

Figure 7.2.: Horizontal and vertical scan curves for colliding particle bunches with Gaussian density profiles in a simulated VdM scan. The simulation parameters were chosen according to the April scan conditions in ATLAS except for one modification: both RF buckets directly neighbouring the main RF buckets contain satellite bunches. The number of protons in each of those buckets corresponds to 1 % of the main bunch current. The black squares represent the luminosity as a function of separation, the red solid line illustrates the contribution of main-main bunch collisions and the green dashed line depicts the contribution of main-satellite and satellite-satellite collisions. Main simulation parameters: $\sigma^*_{1x} = \sigma^*_{2x} = \sigma^*_{1y} = \sigma^*_{2y} = 18\,\mu$m, $\sigma^*_{1z} = \sigma^*_{2z} = 10\,$cm, $\Phi_{x\text{-}z} = 290\,\mu$rad, $\beta^* = 0.6\,$m, $n_1 = n_2 = 10^{11}$ protons.

The drop of the peak luminosity is cancelled to a high degree by a widening of the scan curves.

- A non-zero crossing angle prevents collisions of main with satellite bunches during normal LHC physics operation, but gives rise to distortions of the VdM scan curves. These are caused by head-on collisions of the main bunch with satellite bunches at high beam separation. The scan curve distortion originating from satellite bunches is demonstrated in figure 7.2 for conditions similar to the April scans: while the scan curves in the non-crossing plane are only marginally affected, the tails of the scan curve in the crossing-plane are strongly enhanced. The satellite bunch current in the simulation was fixed to 1 % of the main bunch current. Even though the fractional satellite bunch currents at the LHC are often less than 1 %, it is crucial to monitor satellite bunches during VdM scans.

Particle bunch configuration during VdM scans

The particle bunch configuration during the 2012 VdM scans was different from those during regular LHC operation and was chosen in consideration of the following points:

- No long-range interactions. These are interactions of bunches at locations different from the nominal IP. They can only happen at places, where the counter-rotating beams share a common beam pipe. In order to avoid long-range interactions, one needs to operate the LHC with a wide bunch spacing. Hence, the filling scheme for VdM scan fills does not involve bunch trains[1].

- Small bunch currents in order to reduce unwanted beam-beam effects. In general, beam-beam effects increase with higher bunch currents.

- Exclusive bunches. In other words, the particle bunches colliding in ATLAS are not colliding in other IPs with the natural exception of IP5. Again, this measure aims at reducing beam-beam effects.

- Optimal FBCT performance. Another reason in support of a wide bunch spacing is the FBCT performance, which degrades for bunches within a bunch train.

- Optimal DCCT performance. The number of circulating particle bunches is chosen such that the total beam current lies in a range, for which the DCCT precision is best.

- Optimal luminosity detector performance. BCM and LUCID suffer to a different degree from afterglow background. Afterglow denotes the generation of hits in BCs succeeding the paired[2] BCs, due to slow collision remnants. The wider the bunch spacing, the smaller is the contribution of afterglow background to the measured luminosity of the paired BC.

Even though at this point, beam-beam effects are not yet commented on, they may interfere with the VdM calibration procedure in different ways: through modifying the equilibrium orbit, through exerting focussing or defocussing forces on the bunches and through increasing the emittance growth and bunch current losses.

[1] A bunch train is a sequence of filled successive bunch slots.

[2] A paired BC denotes a crossing at the IP of two filled bunch slots. This means both slots are occupied by particle bunches.

Synchronisation of luminosity detectors with scan steps

Like during normal physics operation, the beam steering during a VdM scan is conducted in the LHC control room. The beam movements during a VdM scan are controlled by a dedicated VdM scan application. This application is also responsible for the synchronisation of the ATLAS luminosity detectors with the stepwise beam separation, also called scan steps. The synchronisation between LHC and ATLAS is done via ethernet messages. During a VdM scan, the luminosity data in ATLAS is indexed by so-called PLBs[3], which are time intervals of variable length. The PLBs are integer-labelled and the start and end of a PLB are triggered by the LHC VdM scan application. The latter also publishes various flags for each PLB, which allow to easily select the PLBs relevant for the VdM scan evaluation; PLBs during which the beams move, must be excluded from the analysis.

7.1. Van der Meer scans in 2012 with injection beam optics

An overview of the main parameters for the July and November 2012 luminosity calibration campaigns is given in table 7.1. During both campaigns, ATLAS performed four head-on scans and two offset scans. In July, four scans were carried out in LHC fill 2855 and two in 2856; in November, five scans were performed in LHC fill 3311 and one in 3316. Each scan comprised an x scan which was directly followed by a y scan. The maximum mean number of interactions per BC during the July and November scans was approximately 0.5, the nominal crossing angle was zero.

Bunch filling scheme

A tabular representation of the LHC bunch filling scheme employed for both July VdM scan fills is given in table 7.2. Both beams contain 48 bunches, 35 of which are colliding in IP1 (ATLAS) and IP5 (CMS); three bunches are colliding in IP2 (ALICE) and six in IP8 (LHCb). Additionally, each beam contains four non-colliding bunches. The time between subsequent collisions is at least 40 BCIDs in each IP. Since a BCID corresponds to 25 ns, 40 BCIDs correspond to 1 μs. Table 7.2 also shows the per-bunch currents measured by the FBCT during the first July VdM scan, which are discussed in detail in the subsequent subsection.

[3] *Pseudo Luminosity Block*

	July 2012	November 2012
Energy $\sqrt{s}$ [TeV]	8	8
LHC fill number	2855	3311
	(2856)	(3316)
Number of bunches	48	39
Bunches colliding in ATLAS	35	29
Nominal β^* [m]	11	11
Beam size σ_b at IP [μm]	~ 90	~ 90
Nominal crossing angle [μrad]	0	0
Interactions/BC (μ^{max})	~ 0.5	~ 0.5
Scans	4,5,6: centred	10,11: centred
each scan comprises an	7: offset	12,13: offset
x scan followed by a y scan		14: centred
	(8: centred	(15: centred)
	9: offset)	
Number of scan steps	25	25
	(17)	(25)
Scan step duration [s]	30	30
Beam separation range	$\pm 6\sigma_b$	$\pm 6\sigma_b$

Table 7.1.: Main scan parameters for the July and November 2012 VdM scans.

The filling scheme used for both November VdM scan fills is shown in table 7.3. Both beams contain 39 bunches, 29 of which are colliding in IP1 and IP5; two bunches are colliding in IP2 and six in IP8. In each beam, two of the bunches are not colliding in any IP. Like for the July scans, the time between subsequent collisions is at least 1 μs in all IPs. Also shown are the per-bunch currents measured during the first November VdM scan.

Beam currents

This section discusses the current measurements during the July and November 2012 VdM scans. First an overview of the total currents determined by the DCCTs is given, then the bunch-by-buch measurements of the FBCTs are presented.

Total currents

Figure 7.3 depicts the evolution of the total bunch currents during the four LHC fills, in which ATLAS carried out VdM scans in July and November 2012. The shown data covers the whole fill duration and corresponds to the the time intervals, in which LHC declared stable beams. There are eight plots, one for each fill and beam. Each row of

			colliding B2 BCID						colliding B2 BCID		
BCID	$n1$	$n2$	IP1/5	IP2	IP8	BCID	$n1$	$n2$	IP1/5	IP2	IP8
1	0.80	0.99	1	-	-	1375	0.99	0.00	-	-	481
41	1.02	1.08	41	-	-	1415	0.95	0.00	-	-	521
81	0.85	0.98	81	-	-	1455	0.95	0.00	-	-	561
121	0.78	0.78	121	-	-	1495	0.77	0.00	-	-	601
161	0.81	1.07	161	-	-	1535	1.04	0.00	-	-	641
201	0.95	0.93	201	-	-	1581	0.91	0.83	1581	-	-
241	0.93	1.01	241	-	-	1621	1.06	1.07	1621	-	-
301	0.98	0.00	-	1192	-	1661	0.64	1.00	1661	-	-
341	1.01	0.00	-	1232	-	1701	0.96	1.04	1701	-	-
381	0.94	0.00	-	1272	-	1741	0.79	1.00	1741	-	-
441	0.00	1.02	-	-	-	1781	1.02	0.71	1781	-	-
481	0.00	0.82	-	-	-	1821	0.81	1.02	1821	-	-
521	0.00	1.02	-	-	-	2001	0.00	1.08	-	-	-
541	1.10	0.00	-	-	-	2041	0.00	0.97	-	-	-
561	0.00	1.00	-	-	-	2081	0.00	1.04	-	-	-
581	0.96	0.00	-	-	-	2121	0.00	0.72	-	-	-
601	0.00	0.97	-	-	-	2161	1.00	0.94	2161	-	-
621	0.98	0.00	-	-	-	2201	0.89	0.88	2201	-	-
641	0.00	0.89	-	-	-	2241	0.77	1.00	2241	-	-
661	0.91	0.00	-	-	-	2281	0.79	0.90	2281	-	-
721	1.02	1.10	721	-	-	2321	1.03	0.96	2321	-	-
761	0.80	0.70	761	-	-	2361	0.92	0.76	2361	-	-
801	0.90	1.02	801	-	-	2401	0.82	0.89	2401	-	-
841	0.73	1.03	841	-	-	2881	0.75	1.00	2881	-	-
881	0.79	1.02	881	-	-	2921	0.86	0.86	2921	-	-
921	0.94	0.84	921	-	-	2961	0.77	1.04	2961	-	-
961	0.86	0.99	961	-	-	3001	0.90	0.99	3001	-	-
1192	0.00	0.83	-	-	-	3041	0.77	1.02	3041	-	-
1232	0.00	1.01	-	-	-	3081	0.97	0.93	3081	-	-
1272	0.00	1.06	-	-	-	3121	0.86	0.97	3121	-	-
1335	1.01	0.00	-	-	441						

Table 7.2.: Bunch filling scheme employed for the July 2012 scans. The bunch currents $n1$ and $n2$ are given in units of 10^{11} protons and are averaged over the duration of the first July 2012 scan (scan 4).

			colliding B2 BCID						colliding B2 BCID		
BCID	$n1$	$n2$	IP1/5	IP2	IP8	BCID	$n1$	$n2$	IP1/5	IP2	IP8
1	0.79	0.90	1	-	-	1232	0.00	0.84	-	-	-
41	0.93	0.99	41	-	-	1335	0.81	0.00	-	-	441
81	0.81	1.06	81	-	-	1375	0.88	0.00	-	-	481
121	0.97	1.03	121	-	-	1415	0.98	0.00	-	-	521
161	0.95	0.87	161	-	-	1455	0.88	0.00	-	-	561
201	0.96	0.89	201	-	-	1495	0.96	0.00	-	-	601
241	0.81	0.86	241	-	-	1535	0.85	0.00	-	-	641
301	0.89	0.00	-	1192	-	1581	0.80	1.02	1581	-	-
341	0.86	0.00	-	1232	-	1621	0.83	1.04	1621	-	-
441	0.00	0.88	-	-	-	1661	1.05	0.76	1661	-	-
481	0.00	0.86	-	-	-	1701	0.94	0.91	1701	-	-
521	0.00	0.90	-	-	-	1741	0.78	0.82	1741	-	-
541	0.83	0.00	-	-	-	1781	0.89	1.00	1781	-	-
561	0.00	1.02	-	-	-	1821	1.02	1.00	1821	-	-
581	1.02	0.00	-	-	-	2001	0.00	0.86	-	-	-
601	0.00	0.84	-	-	-	2041	0.00	0.83	-	-	-
641	0.00	0.88	-	-	-	2161	1.00	0.77	2161	-	-
721	0.85	0.85	721	-	-	2201	1.09	0.82	2201	-	-
761	1.06	0.91	761	-	-	2241	0.84	0.77	2241	-	-
801	0.99	0.89	801	-	-	2281	0.90	1.09	2281	-	-
841	1.07	1.13	841	-	-	2321	0.98	0.91	2321	-	-
881	1.01	0.89	881	-	-	2361	0.89	0.85	2361	-	-
921	0.92	0.84	921	-	-	2401	0.84	0.82	2401	-	-
961	0.90	0.93	961	-	-	2881	1.01	1.00	2881	-	-
1192	0.00	0.77	-	-	-						

Table 7.3.: Bunch filling scheme employed for the November 2012 scans. The bunch currents $n1$ and $n2$ are given in units of 10^{11} protons and are averaged over the duration of the first November 2012 scan (scan 10).

plots corresponds to one fill, where the left plots refer to beam 1 and the right ones to beam 2 currents. All plots are built-up of two panels. The upper ones show the total bunch currents measured by the $\mathrm{DCCT_A}$, the $\mathrm{DCCT_B}$ and the FBCT, the lower ones illustrate the agreement of the average of both DCCT measurements with the total current measurements of the FBCT. Even though the FBCT measures per-bunch currents, the total currents can be calculated by summing up the bunch currents.

An interesting feature can be observed during fill 3311 for the beam 2 measurements: at about 20:30h in Geneva local time, the ratio of the FBCT to the DCCT measurements abruptly jumps by $+0.2\,\%$. When looking at the absolute intensities, one can identify the FBCT as the origin of the jump. Because at the time of the jump, part of the FBCT infrastructure was being restarted, the jump is attributed to instrumental rather than real beam effects.

One reason for the good agreement of the absolute FBCT measurements with the DCCT ones is the wide bunch spacing in VdM scan fills, another reason is the cross-calibration of the FBCT with the DCCT at the beginning of the fills. The deviation between absolute FBCT and DCCT measurements is of high relevance for the VdM scan analysis. Instead of rescaling the FBCT bunch-by-bunch fractions accordingly to the absolute DCCT scale, the calibration constants σ_{vis} are determined based on uncorrected FBCT measurements. Only at the last step of the VdM scan analysis, the σ_{vis} are corrected for the deviation between FBCT and DCCT measurements. This course of action aims at simplifying the analysis. One should note, that the σ_{vis} correction also must take satellite bunches and ghost charges into account. The overall current correction factors for the July and November scans are listed in table 7.4 and discussed at a later stage.

Bunch-by-bunch currents

Figure 7.4 and 7.5 depict the evolution of the per-bunch currents during the July and November VdM scans, respectively. The shown time intervals are identical to the ones in figure 7.3. Again there are eight plots, one for each fill and beam. Each row of plots corresponds to one fill, where the left plots refer to beam 1 and the right ones to beam 2 currents. All plots comprise two panels. The upper ones show the absolute per-bunch currents measured by the FBCT, the lower ones illustrate the current decay over time.

For better readability, the bunches are divided into different categories according to their collision configuration:

- **IP1/5** Group of bunches colliding only in IP1 (ATLAS) and IP5 (CMS).

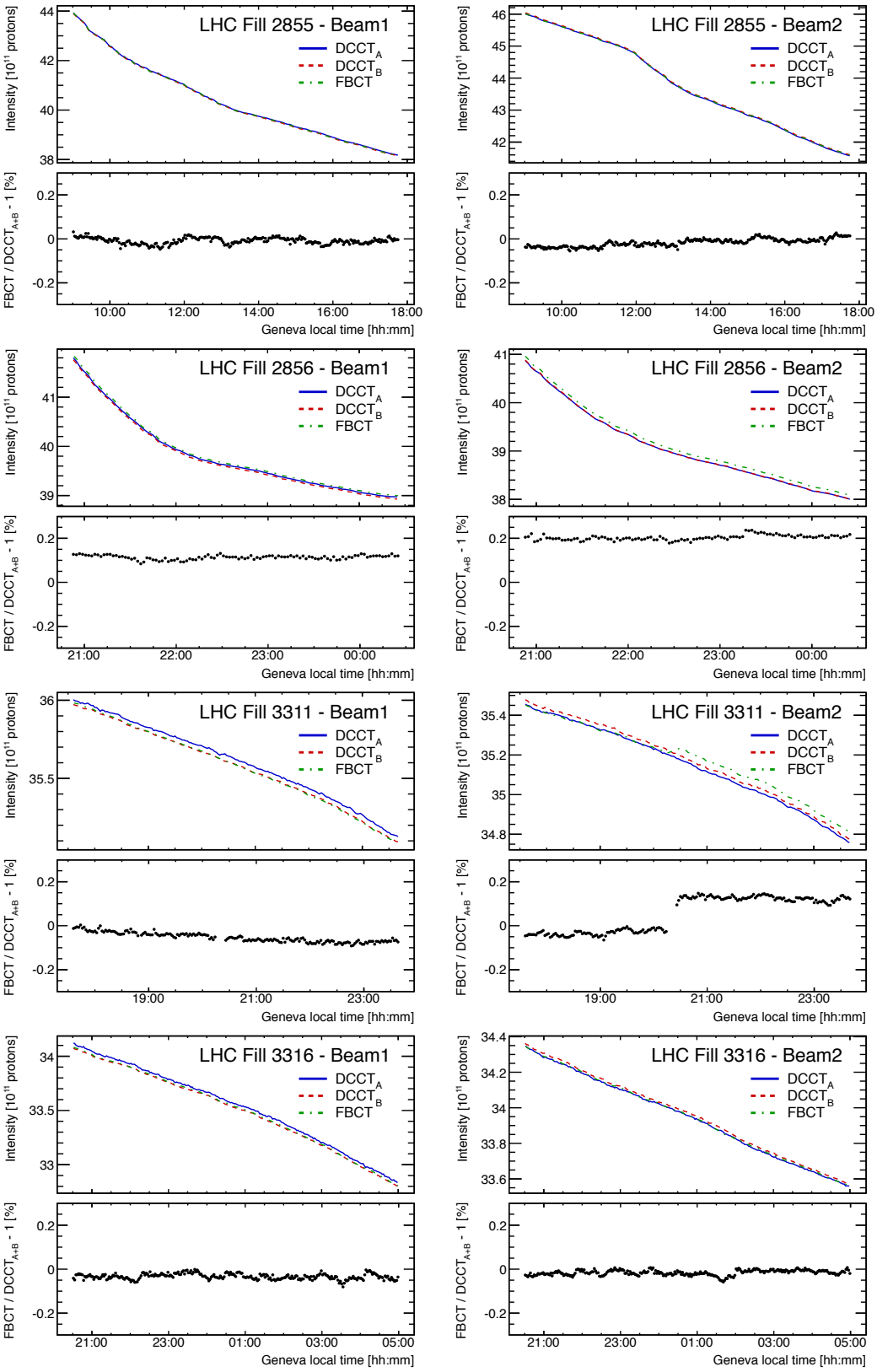

Figure 7.3.: Total bunch currents during the LHC fills, in which the July and November VdM scans took place. The upper four plots correspond to the July fills, the lower ones to the November fills.

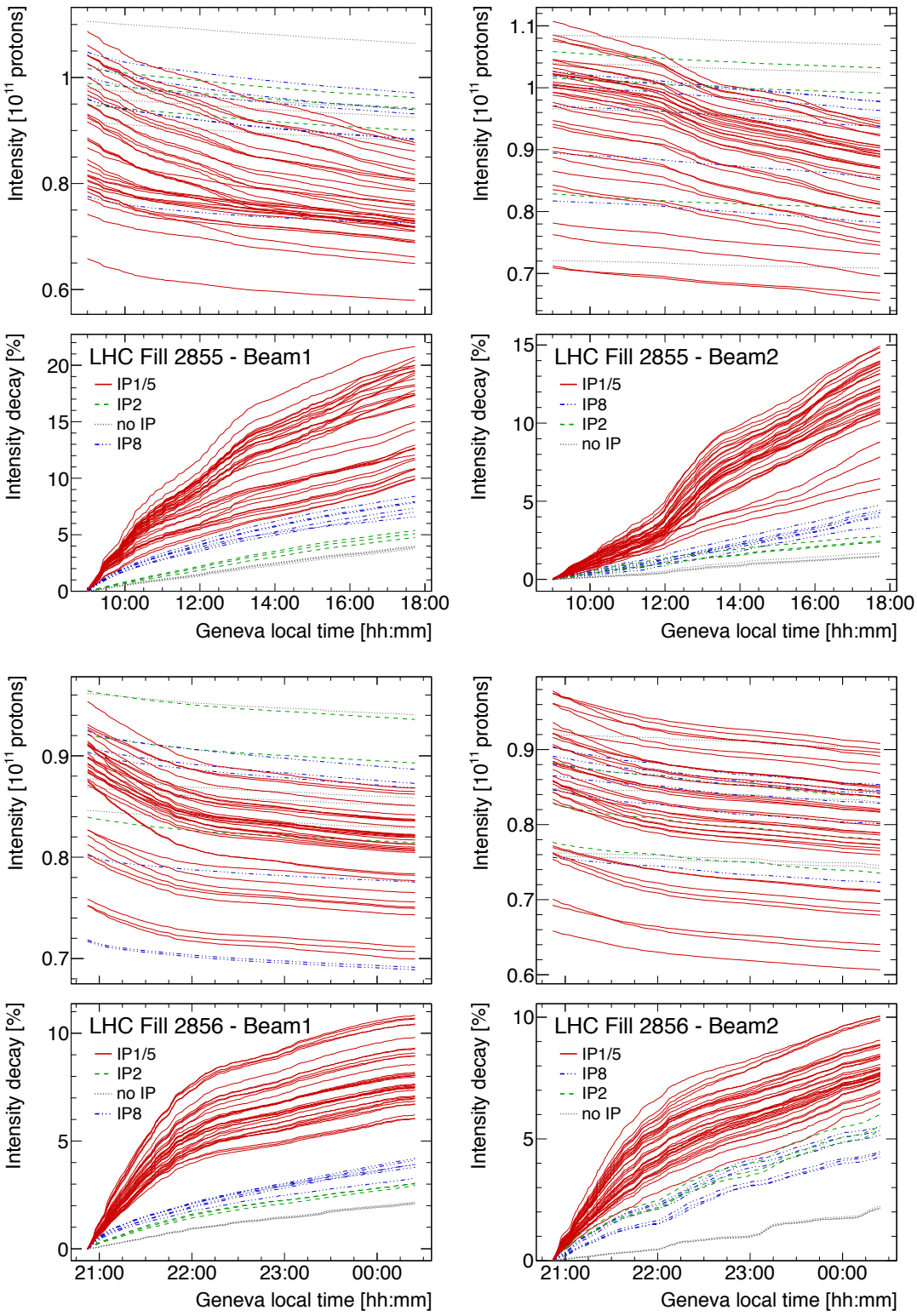

Figure 7.4.: Bunch-by-bunch currents during the LHC fills, in which the July VdM scans took place.

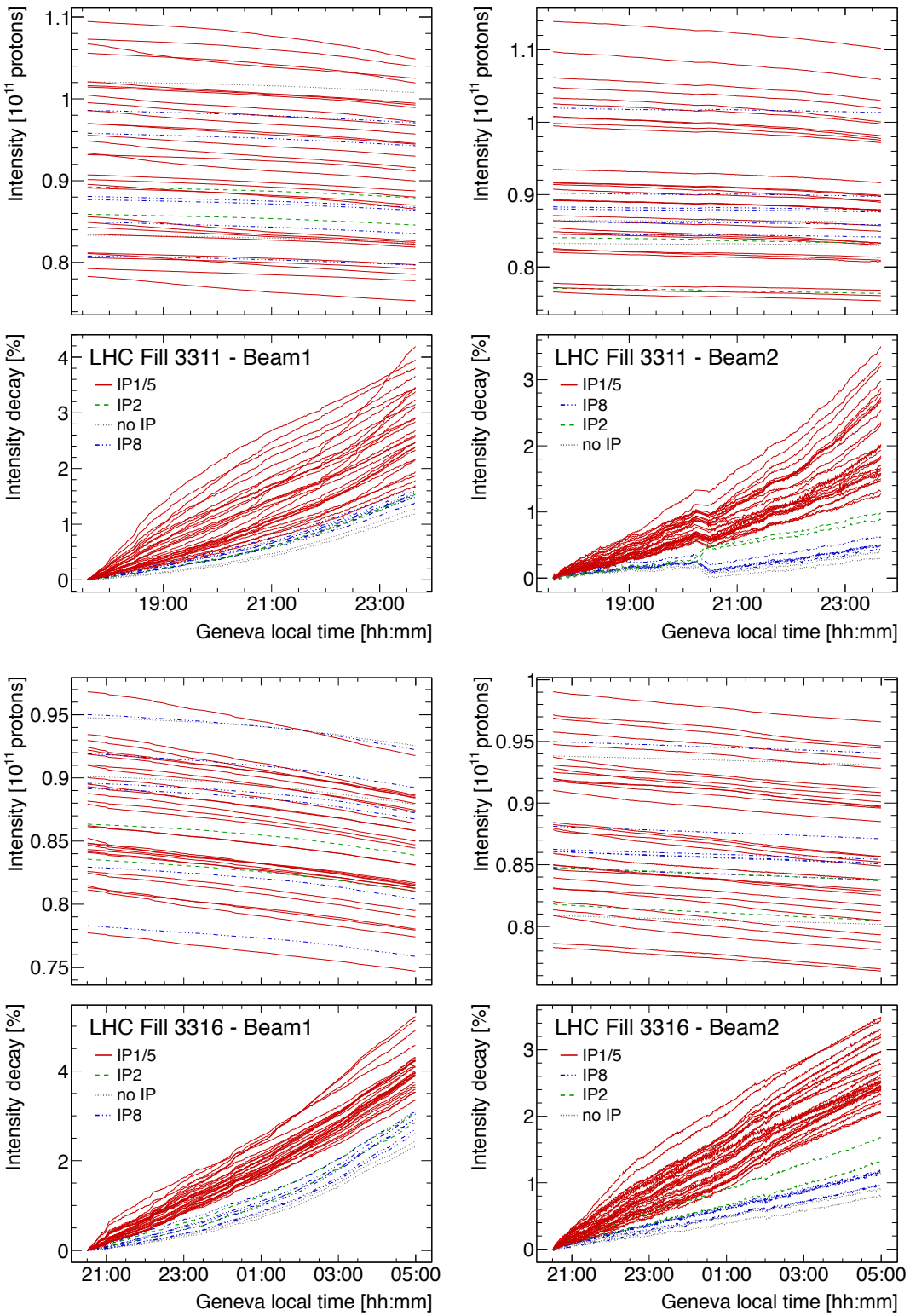

Figure 7.5.: Bunch-by-bunch currents during the LHC fills, in which the November VdM scans took place.

- **IP2** Group of bunches colliding only in IP2 (ALICE).
- **IP8** Group of bunches colliding only in IP8 (LHCb)
- **no IP** Group of non-colliding bunches.

At the beginning of the fills, the bunches contain about 0.7 up to $1.1 \cdot 10^{11}$ protons. There is no clear correlation of bunch current with category. However, even though the magnitude of decay differs from bunch to bunch, it is similar among bunches of the same category. While the non-colliding bunches have the lowest losses, the bunches of category IP1/5 have the highest ones; the bunches colliding in IP2 or IP8 lie in between.

A possible explanation may be, that the bunches of group IP1/5 collide twice and hence lose more protons due to luminosity production than non-colliding bunches or bunches colliding only once. Another reason may be, that bunches colliding in more than one IP are more effected by beam-beam effects, thus losing more protons due to instabilities. A feature visible for the bunches colliding in IP1/5 is, that high intensity bunches typically have larger relative losses than low intensity bunches.

One notices a major difference between the July and November scans: while the relative current losses are up to approximately 20 % in July, they are limited to about 5 % in November. A more subtle feature is contained within figure 7.5: during LHC fill 3311 at about 20:30h the measured beam 2 bunch currents abruptly jump. The cause was already discussed in the previous section and attributed to instrumental effects. While the currents at the time of the jump decrease for all bunches of category IP2, they increase for the rest of the bunches. Why the different bunch categories are affected in a different way is not understood.

In order to properly take the current decay during a VdM scan into account, the scan evaluation is slightly modified. According to equation (5.20), the visible cross section $\sigma_{vis}^{(i)}$ for colliding bunch pair i can be written as[4]:

$$\sigma_{vis}^{(i)} = \frac{2\pi\Sigma_x^{(i)}\Sigma_y^{(i)}}{n_1^{(i)}n_2^{(i)}} \frac{\mu_{vis}^{(i)}(0,\Delta y_0)\mu_{vis}^{(i)}(\Delta x_0,0)}{\mu_{vis}^{(i)}(\Delta x_0,\Delta y_0)} \tag{7.1}$$

where $n_1^{(i)}n_2^{(i)}$ is the bunch current product averaged over the duration of the scan. For the case of slowly decaying bunch currents, μ_{vis} should be replaced by the specific visible μ defined as

$$\mu_{vis,spec} = \frac{\mu_{vis}}{n_1 n_2} \tag{7.2}$$

[4]Here one uses the relation: $\mathcal{R}^{(i)} = \mu_{vis}^{(i)} f_r$.

and equation (7.1) becomes:

$$\sigma_{vis}^{(i)} = 2\pi\Sigma_x^{(i)}\Sigma_y^{(i)}\frac{\mu_{vis,spec}^{(i)}(0,\Delta y_0)\mu_{vis,spec}^{(i)}(\Delta x_0,0)}{\mu_{vis,spec}^{(i)}(\Delta x_0,\Delta y_0)} \tag{7.3}$$

Instead of using bunch currents averaged over the duration of the scan, each measured μ_{vis} is divided by the bunch current product measured at the time of the corresponding scan step. Accordingly, Σ_x and Σ_y are determined with scan curves based on $\mu_{vis,spec}$ rather than μ_{vis}.

Current correction factors

Since the VdM scans are evaluated on the basis of the uncorrected FBCT currents, the obtained σ_{vis} values must be corrected for three factors: the deviation of the summed FBCT bunch currents from the total DCCT currents, the amount of present ghost charges, and the amount of satellite bunches. The current correction procedure is discussed in detail in section 6.1. A given relative change of the bunch current product $n_1 n_2$ results in a relative change of σ_{vis} of same absolute value, but opposite sign.

The correction factors for the four VdM scan fills are listed in table 7.4. The FBCT scale correction was discussed before. Satellite bunches are measured with the LDM. Instead of treating each bunch individually, the satellite bunch correction is based on bunch-averaged satellite charges. In July, the bunch-averaged intensity of satellite bunches with respect to the main bunch is about 0.2 % to 0.3 % in both beams. It is less than 0.1 % in both beams in November. Thus the correction of σ_{vis} due to satellite bunches is about +0.5 % for the July scans and negligible for the November ones.

The relative amount of ghost charges is measured by LHCb via beam-gas interactions. In July, the ghost charge fraction lies between 0.2 % and 0.3 % per beam and the change of σ_{vis} is approximately +0.5 %. The ghost charge correction for the November scans is roughly half the July correction.

After combining the different correction factors, the overall σ_{vis} correction is on the order of +1 % for the July scans, and about +0.3 % for the November scans.

Orbit drifts

Figure 7.6 and 7.7 illustrate the orbit drifts during all centred VdM scans in July and November 2012. The orbit drifts during scans, in which the beams were separated in the non-scan plane, are not discussed here. The shown data corresponds to the time between the first scan step of the x scan and the last scan step of the y scan.

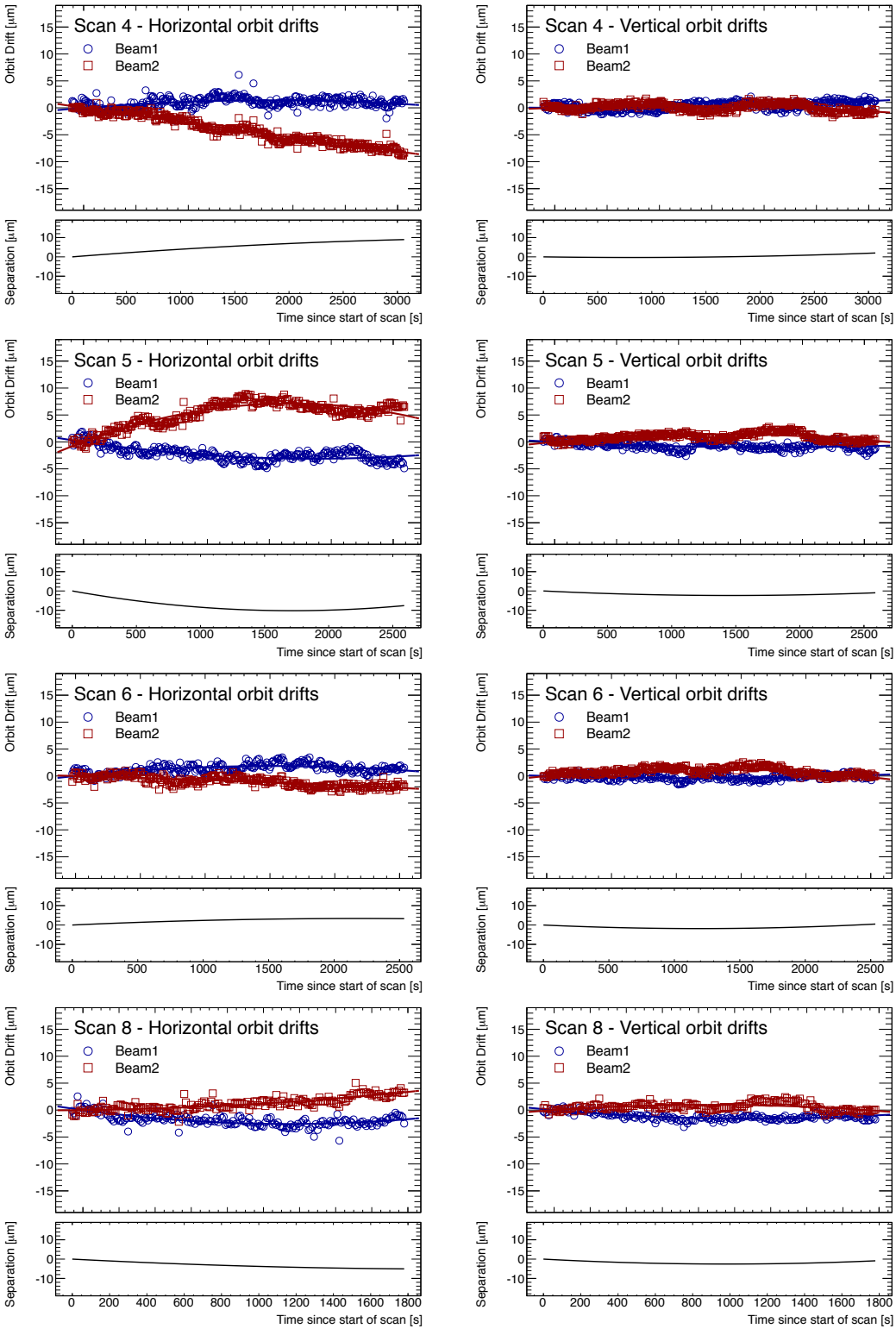

Figure 7.6.: Horizontal and vertical orbit drifts at IP1 (ATLAS) during the four centred VdM scans in July 2012.

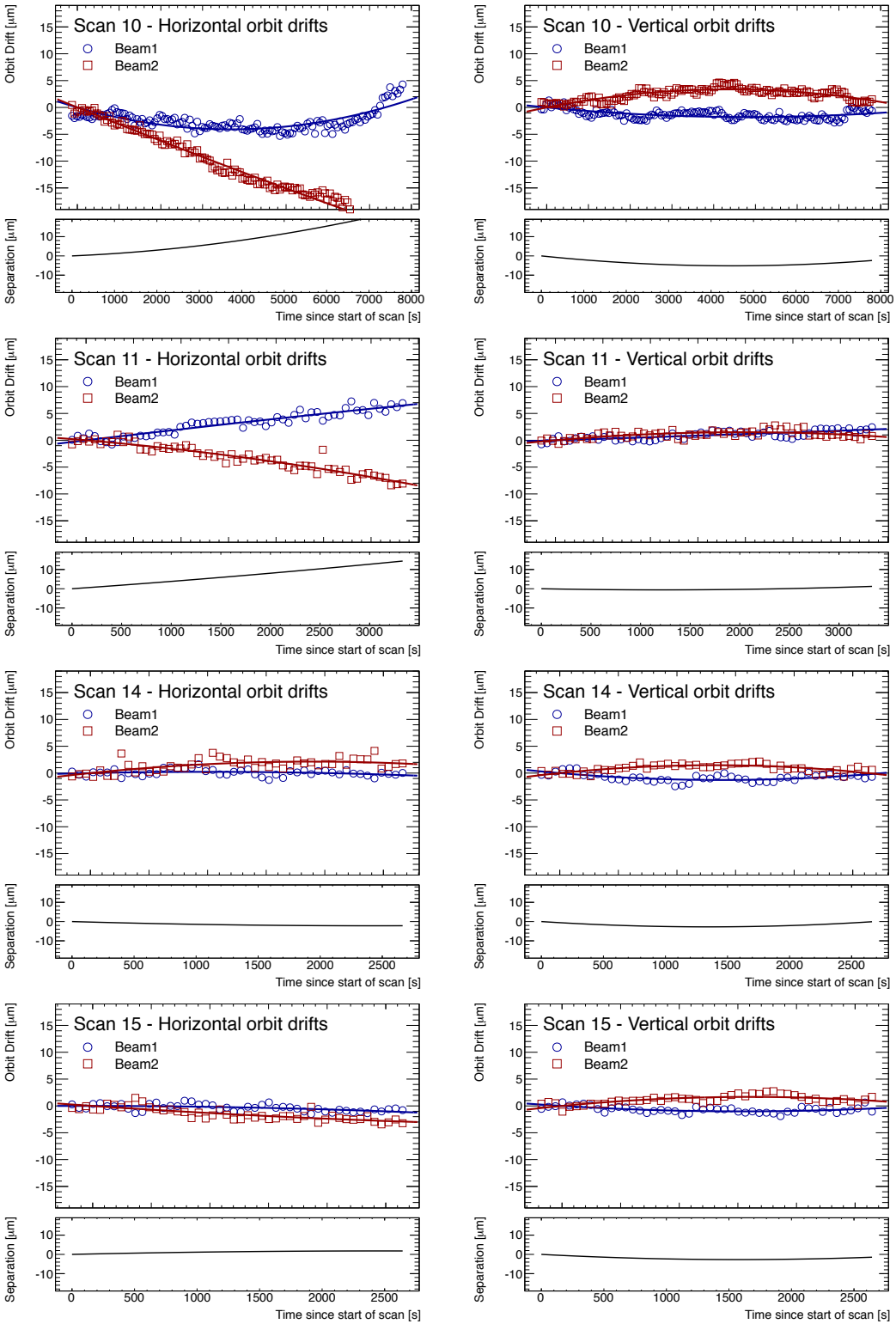

Figure 7.7.: Horizontal and vertical orbit drifts at IP1 (ATLAS) during the four centred VdM scans in November 2012.

	July 2012 corrections				November 2012 corrections			
	Fill	n_1 [%]	n_2 [%]	σ_{vis} [%]	Fill	n_1 [%]	n_2 [%]	σ_{vis} [%]
FBCT scale	2855	+0.02	+0.05	−0.07	3311	<0.03	<0.15	negligible
	2856	−0.11	−0.20	+0.30	3316	<0.05	<0.03	negligible
Satellites	2855	−0.21	−0.27	+0.49	3311	<0.07	<0.04	negligible
	2856	−0.20	−0.34	+0.54	3316	<0.02	<0.02	negligible
Ghost charge	2855	−0.25	−0.24	+0.49	3311	−0.158	−0.060	+0.22
	2856	−0.27	−0.22	+0.49	3316	−0.215	−0.060	+0.28
Total	2855			+0.91	3311			+0.22
	2856			+1.33	3316			+0.28

Table 7.4.: Corrections to the FBCT based current measurements and to σ_{vis}. The correction factors are given for all four fills with injection optics, during which VdM scans were performed.

Each row of plots corresponds to one scan. The left plots refer to the horizontal orbit drifts and the right ones to the vertical ones. All plots comprise two panels. The upper ones show the orbit drifts of beam 1 and beam 2, the lower ones depict the beam separation caused by the orbit drifts. This separation must not be confused with the separation of the beams at the interaction point due to the local orbit bumps, rather it must be treated as an additional separation. The methodology is discussed in section 6.2.

The shown orbit drifts are based on the average of the two independently obtained orbits from BPMs on either side of the IP. After fitting the orbit drifts with a quadratic polynomial they are shifted by a constant, such that at the beginning of the scans the drifts are zero. The separation plotted in the lower panel is based on the fitted orbit drifts. The reason for fitting the data is the large noise of the orbit measurements. Furthermore, the fluctuations in the time scale of a few hundred seconds are presumably caused by instrumental effects: while the general trend of the orbit drifts is consistent between the independently obtained orbits, the fast fluctuations are not.

The data points in the July and November plots have a different granularity in time. In July, the data points are spaced by 10 s intervals. In November, they are spaced by 100 s intervals. The reduction of data points was motivated by the goal to reduce necessary computing resources for the orbit fits. For easier comparisons between scans, the y axis scale is identical for all plots.

During the July scans, the vertical orbits typically drift by up to about 3 μm over the full scan duration. The horizontal drifts are more sizeable and most pronounced in scan 4 and 5, in which they are as big as 10 μm. The quantitative impact of the orbit drifts on the calibration constants σ_{vis} is presented later in this thesis for all scans.

Similar to the July scans, the vertical orbit drifts in November are about 4 μm over

the full scan duration. The horizontal drifts are small in scan 14 and 15, but significant in scan 10 and 11. Because of data acquisition problems, scan 10 did last twice as long as the other scans and the additional beam separation due to orbit drifts is approximately $30\,\mu$m. The origin of the drifts is unknown, whether tidal effects play a role is under study.

Scan curve models

Different scan curve models and corresponding fit functions are discussed in section 5.2. The choice of the primary scan curve model is based on the ability of a model to describe the measured scan curves. The latter criterion is evaluated through the fit quality, thus via the χ^2/ndf of the fits[5].

Before applying the fit functions to measured scan curves, a few additional parameters are introduced:

- p_0^x/p_0^y: These parameters account for a constant background of the measured μ_{vis} values. The background is assumed to be independent of the separation and corresponds to a constant term which is added to the scan curve fit function. p_0^x denotes the constant background during the x scan and p_0^y is the one during the y scan. A constant background component may either be caused by constant instrumental noise of the luminosity detectors or may be beam induced.

- μ_x/μ_y: These parameters are added to the nominal separation and account for a global shift of the nominal separation scale. Possible causes for the shifts are discussed in section 6.2. μ_x denotes a shift of the horizontal nominal separation scale and μ_y a shift of the vertical one. μ_x and μ_y must not be confused with the mean number of interactions per BC, labelled μ, or the mean visible number of interactions per BC, labelled μ_{vis}.

The inclusion of the above parameters into the fit functions of section 5.2 is straightforward and exemplarily presented for the common Gaussian model. Writing equation (5.23) in terms of μ_{vis} rather than $\mathcal{R}$, and adding the parameters μ_x and p_0^x, one finds:

$$\mu_{vis}(\Delta x) = \frac{A}{\sqrt{2\pi}\sigma}\exp\left(-\frac{(\Delta x - \mu_x)^2}{2\sigma^2}\right) + p_0^x \tag{7.4}$$

[5] *number of degrees of freedom*

Since the constant background component is considered to not originate from proton-proton interactions, it is not treated as real luminosity and the definitions of Σ_x and Σ_y given in section 5.2 remain unchanged.

While the July scan curves are described best by Double Gaussians, in November it is sufficient to use common Gaussians. In order to estimate the uncertainties related to the choice of the model, the November scans were also analysed based on the Super Gaussian model.

Length scale calibration and correction

Section 6.2 contains a description on how the beams are separated at the IP via closed orbit bumps. The bump is created by two pairs of steering dipoles and its amplitude is controlled via the magnet settings. The nominal separation denotes the scale linked with the magnet settings. The only LHC instrumentation available for calibrating the separation corresponding to a bump amplitude, is one BPM on either side of the IP; both contained in between the steering dipoles. Even though calibrating the separation scale, also referred to as length scale, based on the two BPMs is a simple task, the achievable precision suffers from various effects impacting the stability of the BPM readings. A more precise and stable procedure utilises the primary vertex reconstruction capabilities of the ATLAS inner detector.

Both beams can be displaced horizontally and vertically, hence there are four bump amplitudes. Because all bump amplitudes are subject to different lattice and magnet functions, they must be calibrated independently [17]. In order to calibrate a given bump amplitude, the corresponding beam is displaced stepwise. For each displacement the beam undergoes a mini luminosity scan by the other beam. The mini scan is used to determine the nominal separation of maximum beam overlap. Additionally, the position of the luminous centroid is reconstructed for each mini scan step, hence one can derive the centroid position for maximum beam overlap. The transverse position of the luminous centroid at maximum beam overlap is identical to the transverse position of the beam, whose bump amplitude is being calibrated. In this manner, the transverse beam position is determined for different orbit bump amplitudes. To extract the length scale factor, which relates the bump amplitude to separation, the dependency of the beam position on the bump amplitude is fitted by a linear polynomial.

A length scale calibration with injection optics was conducted in July at the end of LHC fill 2885. During the same fill, also four of the ATLAS VdM scans took place. Because the beams were lost before the end of the calibration, the procedure was completed at the start of fill 2856.

Scan	Plane	Separation in non-scan plane [μm]	Start [hh:mm]	Stop [hh:mm]	In-plane re-centering after scan [μm]
4	x	0	9:14	9:31	0
	y		9:45	10:02	0
5	x	0	11:54	12:11	+13
	y		12:20	12:37	0
6	x	0	12:43	13:00	0
	y		13:05	13:22	0
7	x	344	13:52	14:09	0
	y		14:18	14:35	0
8	x	0	21:41	21:53	0
	y		21:58	22:11	0
9	x	369	22:18	22:31	0
	y		22:38	22:50	0

Table 7.5.: Overview of the July 2012 VdM scans. The scan times are given in Geneva local time. All scans took place on July 19, 2012. The horizontal line in between scan 7 and 8 alludes to the fact, that the scans took place in different LHC fills.

In order to calibrate each of the four bump amplitudes, the corresponding beam was displaced in five steps over the nominal separation range $\pm 240\,\mu$m. A mini scan for a given displacement comprised three scan steps spanning the nominal separation range $\pm 100\,\mu$m. After combining the measured length scales for both beams, one finds, that the nominal separation scale overestimates the separation by 0.33 % in the horizontal plane and 0.44 % in the vertical plane. Therefore the product $\Sigma_x \Sigma_y$ decreases by 0.77 % when changing from nominal separation to the more precise inner detector based separation, hence σ_{vis} decreases by 0.77 %.

From past experience at the LHC, the length scale reproducibility for identical beam optics configurations is believed to be very high, hence there was no additional length scale calibration in November.

7.2. July Van der Meer scans

The six July VdM scans took place in two different fills. Four scans were carried out in LHC fill 2855 and two in fill 2856. While the scans in fill 2855 comprise 25 scan steps in each plane, the scans in fill 2856 are based on 17 scan steps. The scans in the second fill were intended as a quick cross-check of the results obtained from the first fill, hence the reduction of scan steps. The transverse beam separation in the horizontal and vertical plane spanned the range $\pm 6\sigma_b$.

The start and end times of all July scans are shown in table 7.5. Also listed is the separation in the non-scan plane. Scan 4, 5, 6 and 8 are centred scans, while scan 7 and 9 are offset ones. An x or y scan lasted about fifteen minutes, the duration of a full scan was typically forty-five minutes. During the time between scan 4 and 5, two VdM scans were carried out in Point 5 for the CMS experiment.

The last column of table 7.5 shows the re-centering of the beams immediately after the x or y scan, a re-centering was only performed once after the x scan of scan 5.

Scan curve examples

Figure 7.8 shows examples of typical horizontal scan curves during the July VdM scans obtained with the luminosity algorithms BCMV_EventOR and LUCID_EventOR. Also shown are the fits to the scan curves. The primary fit model for the centred scans is a Double Gaussian plus constant background, since common Gaussian fits are not able to describe the wide tails. The fit residuals, normalised to the statistical error of the data, indicate that the model describes the data appropriately.

The peak rates measured by BCMV_EventOR and LUCID_EventOR differ from each other by about one order of magnitude, which is a consequence of the higher event detection efficiency of LUCID compared to BCM. Although not shown here, the peak rates measured by BMCH_EventOR are similar to the ones of BCMV_EventOR, as expected.

The lower plot depicts also an example of a scan curve obtained in offset scan 7, during which the beams were separated in the non-scan plane. Hence the lower peak rates compared to scan 6, which is a centred scan. In contrast to the centred scan curves, the offset scan curves are well described by common Gaussians.

Because of the low rates, the BCM algorithms are unsuitable for evaluating the offset scans, and the curve fitting becomes unstable.

Goodness of fit

The fit quality is judged by the reduced χ^2, defined as χ^2/ndf, where ndf denotes the number of degrees of freedom. The latter corresponds to the number of fitted data points minus the number of fit parameters. Figure 7.9 illustrates the reduced χ^2 of all horizontal and vertical scan curve fits for the four centred July VdM scans. The average χ^2/ndf is close to 1.0, which justifies the choice of the Double Gaussian fit model. Even if demonstrated here for BCMV_EventOR only, the fits to scan curves obtained with the other two algorithms are good as well.

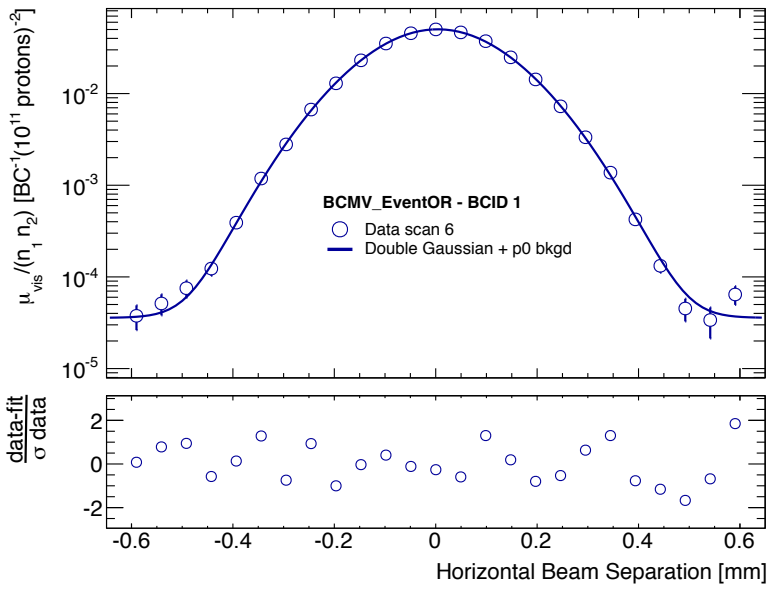

(a) Horizontal scan curve of BCID 1 in scan 6 measured by BCMV_EventOR.

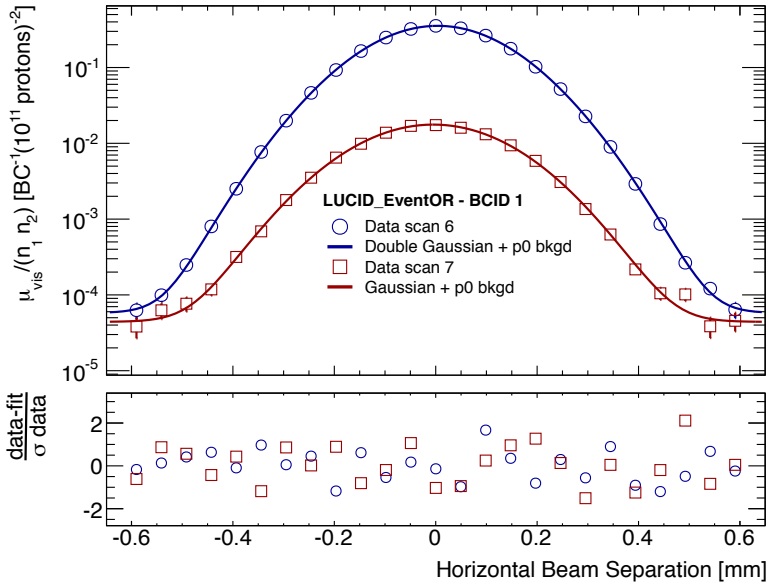

(b) Horizontal scan curves of BCID 1 in scan 6 and 7 measured by LUCID_EventOR.

Figure 7.8.: Examples for horizontal scan curves during the July VdM scans. The upper panels show the measured $\mu_{vis,spec}$ for different horizontal beam separations. The solid lines represent fits to the data. The lower panels show the difference between data and fit, normalised to the statistical error of the data.

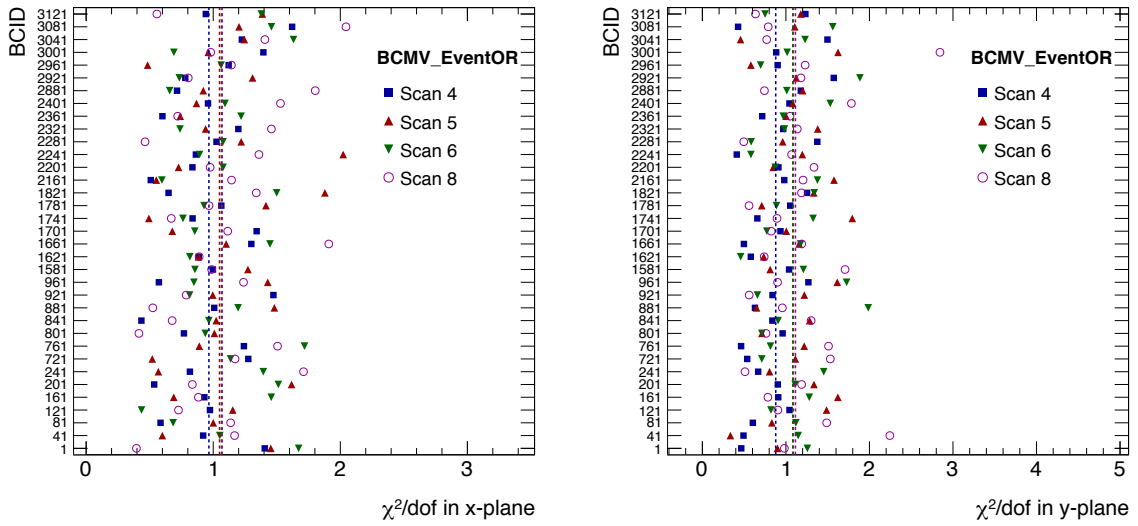

(a) Horizontal scans **(b)** Vertical scans

Figure 7.9.: χ^2/dof for the Double Gaussian plus constant background fits to the individual bunch scan curves for the four centred July 2012 scans. The vertical dashed lines indicate the bunch-averaged χ^2/dof per scan.

Convolved bunch sizes Σ_x and Σ_y

The horizontal and vertical convolved bunch sizes Σ_x and Σ_y, determined with the luminosity algorithm BCMV_EventOR, are shown in figure 7.10 for the four centred July VdM scans. Σ_x and Σ_y are defined in equation (5.17) and correspond to the widths of the scan curves in the horizontal and vertical plane, respectively.

The bunch-averaged Σ_x per scan lies between 120 and 124 μm. The increase of Σ_x between scan 4 and 6 is caused by emittance growth over time. Scan 8 was performed in a different fill and the bunches are different from those in scan 4, 5 and 6. Assuming the bunches in beam 1 and beam 2 have similar transverse sizes, one can deduce a few properties for the individual bunches: the average Σ_x is approximately 122 μm, hence the average bunch size along the x axis is $1/\sqrt{2} \cdot 122\,\mu\text{m} = 86\,\mu\text{m}$; the increase of Σ_x by 3.5 % between scan 4 and 6 corresponds to an average emittance growth of about 2.5 % per bunch.

The bunch-averaged Σ_y per scan lies between 126 and 128 μm. The increase between scan 4 and 6 is approximately 1.5 %. The relative spread of the convolved bunch sizes in both planes is about ± 5 % with respect to the bunch-averaged value. Bunches having a large (small) Σ_x typically also have a large (small) Σ_y and vice versa.

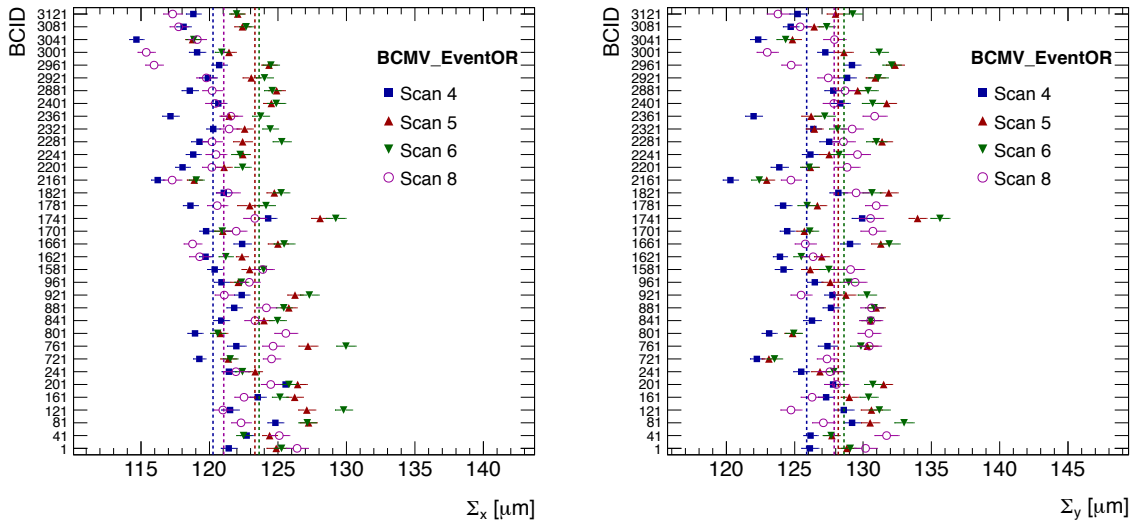

(a) Horizontal scans **(b)** Vertical scans

Figure 7.10.: Convolved bunch size Σ_x (Σ_y) obtained from the horizontal (vertical) scans in the four centred July 2012 scans. The vertical dashed lines indicate the bunch-averaged Σ_x (Σ_y) per scan. The errors are statistical only.

Separation at maximum beam overlap: μ_x and μ_y

Figure 7.11 illustrates the orbit drift corrected nominal beam separations μ_x and μ_y, at which the beams have maximum overlap in the horizontal and vertical plane, respectively. The depicted separations are obtained with BCMV_EventOR and correspond to the four centred July VdM scans.

Within a scan, μ_x and μ_y are consistent among different bunches. This accords with the expectations, since all bunches follow the same orbit trajectory[6]. The changes of μ_x and μ_y between scans are due to orbit drifts. Here one should keep in mind, that the orbit drift correction only corrects for drifts within a scan as explained in section 6.2.

In the vertical plane, the orbit drifts imply a change of μ_y by at most 5 μm between scan 4, 5 and 6. The good reproducibility of μ_y in scan 5 and 6 suggests stable vertical orbits at this time. μ_x jumps back and forth in scan 4, 5 and 6. This can be understood from the horizontal re-centering of the beams immediately after the x scan of scan 5, which also explains, why μ_x in scan 6 is closer to zero than in scan 5. Taking the re-centering correction into account, one deduces that the horizontal orbit drifts are larger than the vertical ones. This is in line with the orbit monitoring observations presented in section 7.1.

[6]This is only the case for filling schemes without long range interactions, like employed during the July and November VdM scans.

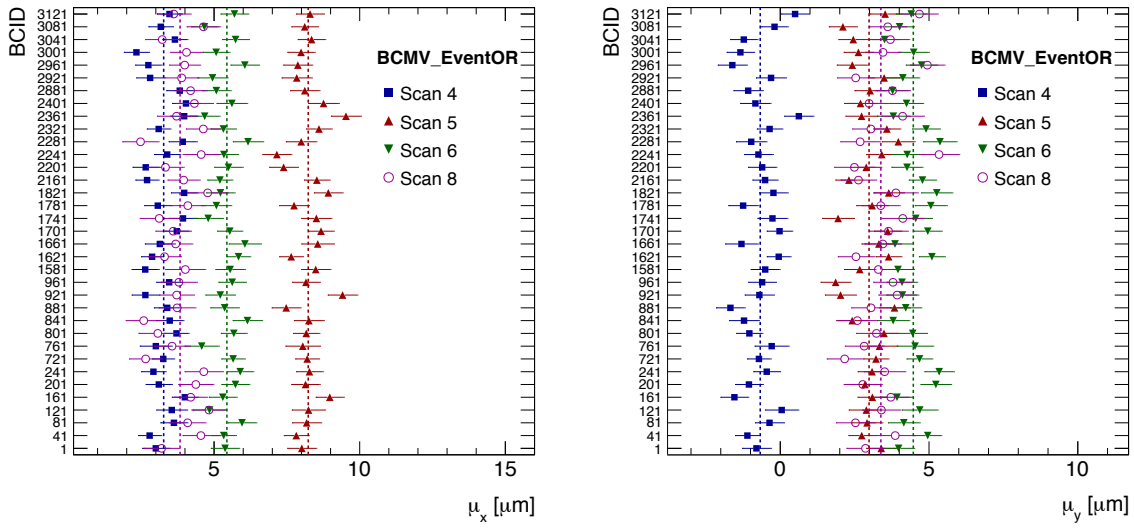

(a) Horizontal scans **(b)** Vertical scans

Figure 7.11.: Orbit drift corrected nominal separation μ_x (μ_y) for maximum beam overlap, obtained from the horizontal (vertical) scans in the four centred July 2012 scans. The vertical dashed lines indicate the bunch-averaged μ_x (μ_y) per scan. The errors are statistical only.

Evolution of $\mu^{max}_{vis,spec}$ in time

The evolution of the scan curve peaks $\mu^{max}_{vis,spec}$ during the scans 4, 5 and 6 is depicted in figure 7.12. The shown $\mu^{max}_{vis,spec}$ values correspond to BCMV_EventOR. Since each colliding bunch pair may have a different luminosity, hence a different $\mu^{max}_{vis,spec}$, the first five paired BCIDs are shown.

The downward trend of μ^{max}_{spec} with time is likely due to emittance growth. It is not caused by a decay of the bunch currents, since $\mu^{max}_{vis,spec}$ is defined as $\mu^{max}_{vis}/(n_1 n_2)$ and therefore corrected for the current decay. In general, the variation of $\mu^{max}_{vis,spec}$ between scans may also be due to imperfectly centred beams in the non-scan plane. An interesting feature in figure 7.12 is, that the average $\mu^{max}_{vis,spec}$ is larger in y scan 5 and x scan 6 than in x scan 5. This can be explained by the horizontal beam re-centering which was done in between x scan 5 and y scan 5.

Calibration constants σ_{vis}

Figure 7.13a illustrates the per-bunch visible cross sections for BCMV_EventOR determined in the four centred July VdM scans. The shown values are bunch current and length scale corrected, the correction factors can be looked up in section 7.1.

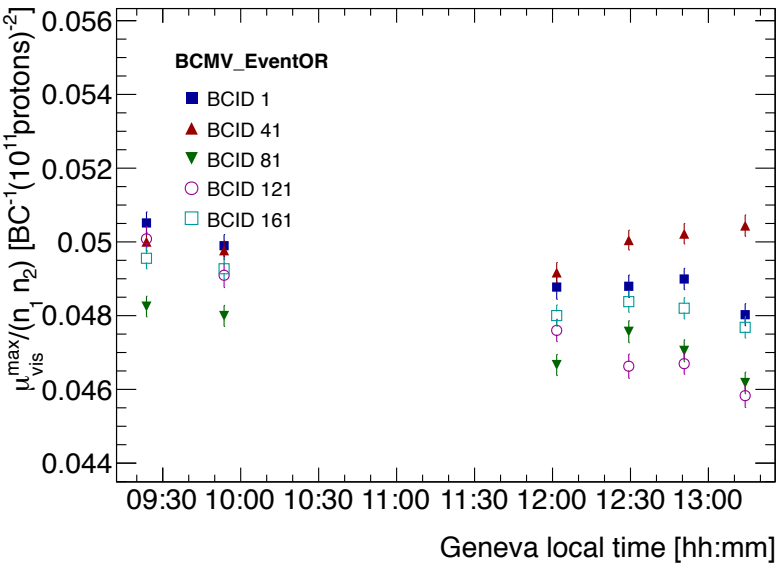

Figure 7.12.: Evolution of $\mu_{vis,spec}^{max}$ in time during LHC fill 2855 for the first five paired BCIDs. The plotted data points (from left to right) correspond to x scan 4, y scan 4, x scan 5, y scan 5, x scan 6 and y scan 6. The errors are statistical only.

Even though the visible cross section σ_{vis} is supposed to be a detector specific constant, the bunch-averaged σ_{vis} significantly vary among the scans. The variation is more clearly seen in figure 7.13b which depicts the evolution of the bunch-averaged σ_{vis} over time. The σ_{vis} values in scan 5 and 6 are similar, but deviate from scan 4 by approximately 2 %. Since the length scale and bunch current uncertainties are highly correlated between scans in the same fill, they are unlikely responsible for the variation. Furthermore, the bunch-averaged σ_{vis} in scan 4 is similar to the one in scan 8.

Table 7.6 gives an overview of the bunch-averaged σ_{vis} per scan and luminosity algorithm. The σ_{vis} values for both BCM algorithms are similar, but much smaller than the LUCID ones. Since the pattern and magnitude of the variation is consistent between the algorithms BCMV_EventOR, BCMH_EventOR and LUCID_EventOR, the variation does not originate from possible instabilities or non-linearities of the detector response.

The relative RMS of the per-bunch visible cross sections measured by LUCID in a scan is half as large as the RMS for BCM, even though the χ^2/ndf of the average is less good. Here, the number of degrees of freedom is given by the number of paired bunches minus one. The reason is, that LUCID is more sensitive to systematic error sources because of its high statistics. The systematic uncertainties affecting the σ_{vis} calibration are discussed in detail in section 7.4.

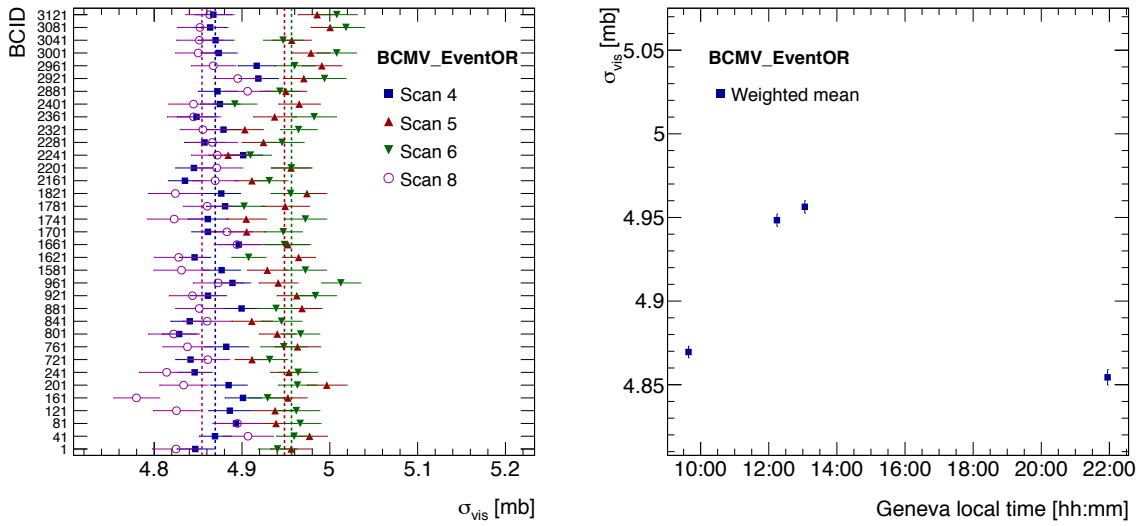

(a) Per-bunch σ_{vis}. The vertical dashed lines indicate the bunch-averaged σ_{vis} per scan.

(b) Bunch-averaged σ_{vis} plotted against the time of the scan.

Figure 7.13.: σ_{vis} obtained with BCMV_EventOR in the the four centred July 2012 scans. The plotted data points (from left to right) in (b) correspond to scan 4, 5, 6 and 8. The errors are statistical only. Length scale and bunch current corrections are applied.

BCMV_EventOR				
Scan	$\overline{\sigma_{vis}}$ [mb]	χ^2/dof	RMS	Rel. RMS [%]
4	4.870 ± 0.0035	1.2	0.023	0.46
5	4.948 ± 0.0038	1.7	0.028	0.57
6	4.956 ± 0.0038	1.8	0.030	0.60
8	4.854 ± 0.0047	1.0	0.028	0.57
BCMH_EventOR				
Scan	$\overline{\sigma_{vis}}$ [mb]	χ^2/dof	RMS	Rel. RMS [%]
4	4.843 ± 0.0035	1.8	0.029	0.59
5	4.932 ± 0.0037	1.5	0.027	0.55
6	4.939 ± 0.0038	1.2	0.025	0.51
8	4.837 ± 0.0047	0.9	0.026	0.55
LUCID_EventOR				
Scan	$\overline{\sigma_{vis}}$ [mb]	χ^2/dof	RMS	Rel. RMS [%]
4	34.414 ± 0.0098	4.4	0.119	0.35
5	35.000 ± 0.0103	3.0	0.105	0.30
6	35.069 ± 0.0103	3.4	0.110	0.31
8	34.347 ± 0.0128	1.4	0.089	0.26

Table 7.6.: Error-weighted average of the per-bunch σ_{vis} obtained in the four centred July 2012 scans. The errors are statistical only. Length scale and bunch current corrections are applied.

Scan	Plane	Separation in non-scan plane [μm]	Start [hh:mm]	Stop [hh:mm]	In-plane re-centering after scan [μm]
10	x	0	17:49	18:08	-9.6
	y		19:39	19:57	-13
11	x	0	20:04	20:21	-26
	y		20:39	20:57	0
12	x	344	21:05	21:23	-16
	y		21:34	21:52	0
13	x	197	22:00	22:18	0
	y		22:28	22:46	0
14	x	0	22:53	23:11	0
	y		23:16	23:34	0
15	x	0	1:11	1:29	0
	y		1:34	1:52	0

Table 7.7.: Overview of the November 2012 VdM scans. The scan times are given in Geneva local time. Scans 10-14 were carried out on November 22, 2012, scan 15 on November 24, 2013. The horizontal line in between scan 14 and 15 alludes to the fact, that the scans took place in different LHC fills.

7.3. November Van der Meer scans

In November 2012, ATLAS performed in total six VdM scans which took place in two different fills. Five scans were carried out directly one after another in LHC fill 3311 and another scan took place in LHC fill 3316. All scans comprised 25 scan steps in each plane. The transverse beam separation in the horizontal and vertical plane spanned the range $\pm 6\sigma_b$. Table 7.7 lists the start and end times of all November scans. The third column of the table shows the separation in the non-scan plane. Scans 10, 11, 14 and 15 are centred scans, while scans 12 and 13 are offset ones.

A major difference with respect to the July scans is, that the amount of separation in the non-scan plane was different for both offset scans: while it was $344\,\mu$m for scan 12, it was $197\,\mu$m for scan 13. This modification of the scan sequence was motivated by the outcome of the July VdM scans and aims at a better understanding of possible non-factorisation of the transverse density profiles of the colliding bunches into independent x and y components. The findings of the offset scans are presented in section 7.4.

As in July, an x or y scan lasted about fifteen minutes and the overall duration of a scan was typically forty-five minutes. One notable exception is scan 10 which lasted about two hours, the reason being a data acquisition problem which required restarts of various systems needed for the VdM scans. The last column of table 7.7 lists the re-centering of the beams immediately following the x or y scan. A beam re-centering

in both separation planes was considered necessary in scan 10 and a re-centering only in the horizontal plane was done in scans 11 and 12.

Scan curve examples

Figure 7.14 illustrates typical horizontal scan curves during the November VdM scans. The curves are obtained with the algorithms BCMV_EventOR and LUCID_EventOR. Also shown are fits to the scan curve data. The primary fit function for the November scans is a common Gaussian plus constant background. Double Gaussian fits proved to be unstable and often reduced to the common Gaussian case. The fit residuals, normalised to the statistical error of the data, confirm, that the model is able to describe the measured event rates even for high beam separation.

The lower plot in figure 7.14 depicts examples for scan curves obtained during both offset scans. The offset scans are evaluated based on LUCID_EventOR because of its high event detection efficiency. The offset scan curves are well described by common Gaussians. The peak rates decrease with increased beam separation in the non-scan plane, as expected.

Goodness of fit

The quality of scan curve fits is illustrated in figure 7.15 for the four centred November VdM scans. The left plot shows the χ^2/ndf for all horizontal scan curve fits, the right plot for all vertical ones. The depicted data corresponds to BCMV_EventOR.

The average χ^2/ndf is close to 2.0, indicating that the scan curve shapes slightly deviate from a perfect Gaussian distribution. For LUCID_EventOR, the bunch and scan-averaged χ^2/ndf is close to 4.0 in the horizontal plane and close to 2.0 in the vertical plane. Due to the higher statistics of the LUCID measurements compared to the ones of BCM, LUCID is more sensitive to non-Gaussian scan curve components. The quality of fits to scan curves obtained with BCMH_EventOR is similar to BCMV_EventOR.

Convolved bunch sizes Σ_x and Σ_y

Figure 7.16 shows the horizontal and vertical convolved bunch sizes Σ_x and Σ_y, determined with the luminosity algorithm BCMV_EventOR, for the four centred November VdM scans.

The bunch-averaged Σ_x per scan lies between 122 and 136 μm. The increase of Σ_x between scan 10 and 14 can be explained by emittance growth over time; scan 15 took

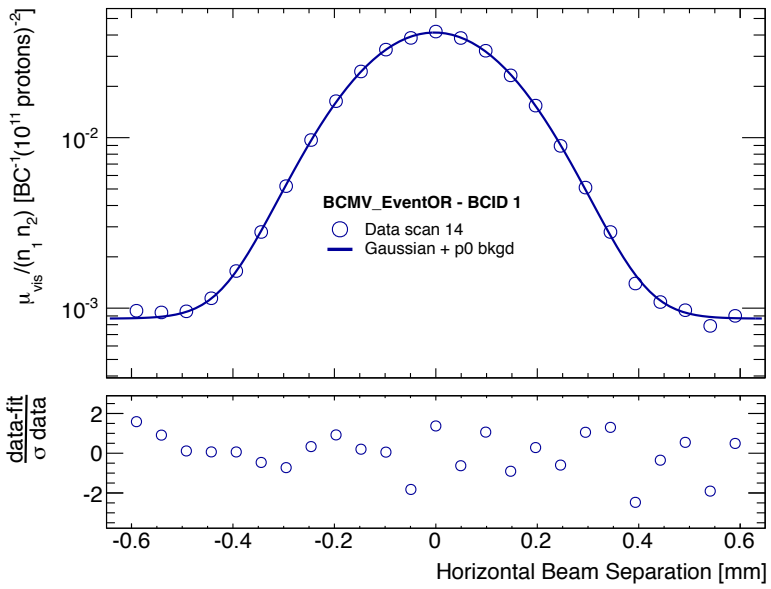

(a) Horizontal scan curve of BCID 1 in scan 14 measured by BCMV_EventOR.

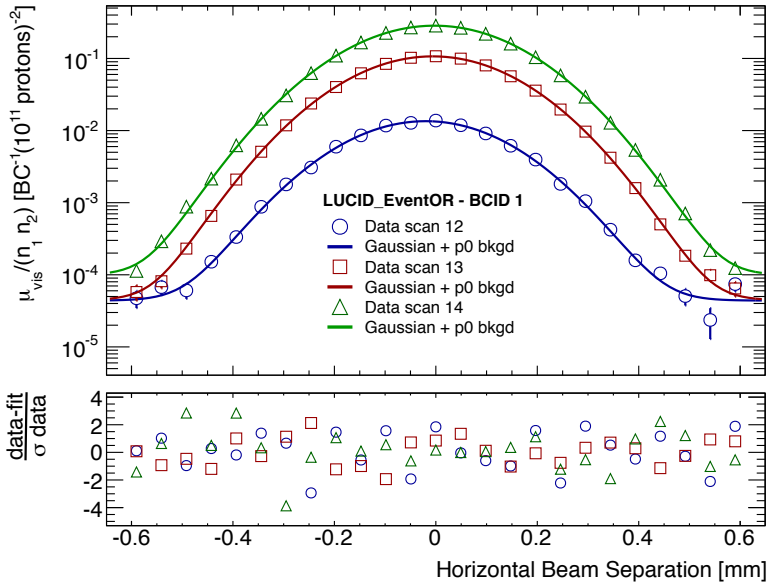

(b) Horizontal scan curves of BCID 1 in scan 12, 13 and 14 measured by LUCID_EventOR.

Figure 7.14.: Examples for horizontal scan curves during the November VdM scans. The upper panels show the measured $\mu_{vis,spec}$ for different horizontal beam separations. The solid lines represent fits to the data. The lower panels show the difference between data and fit, normalised to the statistical error of the data.

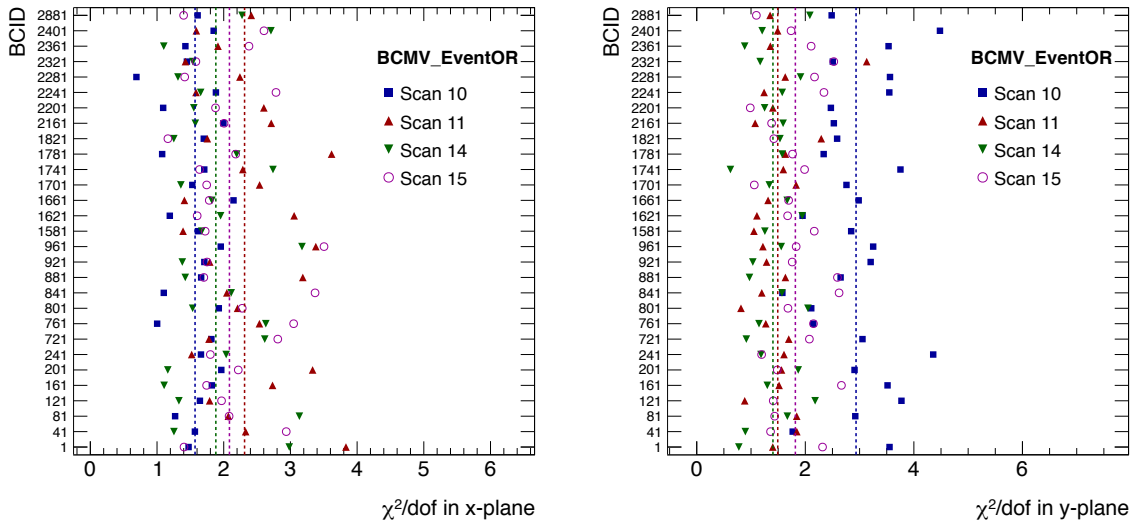

(a) Horizontal scans **(b)** Vertical scans

Figure 7.15.: χ^2/dof of the common Gaussian plus constant background fits to the individual bunch scan curves for the four centred November 2012 scans. The vertical dashed lines indicate the bunch-averaged χ^2/dof per scan.

place in a different fill. As done for the July VdM scans, one can deduce a few properties for the individual bunches, if one assumes that the bunches in beam 1 and beam 2 have similar transverse sizes: the overall average of Σ_x is approximately 130 μm, thus the bunch size along the x axis is on average 92 μm; the increase of Σ_x by 10 % between scan 10 and 14 corresponds to an average emittance growth of about 7 % per bunch.

The bunch-averaged Σ_y per scan lies between 130 and 136 μm. The increase between scan 10 and 14 is approximately 4 %. The relative spread of the convolved bunch sizes in both planes is about ± 5 % with respect to the bunch-averaged value. As for the July scans, one observes a clear correlation between the transverse bunch sizes in the horizontal and vertical plane. The emittance growth in the x plane is roughly 1.5 times larger than in the y plane. In July, this ratio is similar.

Separation at maximum beam overlap: μ_x and μ_y

Figure 7.17 depicts the orbit drift corrected nominal beam separations μ_x and μ_y, at which the beams have maximum overlap in the horizontal and vertical plane, respectively. The shown data corresponds to the four centred November VdM scans and is based on BCMV_EventOR. As stated before, the overall shifts of μ_x and μ_y between scans are caused by orbit drifts, since the orbit drift correction only corrects for drifts

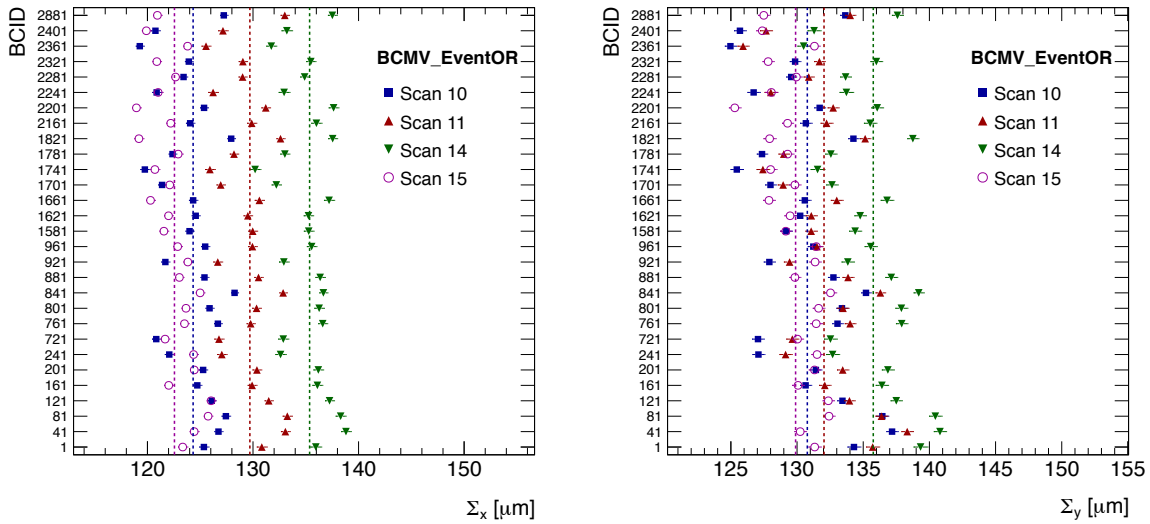

(a) Horizontal scans **(b)** Vertical scans

Figure 7.16.: Convolved bunch size Σ_x (Σ_y) obtained from the horizontal (vertical) scans in the four centred November 2012 scans. The vertical dashed lines indicate the bunch-averaged Σ_x (Σ_y) per scan. The errors are statistical only and correspond approximately to the marker size.

within a scan and not in between different scans.

The horizontal orbit drifts are clearly visible in scan 10 and 11. The scan curve peak in x scan 10 is found at a separation of approximately $-10\,\mu$m and even though the beams were re-centred after x scan 10, the position of the scan curve peak μ_x in x scan 11 differs from zero by about $-25\,\mu$m. Again, the separation is corrected for by a horizontal re-centering of the beams. In scan 14 and 15, μ_x is close to zero, indicating small orbit drifts. The large orbit drifts in the x plane at the time of scan 10 and 11 are in agreement with the findings of the orbit drift monitoring presented in section 7.1.

Vertical orbit drifts cause a μ_y of about $-16\,\mu$m in scan 10. After re-centering the beams in the vertical plane immediately after y scan 10, the separation corresponding to maximum beam overlap stays close to zero in scan 11 and 14 without any further corrections. Hence the impact of vertical orbit drifts on these VdM scans is marginal.

Evolution of $\mu^{max}_{vis,spec}$ in time

The evolution of the scan curve peaks $\mu^{max}_{vis,spec}$ during scans 10, 11 and 14 is depicted in figure 7.18. The shown values correspond to the first five paired BCIDs and are obtained via BCMV_EventOR. The downward trend of μ^{max}_{spec} with time can be explained by emittance growth. One striking feature is the increase of μ^{max}_{spec} between y scan 10

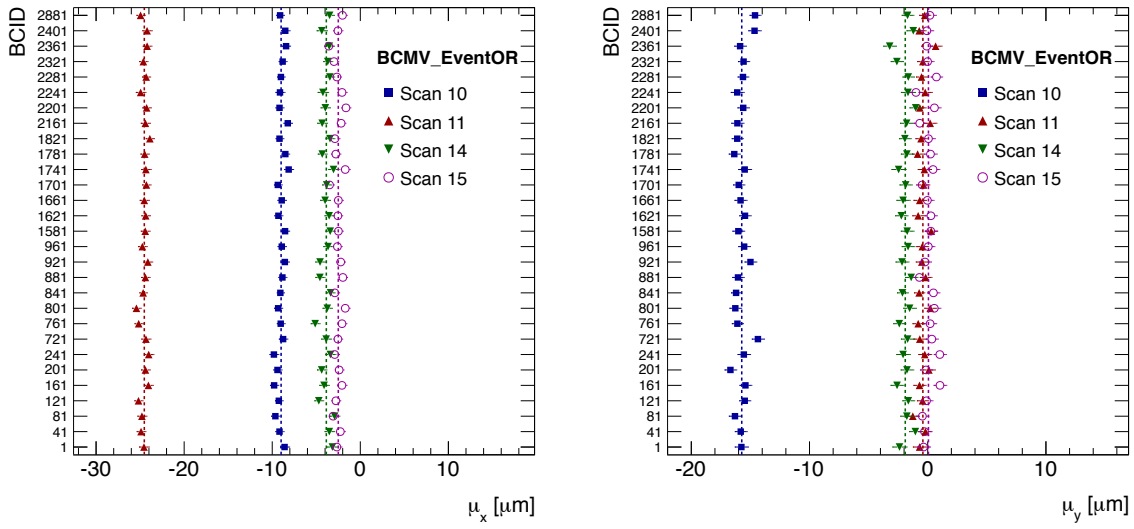

(a) Horizontal scans **(b)** Vertical scans

Figure 7.17.: Orbit drift corrected nominal separation μ_x (μ_y) for maximum beam overlap, obtained from the horizontal (vertical) scans in the four centred November 2012 scans. The vertical dashed lines indicate the bunch-averaged μ_x (μ_y) per scan. The errors are statistical only and correspond approximately to the marker size.

and x scan 11. It is due to the vertical re-centering of the beams immediately following y scan 10.

Calibration constants σ_{vis}

Figure 7.19a illustrates the per-bunch visible cross sections for BCMV_EventOR determined in the four centred July VdM scans. The values are bunch current and length scale corrected. The correction factors are documented in section 7.1.

The consistency of the per-bunch visible cross sections σ_{vis} within a scan is reasonable and there are no obvious outliers. The agreement of the bunch-averaged σ_{vis} among different scans is better than for the July scans. The latter is more clearly visible in figure 7.19b: the maximum deviation between all four scans amounts to less than 0.6 %. If one only considers the scans 11, 14 and 15, the maximum difference is 0.3 %. The neglect of scan 10 is motivated by the large time gap between the x scan and y scan due to data acquisition problems. One assumption of the VdM scan procedure is that the transverse density profiles of the colliding bunches are constant over time; only for scans of a short duration this is approximately true. Thus the reason for σ_{vis} of scan 10 being an outlier may be emittance growth.

Table 7.8 gives an overview of the bunch-averaged σ_{vis} per scan and luminosity al-

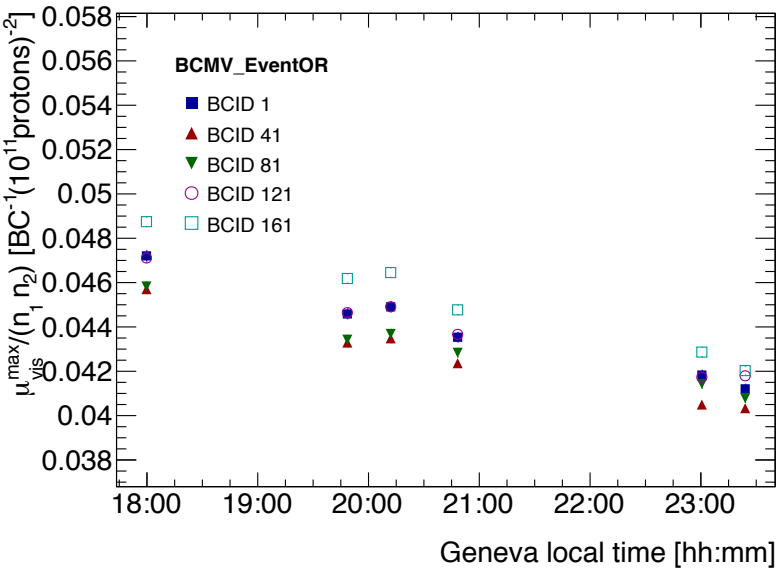

Figure 7.18.: Evolution of $\mu_{vis,spec}^{max}$ in time during LHC fill 3311 for the first five paired BCIDs. The plotted data points (from left to right) correspond to x scan 10, y scan 10, x scan 11, y scan 11, x scan 14 and y scan 14. The errors are statistical only and correspond approximately to the marker size.

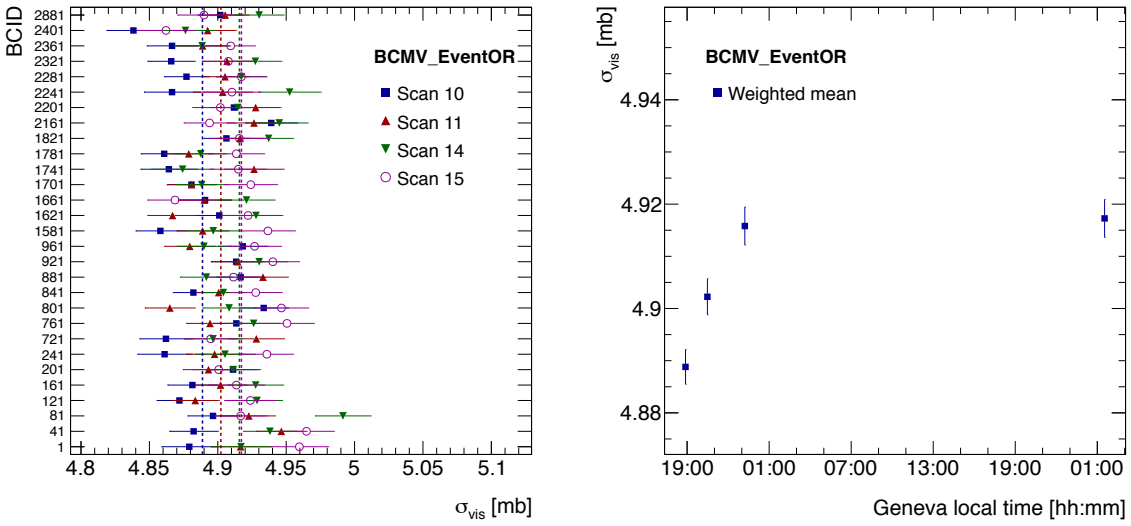

(a) Per-bunch σ_{vis}. The vertical dashed lines indicate the bunch-averaged σ_{vis} per scan.

(b) Bunch-averaged σ_{vis} plotted against the time of the scan.

Figure 7.19.: σ_{vis} obtained with BCMV_EventOR in the four centred November 2012 scans. The plotted data points (from left to right) in (b) correspond to scan 10, 11, 14 and 15. The errors are statistical only. Length scale and bunch current corrections are applied.

BCMV_EventOR				
Scan	$\overline{\sigma_{vis}}$ [mb]	χ^2/dof	RMS	Rel. RMS [%]
10	4.889 ± 0.0033	1.9	0.025	0.51
11	4.902 ± 0.0035	1.2	0.020	0.41
14	4.916 ± 0.0036	1.5	0.025	0.51
15	4.917 ± 0.0036	1.4	0.023	0.47
BCMH_EventOR				
Scan	$\overline{\sigma_{vis}}$ [mb]	χ^2/dof	RMS	Rel. RMS [%]
10	4.914 ± 0.0031	2.3	0.025	0.52
11	4.947 ± 0.0033	1.6	0.022	0.44
14	4.966 ± 0.0034	1.0	0.019	0.38
15	4.957 ± 0.0034	1.1	0.019	0.39
LUCID_EventOR				
Scan	$\overline{\sigma_{vis}}$ [mb]	χ^2/dof	RMS	Rel. RMS [%]
10	34.369 ± 0.0077	3.5	0.077	0.22
11	34.660 ± 0.0079	4.2	0.086	0.25
14	34.686 ± 0.0082	3.4	0.079	0.23
15	34.782 ± 0.0082	1.4	0.052	0.15

Table 7.8.: Error-weighted average of the per-bunch σ_{vis} obtained in the four centred November 2012 scans. The errors are statistical only. Length scale and bunch current corrections are applied.

gorithm. Similar to BCMV_EventOR, the agreement among scan 11, 14 and 15 is better than 0.4 % for BCMH_EventOR and LUCID_EventOR. However, when also considering scan 10, the variation of σ_{vis} surpasses 1 % for both BCMH_EventOR and LUCID_EventOR, as opposed to 0.6 % for BCMV_EventOR. The inconsistency among the algorithms can not be explained by statistical fluctuations. Because beam related uncertainties are fully correlated among different algorithms, they can be ruled out as a source of the inconsistency. Hence the variations must be caused by instabilities of the detector response. These are quantitatively assessed in section 7.4.

As observed in the July VdM scans, the χ^2/ndf of the average of the bunches in a scan is less good for LUCID than for BCM, even if the relative RMS of the per-bunch visible cross sections measured by LUCID is smaller. The reasoning remains unchanged and the worse χ^2/ndf is attributed to the high sensitivity of LUCID to systematic error sources.

7.4. Systematic uncertainties

Subject of this section are the systematic uncertainties of the visible cross sections obtained during the July and November VdM scans. The uncertainties can be divided into two groups: bunch current related and bunch current independent. The section is structured such that each type of uncertainty is dealt with in a separate subsection. Within each subsection, both the July and November uncertainties are discussed and then compared against each other. In the following, the bunch current related uncertainties are treated first, then the other ones.

Bunch currents

One necessary input to the VdM scan evaluation is the bunch current product, the knowledge of the individual bunch currents per beam is not required. Hence for VdM scans, only the uncertainty of the product of the bunch currents is of relevance. The precision of the bunch current product is mainly limited by four factors: the precision of the total currents as measured by the DCCTs, the precision of the bunch-by-bunch fractions measured by the FBCTs, and the precision of the ghost charge and satellite charge measurements.

DCCT scale

A quantitative analysis of the uncertainties of the total currents measured by the DCCTs is available in [48, 61] for various beam conditions, including those during VdM fills. However, the uncertainties are given as envelope uncertainties. This means, that the true values are guaranteed to be contained within the envelope interval, which is centred on the measured value and twice as big as the quoted uncertainty. The envelope uncertainties are transformed to pseudo-statistical 1σ-uncertainties[7] by multiplication with the factor 0.68. Here it is assumed, that the probability distribution function within the envelope interval is flat. The DCCT scale uncertainties for the July VdM scans are 0.21 %, for the November VdM scans they are 0.22 % and 0.23 %, depending on the fill. The uncertainties differ slightly, because the total intensities in July and November were different.

[7] For Gaussian distributed values, 68 % of the values lie in the interval $\pm 1\,\sigma$, where σ denotes the standard deviation of the Gaussian.

FBCT bunch-by-bunch fractions

The uncertainties of the bunch-by-bunch fractions measured by the FBCT are assessed via two different methods. First, the visible cross sections based on FBCT measurements are compared to the ones based on independent measurements of the ATLAS BPTX. Secondly, the FBCT and BPTX measurements are corrected for a possible non-linear response utilising the internal consistency of the per-bunch visible cross sections. Hence four different σ_{vis} values are compared: $\sigma_{vis,\mathrm{FBCT\_raw}}$ and $\sigma_{vis,\mathrm{BPTX\_raw}}$ denote the visible cross sections based on uncorrected FBCT and BPTX measurements; $\sigma_{vis,\mathrm{FBCT\_corrected}}$ and $\sigma_{vis,\mathrm{BPTX\_corrected}}$ denote the measurements corrected for a possible non-linear response.

In order to correct for a possible non-linear response of the FBCT, it is assumed, that the response can be approximated by a linear polynomial near a working point which is given by the average bunch current. Since the FBCT is only used for measuring bunch-by-bunch fractions, adding a constant offset to the raw FBCT measurements fully determines the slope of the linear response near the working point.

In a VdM scan, one measures for each colliding bunch pair i the corresponding $\sigma_{vis}^{(i)}$ via the relation:

$$\sigma_{vis}^{(i)} = \frac{2\pi\Sigma_x^{(i)}\Sigma_y^{(i)}}{n_1^{(i)}n_2^{(i)}}\mu_{vis}^{(i)}(0,0) \tag{7.5}$$

If one adds a constant offset c to all FBCT signals $s^{(k)}$, the bunch-by-bunch fraction $r^{(i)}$ of bunch i becomes:

$$r_b^{(i)} = \frac{s_b^{(i)} - c_b}{\sum_k (s_b^{(i)} - c_b)} \tag{7.6}$$

where the index $b \in 1, 2$ denotes beam 1 and beam 2 measurements. The index k denotes all bunches in beam 1 and beam 2, colliding as well as non-colliding. Since the FBCTs for both beams are independent, their signals may have different offsets c_1 and c_2. The change of the per-bunch visible cross sections $\sigma_{vis}^{(i)}$ determined based on the raw FBCT signals due to offsets is given by:

$$\sigma_{vis,\mathrm{FBCT\_corrected}}^{(i)}(c_1, c_2) = \sigma_{vis,\mathrm{FBCT\_raw}}^{(i)} \prod_{b=1,2} \left[\frac{n_b^{(i)}}{\sum_k n_b^{(k)}} \frac{\sum_k (n_b^{(k)} - c_b)}{(n_b^{(i)} - c_b)} \right] \tag{7.7}$$

where the term in the square brackets substitutes the uncorrected bunch-by-bunch fractions by the fractions based on the signals subject to an offset. This substitution must be done for either beam, hence the product over both beams.

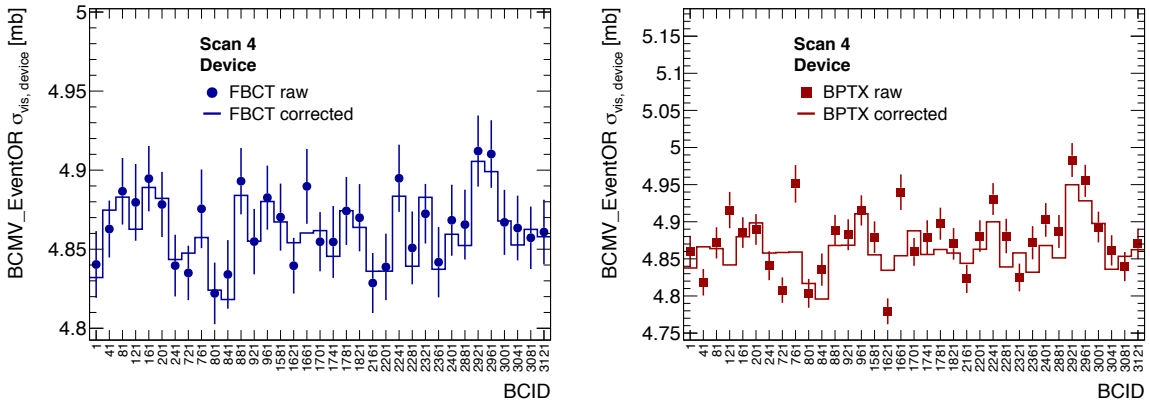

(a) FBCT **(b)** BPTX

Figure 7.20.: Per-bunch σ_{vis} for scan 4. The filled circles and squares correspond to visible cross sections based on raw FBCT and raw BPTX measurements, respectively. The solid lines indicate the visible cross sections obtained with the corrected FBCT or BPTX measurements. Errors are statistical only.

In order to find the offsets c_1 and c_2 for which the $\sigma^{(i)}_{vis,\mathrm{FBCT\_corrected}}$ are most consistent among each other, one needs to minimise the χ^2-function

$$\chi^2(c_1,c_2) = \sum_{i=1}^{N} \left(\frac{\sigma^{(i)}_{vis,\mathrm{FBCT\_corrected}}(c_1,c_2) - \overline{\sigma_{vis}}_{,\mathrm{FBCT\_corrected}}(c_1,c_2)}{\delta\sigma^{(i)}_{vis,\mathrm{FBCT\_corrected}}(c_1,c_2)} \right)^2 \tag{7.8}$$

where $\delta\sigma^{(i)}_{vis,\mathrm{FBCT\_corrected}}$ is the statistical error on the corrected per-bunch visible cross sections and $\overline{\sigma_{vis}}_{,\mathrm{FBCT\_corrected}}$ the visible cross section averaged over all paired bunches:

$$\overline{\sigma_{vis}}_{,\mathrm{FBCT\_corrected}}(c_1,c_2) = \frac{1}{N}\sum_{i=1}^{N} \sigma^{(i)}_{vis,\mathrm{FBCT\_corrected}}(c_1,c_2) \tag{7.9}$$

The correction for the BPTX measurements is analogous. The minimisation of the χ^2-function is done with a fit routine having the fit parameters c_1 and c_2. In this thesis, the determination of c_1 and c_2 is based on visible cross sections measured for the luminosity algorithm BCMV_EventOR.

As an example, figure 7.20 illustrates the four different types of visible cross sections obtained for scan 4: while the per-bunch $\sigma_{vis,\mathrm{FBCT\_raw}}$ and $\sigma_{vis,\mathrm{FBCT\_corrected}}$ are close to each other, the per-bunch $\sigma_{vis,\mathrm{BPTX\_corrected}}$ exhibit a much better internal consistency than the ones based on the uncorrected BPTX measurements. This result indicates, that the BPTX measurements suffered from a non-linear response during scan 4.

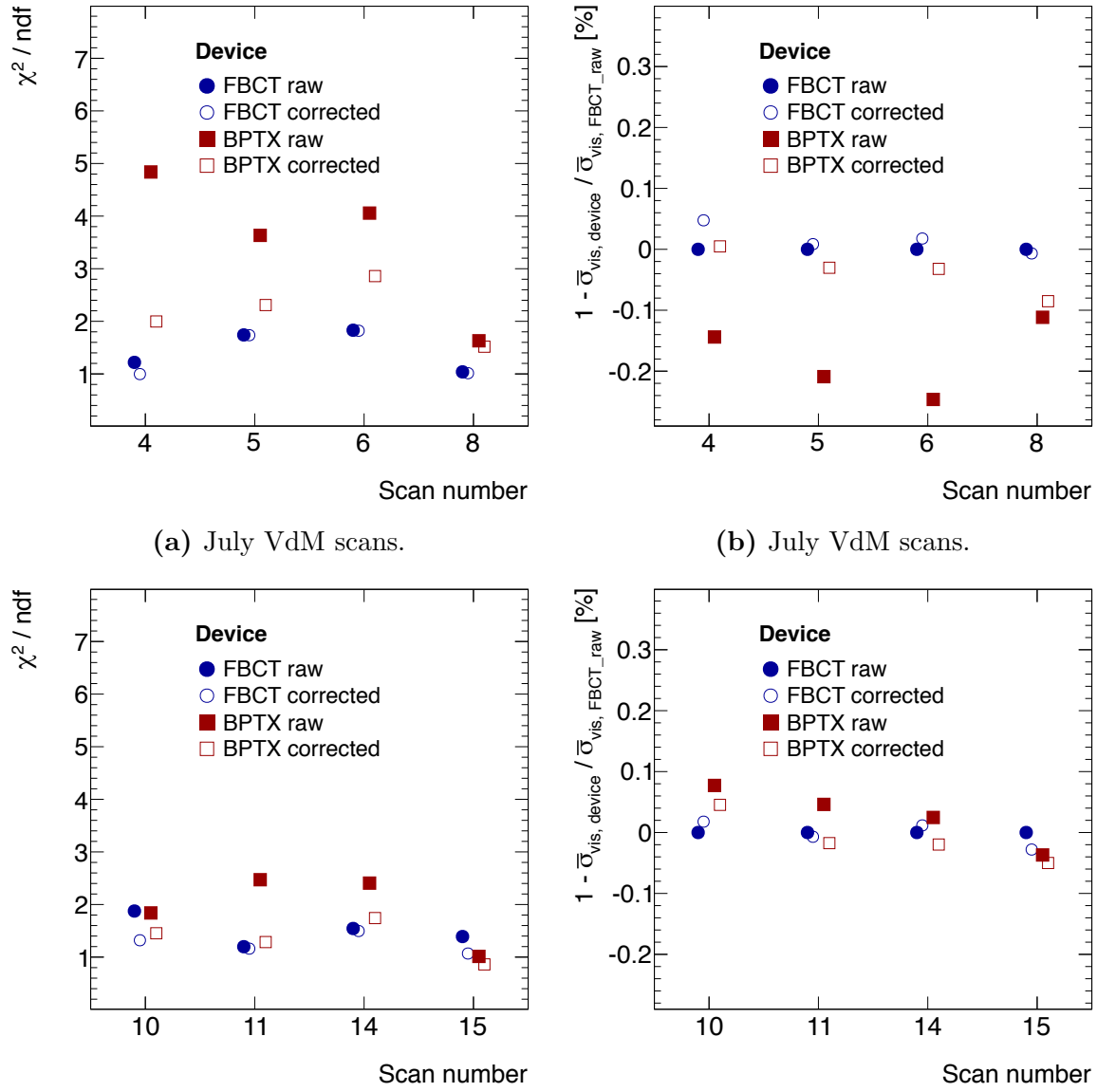

(a) July VdM scans.

(b) July VdM scans.

(c) November VdM scans.

(d) November VdM scans.

Figure 7.21.: The left plots illustrate the χ^2/ndf of the average of the per-bunch visible cross sections for the four different types of σ_{vis}. The right plots show the relative change of the four different types of σ_{vis} with respect to $\sigma_{vis,\mathrm{FBCT\_raw}}$. The upper plots correspond to the four centred July 2012 VdM scans, the lower ones to the four centred November 2012 VdM scans.

The χ^2/ndf of the average of the per-bunch visible cross sections is shown in the left plots of figure 7.21 for different scans. The number of degrees of freedom is given by the number of paired bunches minus one. The upper left plot depicts the July VdM scans, the lower left one the November VdM scans. The σ_{vis} values obtained with the uncorrected FBCT measurements tend to have a better internal consistency than the ones with the uncorrected BPTX measurements. This indicates, that the bunch-by-bunch fractions measured by the FBCT are closer to the true fractions than the ones measured by the BPTX. While a correction of the FBCT measurements has little impact on the consistency of the per-bunch σ_{vis}, a correction of the BPTX measurements significantly improves the σ_{vis} consistency for many of the scans, revealing a non-linear response of the BPTX.

The right plots in figure 7.21 illustrate the relative difference of the bunch-averaged $\overline{\sigma}_{vis,\mathrm{FBCT\_raw}}$, $\overline{\sigma}_{vis,\mathrm{BPTX\_raw}}$, $\overline{\sigma}_{vis,\mathrm{FBCT\_corrected}}$ and $\overline{\sigma}_{vis,\mathrm{BPTX\_corrected}}$ with respect to the reference cross section $\overline{\sigma}_{vis,\mathrm{FBCT\_raw}}$. By definition, the data points corresponding to the raw FBCT measurements are zero. The maximum deviation between the different type of visible cross sections is larger for the July scans than for the November ones.

The visible cross section uncertainty originating from the bunch-by-bunch fractions is taken as the maximum change of the average visible cross sections among the scans when switching from uncorrected FBCT to corrected FBCT or corrected BPTX measurements. Uncorrected BPTX measurements are not considered, since they are affected by a non-linear response. Hence the uncertainties for the July VdM scans are 0.03 % and 0.08 %, depending on the fill. For the November scans they are 0.05 %.

Ghost charge and satellite corrections

The ghost charge measurement is performed by LHCb. Its uncertainty is estimated by LHCb and dominated by the knowledge of the trigger efficiency. Since the beam 1 and beam 2 measurements are highly correlated, the uncertainties for both beams are added linearly. For the July and November scans, the uncertainties on σ_{vis} arising from the ghost charge measurement range from 0.037 % to 0.09 %, depending on the fill.

The uncertainties of the LDM satellite bunch measurements are evaluated to be 25 % of the measured satellite charges. For the July scans, the uncertainty on σ_{vis} originating from the satellite bunch measurements is 25 % of the correction listed in table 7.4. For November, the uncertainty is taken as 100 % of the neglected correction. The uncertainties on σ_{vis} originating from the satellite bunch measurements are between 0.04 % and 0.14 %, depending on the fill.

	July 2012 corrections		November 2012 corrections	
	Fill	Uncertainty on σ_{vis} [%]	Fill	Uncertainty on σ_{vis} [%]
DCCT scale	2855	0.21	3311	0.22
	2856	0.21	3316	0.23
FBCT	2855	0.03	3311	0.05
	2856	0.08	3316	0.05
Satellites	2855	0.12	3311	0.11
	2856	0.14	3316	0.04
Ghost charge	2855	0.09	3311	0.037
	2856	0.09	3316	0.046
Total	2855	0.26	3311	0.25
	2856	0.28	3316	0.24

Table 7.9.: Uncertainties on σ_{vis} originating from the bunch currents for all four fills with injection optics, during which VdM scans were performed.

Total current uncertainty

The overall σ_{vis} uncertainties originating from the bunch currents are listed in table 7.12. Additionally, the individual uncertainty contributions are shown. For calculating the total uncertainties, the individual contributions were added in quadrature.

Orbit drift correction

Figure 7.22 illustrates the ratio of the orbit drift corrected visible cross sections to the ones neglecting the drifts. The shown ratios are based on data for the luminosity algorithm BCMV_EventOR and correspond to the eight centred VdM scans in July and November 2012. Even though not depicted here, the ratios are in agreement with the ones for BCMH_EventOR or LUCID_EventOR.

As commented on in section 6.2, the orbit drifts at the IP are extrapolated from BPMs on either side of the IP, thus providing two independent measurements. The orbit correction is based on the average of both measurements; considering the consistency of both measurements, the uncertainty of the orbit correction is conservatively taken as half of the maximum correction among the scans.

Scan 10 is neglected for the calibration of σ_{vis} because of the large time difference between the x and the y scan. The July VdM scan uncertainty due to the orbit drift correction is estimated to be 0.36 %, the November one to be 0.35 %.

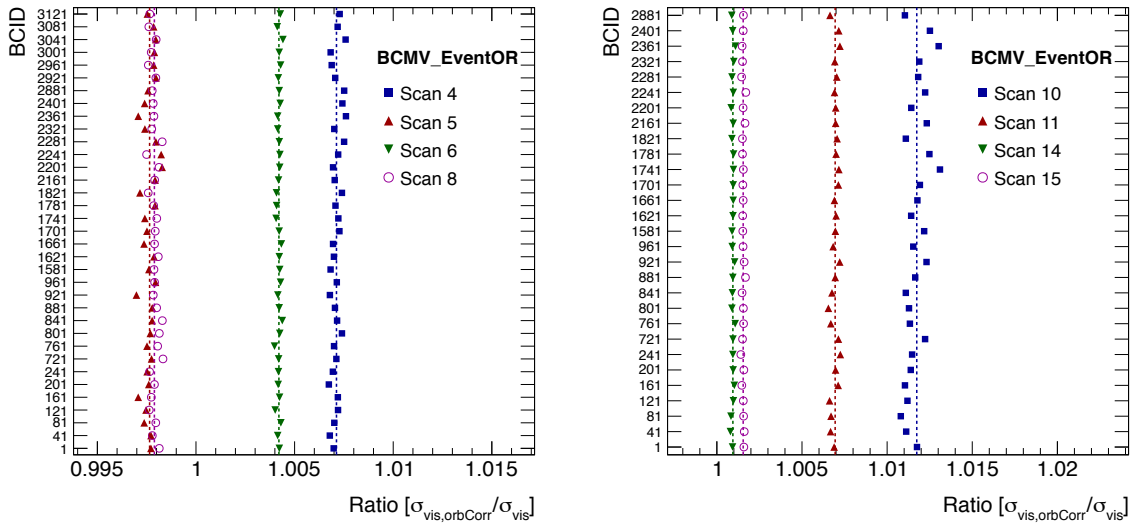

(a) July VdM scans **(b)** November VdM scans

Figure 7.22.: Impact of the orbit drift corrections on the per-bunch σ_{vis} for the July and November 2012 VdM scans.

Beam position jitter

Whilst stepwise separating the beams during a VdM scan, it may be, that the real beam positions are randomly displaced by a small amount with respect to the desired beam positions. In the following, this effect is named beam position jitter. The additional beam separation due to jitter for a given scan step is assumed to be less than 1.5 μm, defined by the maximum deviation of the desired separation from the measured separation during the length scale calibration carried out in July 2012.

In the context of the evaluation of the ATLAS 2011 VdM scans, the impact of the jitter on σ_{vis} was studied based on simulated VdM scan curves [17]. The bias was estimated to be 0.3 % for a jitter on the order of 1 % of the convolved bunch size. The jitter during the July and November scans is 1.5 μm/130 μm=1.2 % of the convolved bunch size. Scaling the bias for the 2011 scans according to the relative jitter, the uncertainties for the 2012 VdM scans are estimated to be 0.36 %.

Emittance growth & other non-reproducibility

The observed non-reproducibility of σ_{vis} among the different VdM scans in November may be due to emittance growth or other unknown effects. It is conservatively treated as a separate uncertainty contribution, even if perhaps caused by effects covered already by other uncertainty types.

For the three luminosity algorithms analysed in this thesis, the maximum relative deviation between the bunch-averaged visible cross sections among the scans 11, 14 and 15 is 0.39 %. This value defines the non-reproducibility uncertainty for the November scans.

The non-reproducibility of σ_{vis} in the July scans amounts to approximately 2 %. Since this variation is largely attributed to non-factorisation of the transverse density profiles into independent x and y components, it is accounted for by the non-linear transverse correlation uncertainty and discussed later.

Bunch-to-bunch σ_{vis} consistency

Within a scan, the observed RMS of the bunch-by-bunch visible cross sections is larger than the RMS expected from the statistical error of the bunch-averaged $\overline{\sigma_{vis}}$. This is reflected by values of χ^2/ndf greater than 1.0 in the average calculation. The component of the observed RMS, which can not be explained by statistics, is accounted for by an uncertainty labelled bunch-to-bunch σ_{vis} consistency. It is calculated as

$$\sqrt{\mathrm{RMS}^2 - \left(\sqrt{N}\,\delta\overline{\sigma_{vis}}\right)^2} \tag{7.10}$$

where RMS is the root mean square of the per-bunch σ_{vis}, N the number of colliding bunch pairs and $\delta\overline{\sigma_{vis}}$ the statistical error of the bunch-averaged visible cross section. All required input to formula (7.10) is contained in table 7.6 and 7.8.

The uncertainty on σ_{vis} is conservatively estimated to be the maximum non-statistical component among the different scans and luminosity algorithms. The July VdM scan uncertainty is 0.42 %, the November one is 0.38 %. As before, scan 10 is neglected.

Fit model

The assessment of the uncertainty originating from the choice of the scan curve model is based on the change of the visible cross section when using different fit models. The primary fit model for the November scans is a common Gaussian plus a constant background component. However, the Super Gaussian model also proved to be able to describe the scan curves well. The χ^2/ndf values of the scan curve fits are similar to the common Gaussian model.

The fit model uncertainty for the November VdM scans is taken as the maximum change of the bunch-averaged visible cross sections among scans 11, 14 and 15. All three luminosity algorithms are considered and the fit model uncertainty for the November

VdM scans is found to be 0.84 %.

The primary fit model for the July scans is a Double Gaussian plus constant background component, the χ^2/ndf values are close to the ideal 1.0. Since the transverse density profiles of the colliding bunches during the July VdM scans exhibit signs of significant transverse correlations, a factorisable scan curve model is inadequate for the determination of the visible cross section. Thus the fit model uncertainty for the July VdM scans is accounted for by the non-linear transverse correlation uncertainty.

Background subtraction

The scan curves measured during the July and November VdM scans are fitted with a Double Gaussian and a common Gaussian, respectively. Both models include a constant background component which is not considered as real luminosity and assumed to originate from noise or beam background. Alternatively, one can first correct the scan curves for noise, afterglow and beam background and afterwards consider the constant background component as real luminosity. These corrections make use of the $\mu_{vis,spec}$ measured in BCs preceding the paired BCs and of the $\mu_{vis,spec}$ measured for non-colliding bunches.

A study considering all three luminosity algorithms yields a maximum change of σ_{vis} of 0.71 % for the November scans when using the first or second method. The maximum change is observed for BCMV_EventOR, the changes for BCMH_EventOR and LUCID_EventOR are considerably smaller. This is most probably a consequence of the increased noise level of the BCMV_EventOR algorithm at the time of the November scans. The noise originated from the BCMV hardware and was already observed before the November VdM scans. The cause of the noise is unknown.

Figure 7.23 illustrates the constant background components $p_0^x/(n_1 n_2)$ measured during the July and November VdM scans. The spread of the per-bunch backgrounds within a scan is due to different bunch current products $(n_1 n_2)$. The values of $p_0^x/(n_1 n_2)$ are more than one order of magnitude larger in November than in July. Since the background subtraction study was only performed for the November scans, the July uncertainty is set to the one of the November scans. Because the BCMV_EventOR noise is much smaller in July than in November, this is assumed to be a conservative uncertainty estimation.

Transverse correlations

The non-factorisation of the transverse density profiles of the colliding bunches into independent x and y components is also referred to as transverse correlations. In section

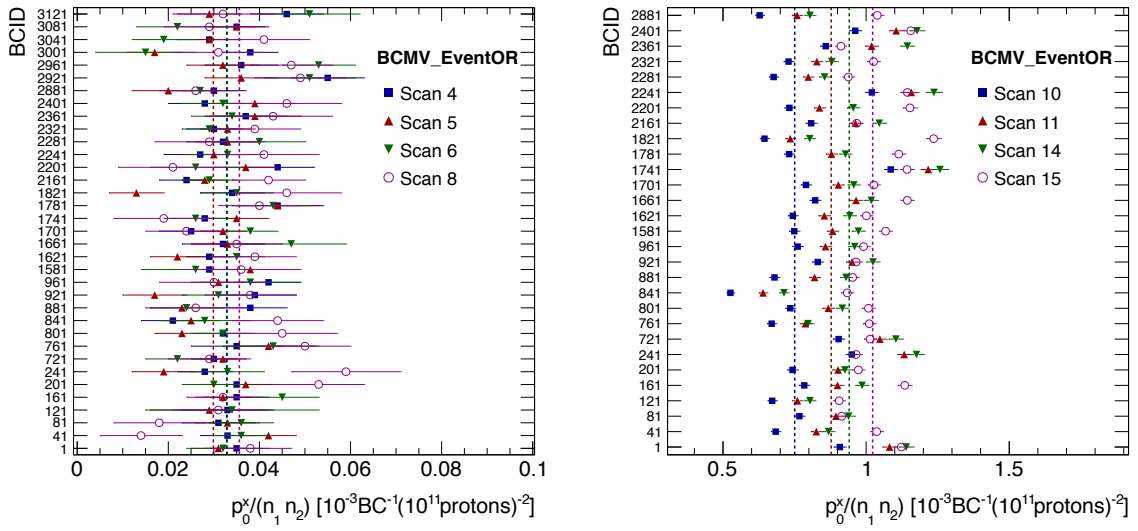

(a) July 2012 VdM scans **(b)** November 2012 VdM scans

Figure 7.23.: Comparison of the constant background component p_0^x obtained from the horizontal scans for the centred July and November 2012 VdM scans. The vertical dashed lines indicate the bunch-averaged p_0^x per scan. The errors are statistical only.

5.1 it is proved, that for absent transverse correlations, the convolved transverse bunch sizes Σ_x and Σ_y obtained in a VdM scan are independent of the separation in the non-scan plane and the factorisation can be experimentally probed via offset scans. Since the peak interaction rates in the offset scans are much lower than in centred scans, they are evaluated with the luminosity algorithm LUCID_EventOR as explained in section 7.3.

Figure 7.24 comprises two plots. The left plot illustrates the evolution of the horizontal convolved bunch sizes Σ_x during the July VdM scans, the right one depicts the evolution of the vertical convolved bunch sizes Σ_y. For better readability, only the first five paired BCIDs are shown. Scans 4, 5, 6 and 7 took place in the same fill. While scans 4-6 are centred scans, scan 7 is an offset scan with a separation of 344 μm in the non-scan plane. The increase of Σ_x and Σ_y between scan 4 and 6 is due to emittance growth. However, Σ_x and Σ_y measured in scan 7 are roughly 10 % larger than expected from the extrapolation of the convolved bunch sizes during scan 4-6 to the time of scan 7. Scan 8 and 9 were conducted in a different fill; the former is a centred scan, the latter an offset scan with a separation of 369 μm in the non-scan plane. The increase of Σ_x and Σ_y by about 20 % between scan 8 and 9 is unlikely due to emittance growth.

An overview of the bunch-averaged convolved bunch sizes during the July scans is given in table 7.10. Since Σ_x and Σ_y significantly depend on the non-scan plane separation,

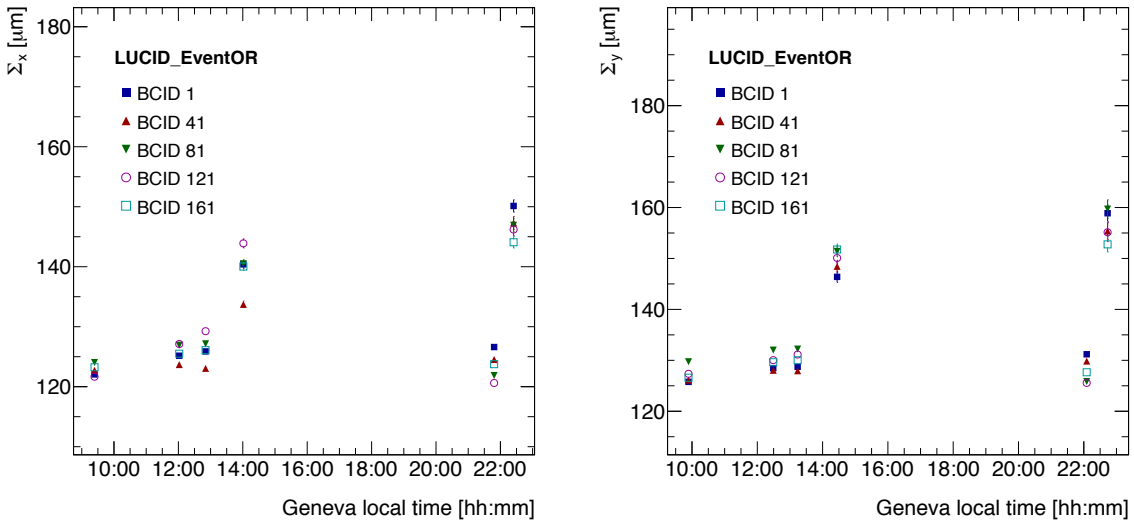

(a) Σ_x **(b)** Σ_y

Figure 7.24.: Evolution of the convolved bunch sizes Σ_x and Σ_y obtained by the algorithm LUCID_EventOR for the July 2012 VdM scans. The data points (from left to right) correspond to scan 4, 5, 6, 7, 8 and 9. Scans 4-7 took place in the same LHC fill, scan 8 and 9 were carried out in a different fill. Errors are statistical only.

the July VdM scans are affected by transverse correlations.

The evolution of the convolved bunch sizes Σ_x and Σ_y during the November VdM scans is depicted in figure 7.25. The left plot corresponds to Σ_x, the right one to Σ_y. Only the first five paired BCIDs are shown. Scans 10-14 took place in the same fill. Scans 10, 11 and 14 are centred scans, while scans 12 and 13 are offset ones. The separation in the non-scan plane during scan 12 is 344 μm, during scan 13 it is 197 μm. Performing both offset scans with a different non-scan plane separation allows for a thorough check of the validity of the factorisation assumption.

Scan	$\overline{\Sigma_x}$ $[\mu m]$	Rel. RMS [%]	$\overline{\Sigma_y}$ $[\mu m]$	Rel. RMS [%]
4	120.3	1.7	125.7	1.9
5	123.2	1.8	128.1	2.0
6	123.7	2.2	128.5	2.1
7	136.5	2.5	148.2	1.8
8	121.2	2.3	127.8	1.7
9	143.7	2.6	155.0	2.0

Table 7.10.: Mean and relative RMS of the per-bunch $\Sigma_{x/y}$ measured by LUCID_EventOR in the July 2012 VdM scans.

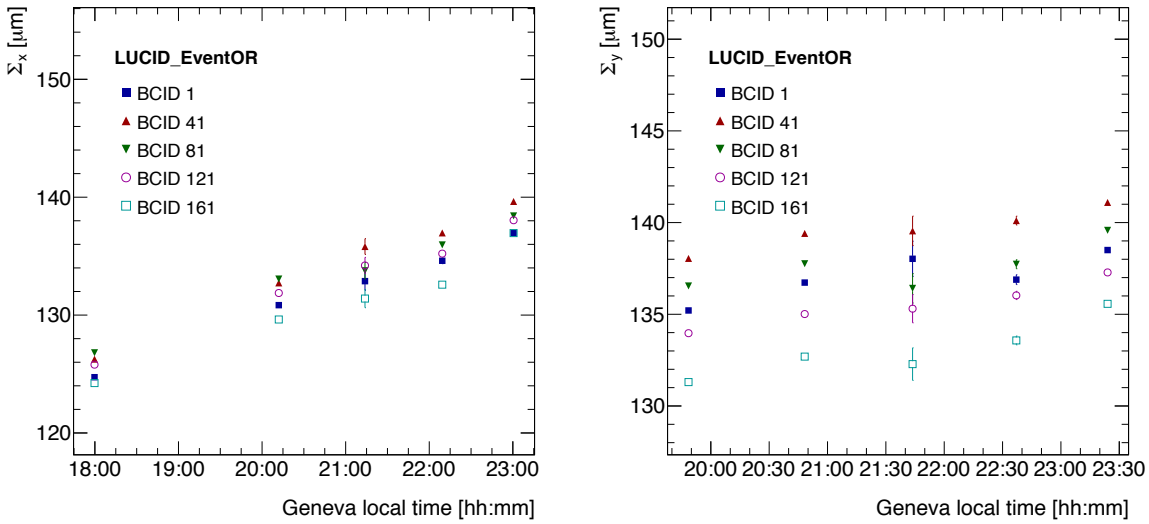

(a) Σ_x **(b)** Σ_y

Figure 7.25.: Evolution of the convolved bunch sizes Σ_x and Σ_y obtained by the algorithm LUCID_EventOR for the November 2012 VdM scans. The data points (from left to right) correspond to scan 10, 11, 12, 13 and 14. All shown scans took place in the same LHC fill. Errors are statistical only.

After interpolating the convolved bunch sizes obtained during scans 10, 11 and 14 to the times of the offset scans, one finds, that Σ_x and Σ_y measured during the offset scans deviate by less than 1 % from the values expected for absent transverse correlations. An overview of the bunch-averaged convolved bunch sizes during the November scans is given in table 7.11.

While during the July VdM scans significant transverse correlations are observed, they seem negligible during the November scans. Consequently, the belonging uncertainties are larger for July than for November. The quantitative uncertainty estimation is based on a combined fit to the reconstructed vertices at the time of the VdM scans which makes use of the shape of the luminous region and the absolute number of vertices. The procedure is documented in detail in chapter 8. The resulting uncertainties are 4.9 % for the July and 0.2 % for the November scans.

Beam-beam effects

Beam-beam effects are interactions between colliding beams. The collision of particles at the IP is a wanted beam-beam effect. Electromagnetic forces which the colliding beams exert on each other are an unwanted beam-beam effect.

During the VdM scans the LHC contained only a few, widely spaced particle bunches

Scan	$\overline{\Sigma_x}$ [μm]	Rel. RMS [%]	$\overline{\Sigma_y}$ [μm]	Rel. RMS [%]
10	124.1	1.8	131.3	2.3
11	129.6	1.7	132.8	2.2
12	131.0	1.4	132.5	1.9
13	133.2	1.5	133.6	2.0
14	136.3	1.5	135.2	2.0
15	123.1	1.3	129.8	1.2

Table 7.11.: Mean and relative RMS of the per-bunch $\Sigma_{x/y}$ measured by LUCID_EventOR in the November 2012 scans.

and long range interactions of the bunches were not possible. The two beam-beam effects relevant for the evaluation of the VdM scans are called dynamic-β and beam-beam deflection. In the following they are conservatively treated independently.

Dynamic-β describes a mutual focussing or de-focussing of the colliding bunches which depends on the transverse separation, hence the name "dynamic". Therefore the transverse bunch sizes change during the scans, affecting the bunch overlap integral and the measured interaction rate. The dynamic-β effect during VdM scans at the LHC was studied in [62].

Beam-beam deflection describes the mutual deflection of colliding bunches. The deflection depends on the transverse beam separation and results in a modification of the beam orbits. The deflection must be treated as an additional separation to the nominal beam separation.

Dynamic-β

The impact of the dynamic-β effect on the visible cross section was evaluated in the context of the ATLAS 2011 VdM scans in [17] and estimated to be 0.5 %. The study is based on simulated scan curves accounting for, or neglecting, the dynamic-β effect. The uncertainty is estimated by the difference of the visible cross sections obtained from either set of scan curves.

The dynamic β-effect scales with the ratio n/ϵ, where n is the number of protons per bunch and ϵ the normalised emittance. Scaling the dynamic-β uncertainty for 2011 according to the November 2012 conditions, yields an uncertainty of 0.66 %. Since the bunch intensities and normalised emittances during the July scans were similar to the ones in November, this uncertainty is also assigned to the July scans.

Beam-beam deflection

Since the impact of the beam-beam deflection effect on the VdM scan procedure was thought to be negligible until recently, detailed studies are not yet available at the time of writing. Based on early studies, a conservative upper limit for the impact is 1.8 %. When precise and reliable simulations of the effect become available, the calibration constants can be corrected for the beam-beam deflection, hence reducing the uncertainty.

Reference $\mathcal{L}_{spec}$

The specific luminosity $\mathcal{L}_{spec}^{(i)}$ of paired bunch crossing i is defined as the luminosity for head-on collisions divided by the bunch current product. Using equation (5.21), the specific luminosity can be written as

$$\mathcal{L}_{spec}^{(i)} = \frac{\mathcal{L}^{(i)}(0,0)}{n_1^{(i)} n_2^{(i)}} = \frac{f_r}{2\pi \Sigma_x^{(i)} \Sigma_y^{(i)}} \tag{7.11}$$

where Σ_x and Σ_y are the convolved transverse bunch sizes and f_r the collision frequency. Since this observable is independent of the detection efficiency and of the bunch currents, it is suited for consistency checks of the convolved bunch sizes measured by different luminosity algorithms. The uncertainty associated with the choice of the reference $\mathcal{L}_{spec}$ is given by the maximum relative deviation among all scans of the bunch-averaged $\mathcal{L}_{spec}$ determined via BCMV_EventOR with respect to BCMH_EventOR or LUCID_EventOR.

Figure 7.26 illustrates the per-bunch $\mathcal{L}_{spec}$ ratios for all centred July VdM scans, the maximum relative deviation is 0.3 %. Figure 7.27 shows the per-bunch $\mathcal{L}_{spec}$ ratios for all centred November VdM scans, the maximum relative deviation is 0.6 % and twice as large as for the July scans.

μ-dependence during Van der Meer scan

The mean number of interactions per BC during both the July and November VdM scans covers the range $0 < \mu < 0.5$. The consistency of luminosity measurements of different detectors and algorithms in this range is estimated to be better than 0.5 % based on the observations during the ATLAS 2011 VdM scans [17]. Even though part of the μ-dependence is already accounted for by the reference $\mathcal{L}_{spec}$ uncertainty, the variation is treated conservatively as an independent uncertainty.

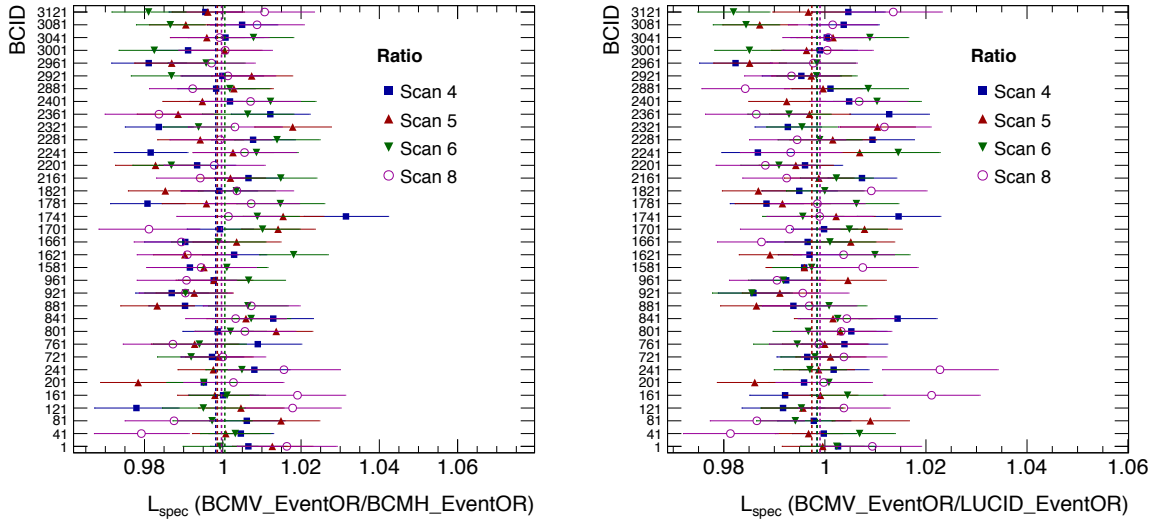

(a) BCMV_EventOR / BCMH_EventOR **(b)** BCMV_EventOR / LUCID_EventOR

Figure 7.26.: Comparison of the per-bunch $\mathcal{L}_{spec}$ obtained via different algorithms for the four centred July 2012 scans. The vertical dashed lines indicate the bunch averaged ratio per scan. Errors are statistical only.

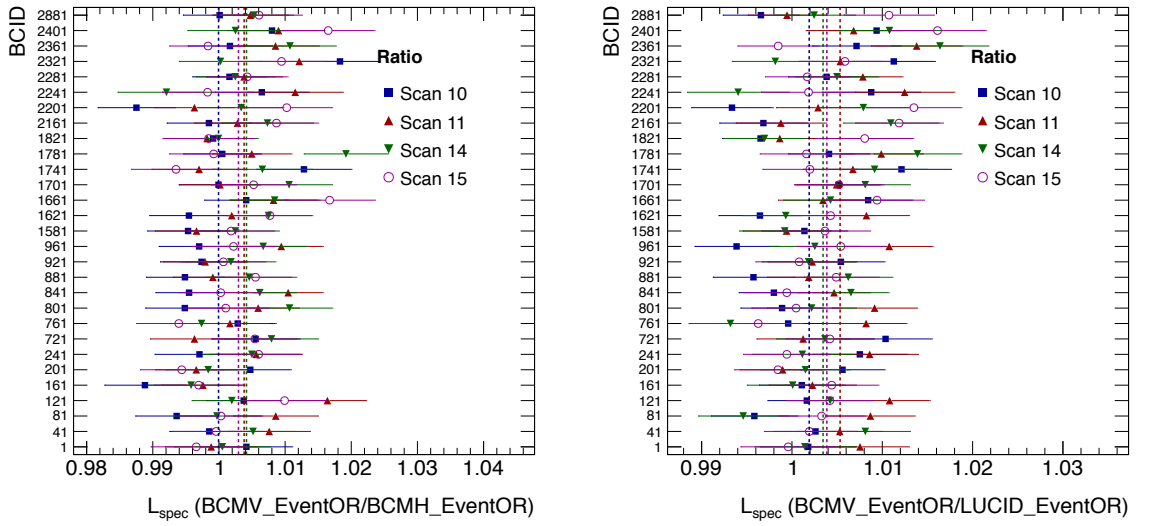

(a) BCMV_EventOR / BCMH_EventOR **(b)** BCMV_EventOR / LUCID_EventOR

Figure 7.27.: Comparison of the per-bunch $\mathcal{L}_{spec}$ obtained via different algorithms for the four centred November 2012 scans. The vertical dashed lines indicate the bunch averaged ratio per scan. Errors are statistical only.

Length scale calibration

Since no systematic uncertainties related to the length scale calibration are known, its uncertainty is given by the statistical error of 0.1 %. The uncertainty is assigned to both the July and November VdM scans.

ID length scale

By means of the length scale calibration, the nominal separation scale is replaced by the more precise inner detector (ID) based separation scale. Using Monte Carlo studies, the impact of misaligned inner detector geometries on the ID based scale was conservatively estimated to be 0.3 % [17]. The geometries were varied on condition, that they are still compatible with data-driven ID alignments. This uncertainty is identical for the July and November VdM scans.

Combined uncertainties

The combined uncertainties on the visible cross section σ_{vis} for the July and November 2012 VdM scans are shown in table 7.12. Additionally, the table lists the individual uncertainty contributions. For calculating the total uncertainties, they are added in quadrature. The total uncertainty for the July scans is 5.40 % and dominated by the uncertainty associated with transverse correlations; the second largest uncertainty contribution originates from the beam-beam deflection. The total uncertainty for the November scans amounts to 2.50 % and is dominated by the beam-beam deflection uncertainty.

	July 2012	November 2012
	Uncertainty on σ_{vis} [%]	Uncertainty on σ_{vis} [%]
DCCT calibration	0.21	0.22
FBCT bunch-by-bunch fractions	0.08	0.05
Ghost charge and satellite corrections	0.17	0.12
Subtotal, bunch current product	0.28	0.25
Orbit-drift correction	0.36	0.35
Beam position jitter	0.36	0.36
Emittance growth & other non-reproducibility	-*	0.39
Bunch-to-bunch σ_{vis} consistency	0.42	0.38
Fit model	-*	0.84
Background subtraction	0.71	0.71
Transverse correlations	4.90	0.20
Dynamic-β	0.66	0.66
Beam-beam deflection	1.80	1.80
Reference $\mathcal{L}_{spec}$	0.30	0.60
μ-dependence during VdM scan	0.50	0.50
Length scale calibration	0.10	0.10
ID length scale	0.30	0.30
Subtotal, calibration-scan systematics	5.39	2.49
Total	5.40	2.50

* Attributed to non-linear transverse correlations

Table 7.12.: Uncertainties on σ_{vis} for the July and November 2012 VdM scans.

8. A combined fit to the luminous region

The determination of the overlap integral of the transverse bunch density profiles of the colliding bunches in VdM scans is based on the dependency of the visible interaction rate on the transverse beam separation. The simultaneous measurement of the bunch currents allows to derive the absolute luminosity.

A partially complementary method for absolute luminosity measurements during VdM scans is based not only on the interaction rate, but it also uses spatial information on the luminous region [63]. The latter is also known as beamspot. Since the corresponding fit makes use of both the visible interaction rate and the beamspot shape, it is referred to as combined fit in the following. The spatial density profile of the beamspot is experimentally accessible using vertices reconstructed from the inner detector data. The principle of vertexing is, that if different particle tracks share a common intersection point, its location is likely to be an interaction vertex.

If the transverse density profiles of the colliding bunches factorise into independent x and y components, the normalised spatial density of the luminous region is independent of the horizontal and vertical transverse beam separation. Therefore only a non-factorisable model of the density profiles of the colliding bunches can explain variations of the size and shape of the luminous region when separating the beams. From this follows the major advantage of the combined fit compared to the common VdM scan procedure: while the combined fit is sensitive to transverse correlations, the VdM fit is not.

In this chapter, first the theory of combined fits is detailled and afterwards a non-factorisable fit model is applied to the vertexing data recorded during the July and November VdM scans. Finally, the visible cross sections obtained with the combined fit are compared to the ones of the VdM fit.

8.1. Theory

The luminosity for collisions of beams with a longitudinally bunched particle structure was introduced in section 4.1 and is given by equation (4.3):

$$\mathcal{L} = K\, n_1 n_2 f_r n_b \iiint_{-\infty}^{\infty} \rho_1(x,y,z,t)\rho_2(x,y,z,t)dxdydzdt \tag{8.1}$$

All variables are defined in section 4.1. The normalised spatial beamspot density follows from equation (4.3) and is:

$$\rho_{\mathrm{LR}}(x,y,z) = \frac{1}{\mathcal{L}} K\, n_1 n_2 f_r n_b \int_{-\infty}^{\infty} \rho_1(x,y,z,t)\rho_2(x,y,z,t)dt \tag{8.2}$$

The factor $1/\mathcal{L}$ ensures the proper normalisation. Since each measured vertex location has a limited precision, the spatial density of the reconstructed vertices is identical to ρ_{LR} convolved with the vertex resolution function r. A further complication is, that the vertex resolution is different for each vertex and depends on the number of tracks and their transverse momentum. The vertex resolution is obtained from the vertex fit where the resolution function is assumed to be a Gaussian.

The determination of the individual bunch parameters, which best describe the measured beamspot and interaction rates at different beam separations, is based on a simultaneous extended maximum-likelihood fit. A general introduction to maximum-likelihood fits is available in [64].

The likelihood L_k of the normalised spatial vertex distribution measured in scan step k is given by:

$$L_k = \prod_{i=1}^{N_k} (r_i * \rho_{\mathrm{LR,k}}(x_i, y_i, z_i)) \tag{8.3}$$

where the index i denotes all reconstructed vertices. The expected measured spatial distribution for each vertex is given by the expected 'true' spatial distribution convolved with the vertex specific resolution function r_i. Even though not explicitly indicated, one must ensure that the convolved distributions are still normalised. When evaluating the expressions for $\mathcal{L}$ and ρ_{LR} for a scan step, the corresponding beam separation must be taken into account.

So far only the spatial distribution of the vertices was considered. In order to also make use of the absolute number of reconstructed vertices in scan step k, one uses the extended likelihood $\tilde{L}$ which is defined as

$$\tilde{L}_k = P_k \cdot L_k \tag{8.4}$$

where P_k is the probability that N_k vertices are reconstructed in scan step k, if the number of expected reconstructed vertices is μ_k. Under the assumption, that the distribution of the number of expected vertices follows a Poisson distribution, one can write:

$$P_k(N_k, \mu_k) = \frac{\mu_k^{N_k} e^{-\mu_k}}{N_k!} \tag{8.5}$$

In order to obtain the calibration constant σ_{vis} from the combined fit, μ_k needs to be expressed in terms of σ_{vis}. In the following, vertexing is employed for event counting and an event is defined as a BC in which at least one vertex is reconstructed. The probability of observing an event in a BC was derived in equation (6.20):

$$P_{\text{Event}}(\mu_{vis}) = 1 - e^{-\mu_{vis}} \tag{8.6}$$

The number of events in scan step k is given by $P_{\text{Event}}(\mu_{vis})$ multiplied by the number of BCs during scan step k, where the number of BCs is the product of the revolution frequency f_r and the known duration of the scan step, labelled t_k.

Using the identity $\mu_{vis}{=}\mathcal{L}_k\sigma_{vis}/f_r$ from equation (6.13), one is finally able to express μ_k as a function of σ_{vis}:

$$\mu_k = \left[1 - \exp\left(-\frac{\mathcal{L}_k \sigma_{vis}}{f_r}\right)\right] t_k f_r \tag{8.7}$$

With a model of the three-dimensional particle densities of the colliding bunches, one can express $\mathcal{L}_k$ in terms of the model parameters, since the values of the parameters occurring in front of the beam density integral in equation (4.3) are known. Consequently, μ_k is a function of σ_{vis} as well as of the parameters of the particle density model for the colliding bunches. Because ρ_{LR} only depends on the parameters of the particle density model, $\tilde{L}_k$ can be expressed in terms of σ_{vis} and the parameters of the particle density model. Hence a fit maximising the extended likelihood, yields σ_{vis} and the density model parameters.

In order to fit all scan steps simultaneously, one defines the simultaneous extended likelihood as the product of the extended likelihoods corresponding to the different scan steps:

$$\tilde{L}_{tot} = \prod_k \tilde{L}_k \tag{8.8}$$

The simultaneous extended maximum-likelihood fit presented in the subsequent section was implemented with RooFit, which is a toolkit commonly used for modelling event distributions in physics analyses [65].

8.2. Combined fit analysis

In order to precisely measure the beamspot corresponding to a colliding bunch pair, a large number of reconstructed vertices is required. Since the ATLAS data acquisition system has a limited bandwidth, it is in general not possible to reconstruct all interaction vertices for all paired BCIDs. Therefore the trigger during the ATLAS VdM scans was configured such that only three BCIDs were triggered on with a high rate.

During the July VdM scans, the chosen BCIDs were 1, 721 and 1821; during the November scans, the chosen BCIDs were 1, 2361 and 2881. The employed trigger was a minimum bias trigger, which efficiently rejects BCs containing no events. The peak trigger rates per BCID during the scans were about 1.5 kHz. One should note, that the rate of reconstructed vertices is subject to trigger dead time.

It was explained in section 6.3, that the event counting method relies on the assumption, that the probability to observe an interaction in a BC is independent of the total number of interactions. To validate this assumption for the vertexing based event counting, the number of vertex events is used to perform a common VdM scan analysis. The convolved transverse bunch sizes Σ_x and Σ_y obtained with vertexing are compared to the ones obtained with the luminosity algorithm BCMV_EventOR. As for BCMV_EventOR, the July and November scan curves are fitted with a Double Gaussian and common Gaussian, respectively.

Figure 8.1 illustrates the comparison of the convolved bunch sizes. While a good consistency between vertexing and BCMV_EventOR is observed in the July scans, it is less good for the November ones. There the deviation is as large as about 1.5 %. The reason for the worse consistency in November for some of the BCIDs is unclear.

Before performing a combined fit to the reconstructed vertices, one needs to chose a model for the particle densities of the colliding bunches. The combined fit carried out in this thesis assumes that the density profiles of the bunches can be modelled by a weighted sum of two three-dimensional Gaussians with common mean [63]. The widths in the x and y plane are independent, the widths in the z plane are identical for both Gaussians

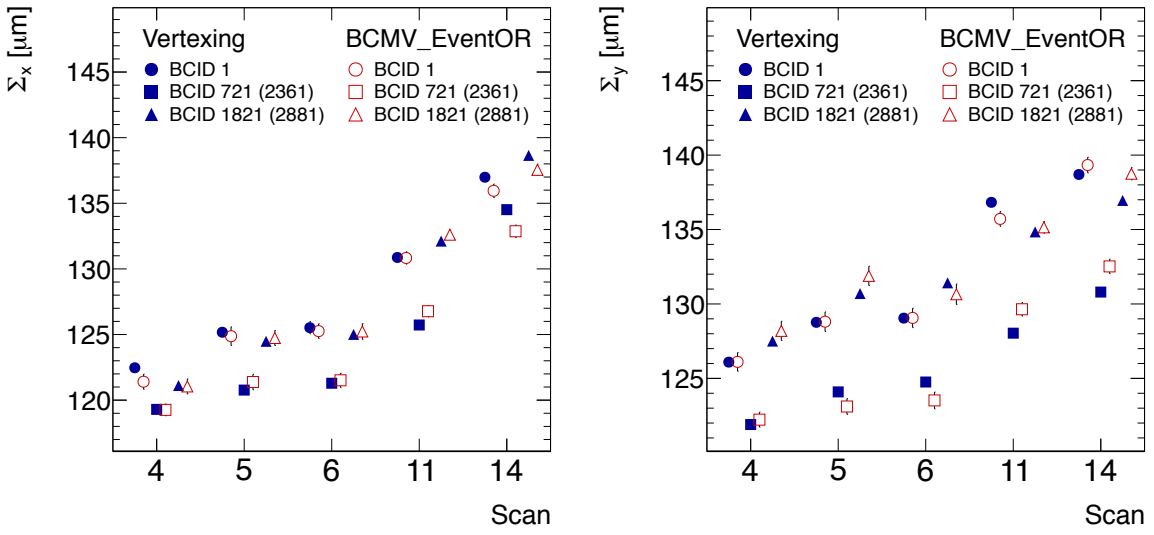

(a) Horizontal scans **(b)** Vertical scans

Figure 8.1.: Convolved bunch sizes Σ_x (Σ_y) measured by vertexing and BCMV_EventOR for the July scans 4, 5 and 6 and for the November scans 11 and 14. The BCID labels in brackets correspond to the November scans, the other ones to the July scans. The errors are statistical only and correspond approximately to the marker size.

and for both beams. In general, this model does not factorise into independent x and y components and hence is suited for studying transverse correlations.

One major advantage of expressing the densities as a sum of two three-dimensional Gaussians is that the integrals in equation (8.1) and (8.2) can be solved analytically even if allowing for a crossing angle between the colliding beams.

The combined fit was carried out for the centred July scans 4, 5 and 6 as well as for the centred November scans 11 and 14. Because of the required computing resources, the centred scans 8, 10 and 15 were not evaluated.

Typical examples on how well the measured scan curves are described by the combined fit are depicted in figure 8.2. The upper plot corresponds to a July VdM scan, the lower one to a November scan. For comparison, also the results of a common VdM fit are shown. Both the combined fits and the VdM fits are good.

In order to check whether the combined fit result is able to describe the beamspot size and position at different beam separations, it proved helpful to define the beamspot position $\langle x \rangle$ along the x axis as

$$\langle x \rangle = \iiint_{-\infty}^{\infty} x \rho_{\mathrm{LR}}(x, y, z) dx dy dz \tag{8.9}$$

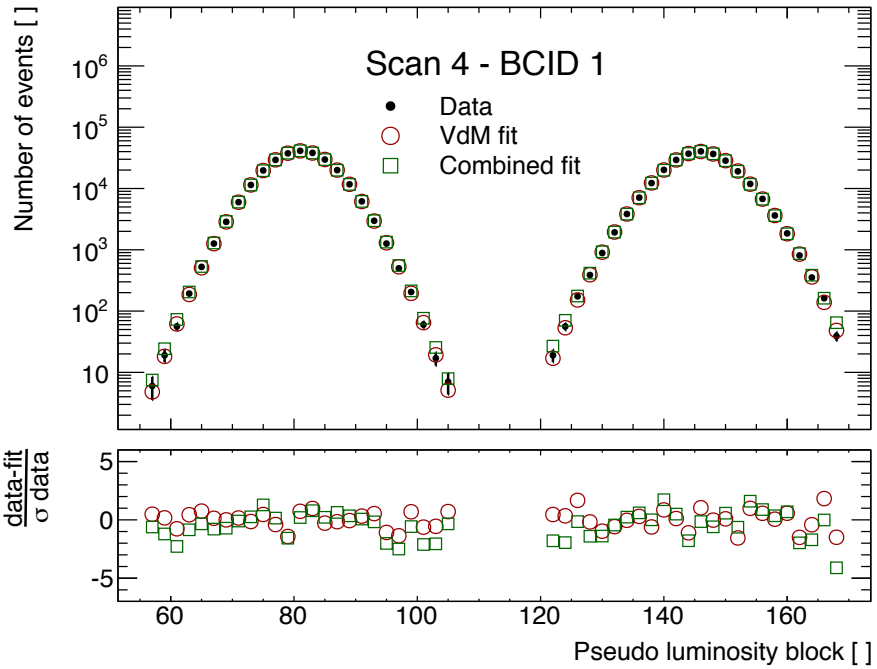

(a) Scan curves of BCID 1 in the July VdM scan 4 measured via vertexing.

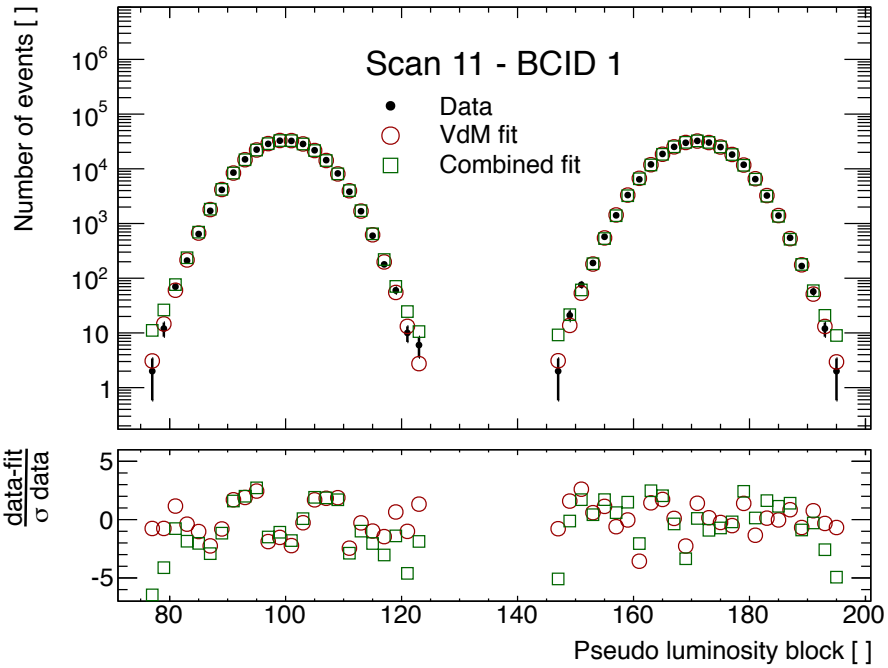

(b) Scan curves of BCID 1 in the November VdM scan 11 measured via vertexing.

Figure 8.2.: Examples for scan curves obtained via vertexing. The upper panels show the measured number of events for different PLBs, i.e. for different beam separations; the left curves correspond to the x scans, the right ones to the y scans. Also shown are the results of the VdM and combined fits. The lower panels show the difference between data and fit, normalised to the statistical error of the data.

and the RMS size σ_x^{LR} along the x axis as

$$\sigma_x^{\mathrm{LR}} = \sqrt{\iiint_{-\infty}^{\infty} (x - \langle x \rangle)^2 \rho_{\mathrm{LR}}(x, y, z) dx dy dz} \tag{8.10}$$

The definitions for $\langle y \rangle$, $\langle z \rangle$, σ_y^{LR} and σ_z^{LR} are analogous.

In order to determine the beamspot position and size expected from the combined fit, the integrals in equation (8.9) and (8.10) are numerically evaluated using the density profiles of the colliding bunches obtained from the combined fit.

The observed beamspot position and size is given by a fit of the luminous region with a three-dimensional Gaussian. The fit corrects for the limited resolution of the reconstructed vertices and is explained in [66]. The mean and width of the Gaussian are taken as the beamspot position and size.

A comparison of the observed ("data") and expected ("fit") beamspot position and size at different beam separations is shown in figure 8.3 for the colliding bunch pair BCID 1 and for July VdM scan 4. While the combined fit models the beamspot features up to a transverse separation of $300\,\mu$m well, the description gets worse beyond this value.

Figure 8.4 shows a comparison of the observed and expected beamspot position and size for the colliding bunch pair BCID 1 and for November VdM scan 11. The transverse beamspot sizes σ_x^{LR} and σ_y^{LR} have a smaller dependency on the beam separation than during the July VdM scans, indicating that the transverse correlations were more pronounced in July than in November. With the exception of σ_x^{LR}, the combined fit describes the features of the luminous region accurately up to a transverse separation of $400\,\mu$m.

Even though demonstrated only for one colliding bunch pair and two scans, the observations for the other scans and bunch pairs are similar: the dependency of the beamspot size on the transverse beam separation is more pronounced in the July than in the November scans. For all examined colliding bunch pairs and scans in July, the combined fit gives a good beamspot description up to a transverse separation of $300\,\mu$m; beyond this value the description gets worse. For all examined colliding bunch pairs and scans in November, the combined fit gives a reasonable beamspot description up to a transverse separation of $300\,\mu$m, however, the variations of the transverse beamspot size at small beam separations are less accurately modelled than for the July scans.

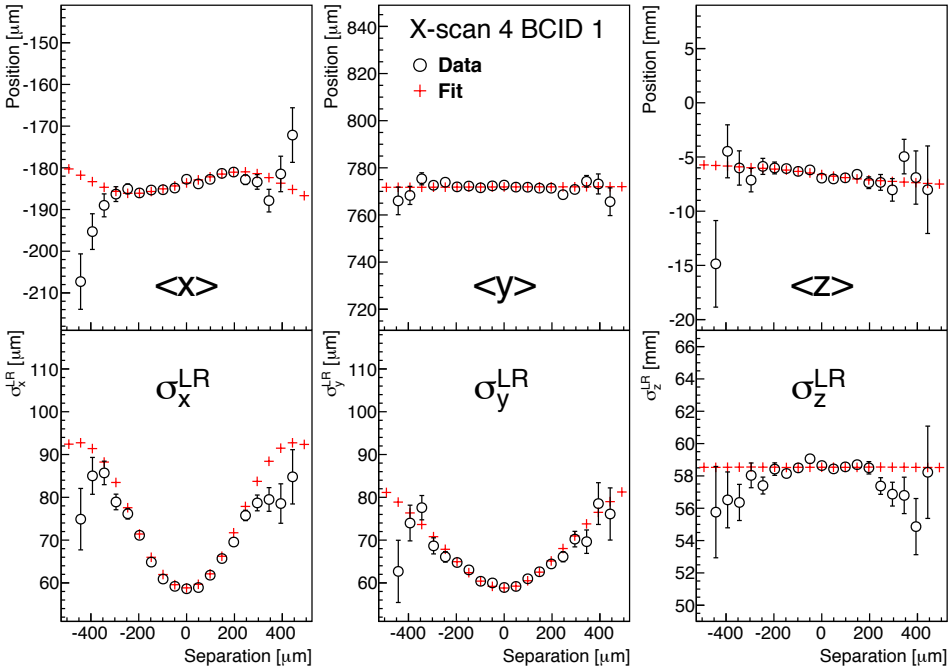

(a) Horizontal scan

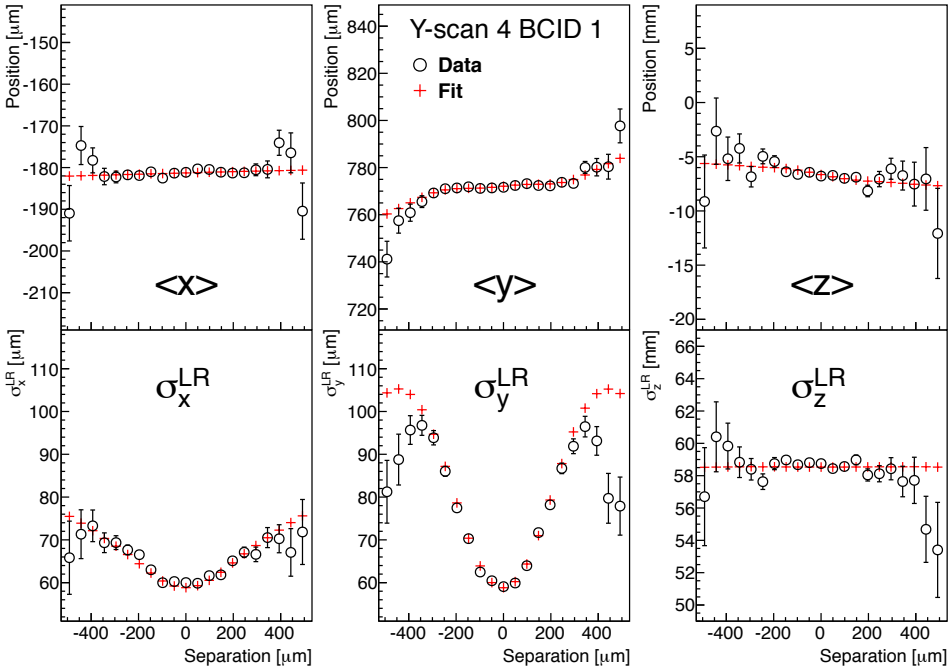

(b) Vertical scan

Figure 8.3.: Beamspot position and size of BCID 1 versus nominal separation during the July VdM scan 4. The black open circles depict the observed beamspot data, the red crosses represent the result of the vertexing based combined fit.

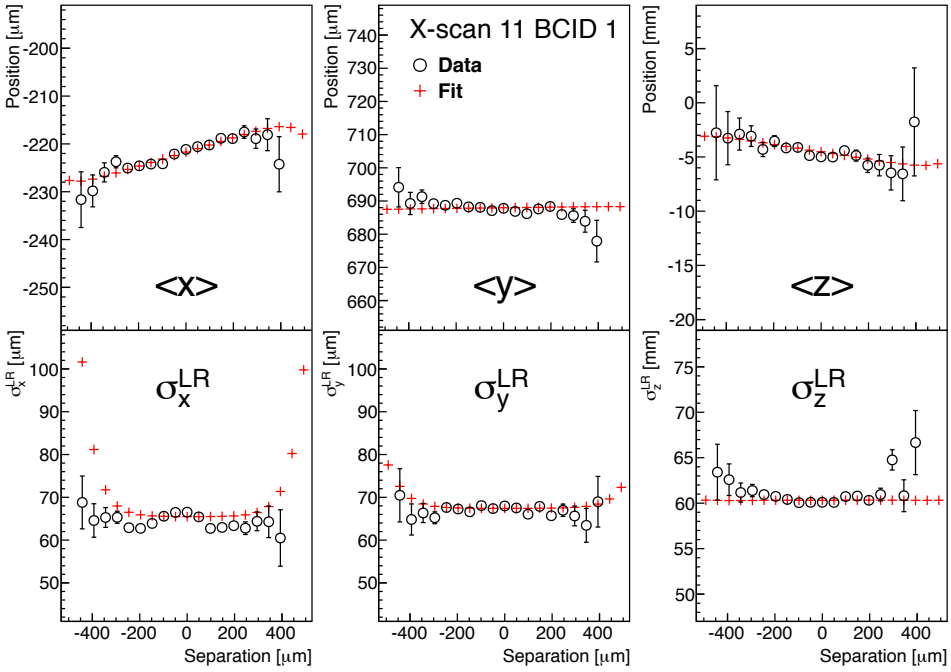

(a) Horizontal scan

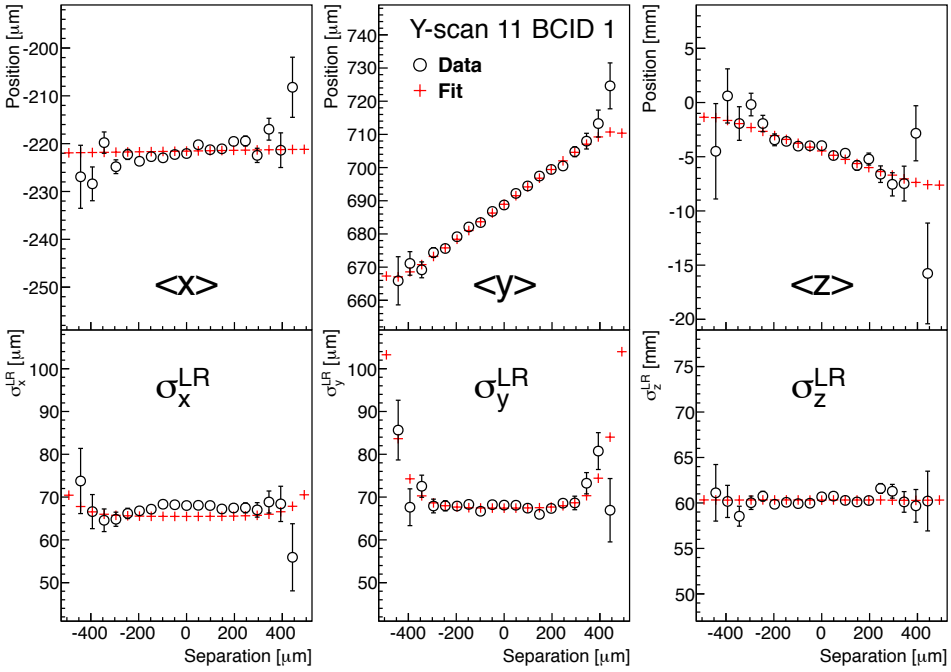

(b) Vertical scan

Figure 8.4.: Beamspot position and size of BCID 1 versus nominal separation during the November VdM scan 11. The black open circles depict the observed beamspot data, the red crosses represent the result of the vertexing based combined fit.

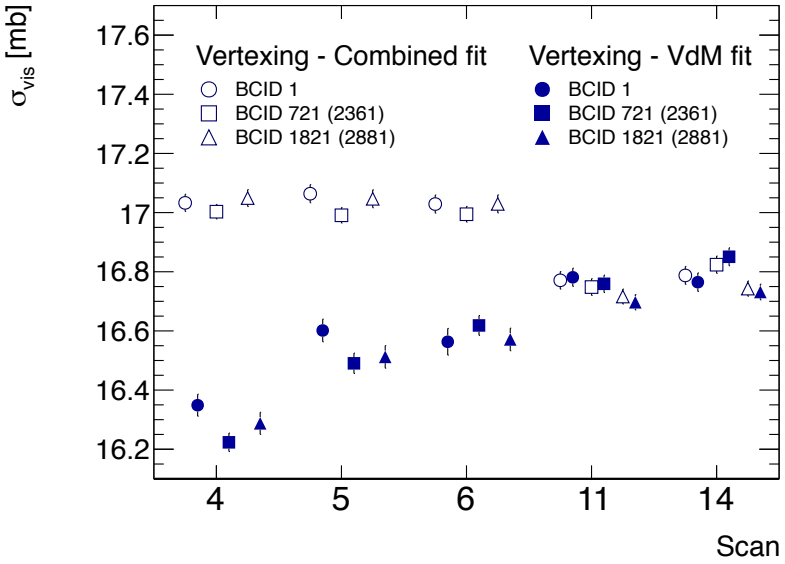

Figure 8.5.: Vertexing σ_{vis} for the July scans 4, 5 and 6 and for the November scans 11 and 14 obtained from the VdM fit and the combined fit. The BCID labels in brackets correspond to the November scans, the other ones to the July scans. The errors are statistical only. Length scale and bunch current corrections are applied.

8.3. Results

Since the combined fit allows transverse correlations and the VdM fit does not, the differences of the visible cross sections obtained with either method are evaluated in this section.

Figure 8.5 depicts the visible cross sections obtained with the VdM and combined fit for all examined colliding bunch pairs and scans. While for the July VdM scans the maximum change of σ_{vis} per colliding bunch pair between either method is 4.9 %, it is 0.2 % for the November scans. For the July scans, the σ_{vis} values obtained with the combined fit not only have a better scan-to-scan consistency than the ones obtained from the VdM fit, they also have a better bunch-to-bunch consistency within a scan. The decrease of the differences between both σ_{vis} values from scan 4 to 6 indicates that the transverse correlations in scan 5 and 6 are smaller than in scan 4.

Although the combined fit σ_{vis} values are current and length scale corrected using the correction factors derived in section 7.1, one observes an overall shift on the order of about 1 % between July and November. The vertexing rates were not corrected for the effect of trigger dead time, but since the dead time was similar for all scan steps and less than 0.5 %, it can not explain the shift. One reason for the shift may be, that the efficiency of the minimum bias trigger, which was used as a trigger for the vertexing,

changed between July and November. Another reason may be that the combined fit overestimates the transverse correlations.

In order to check whether the combined fit is able to describe the transverse correlations well, one can also make use of the offset scans in July and November. If the transverse correlations are modelled well, the observed change of the convolved bunch widths Σ_x and Σ_y in the offset scans with respect to the centred scans, should be predictable with the combined fit result for the centred scans. For this check the offset scan curves are simulated first via numerical integration using the spatial densities of the colliding bunch pairs obtained from the combined fit in the centred scan. Then the simulated scan curves are fitted to determine Σ_x and Σ_y.

The predicted increase of Σ_x for all colliding bunch pairs between centred July scan 6 and offset scan 7 is about 15 %, the predicted increase of Σ_y is approximately 20 %. For both Σ_x and Σ_y, the observed increase is approximately 5 % smaller than the predicted one. The predicted increase of Σ_x and Σ_y between centred November scan 11 and offset scan 13 is about 2 %. For both Σ_x and Σ_y, the observed increase is less than 1 %. Here it was accounted for the fact, that part of the observed increase between centred and offset scans is due to emittance growth.

The maximum change of the visible cross sections obtained from either the VdM or combined fit is used as an uncertainty on the visible cross section obtained through common VdM fits. Since the transverse correlations obtained from the combined fit overestimate the real ones, this is a conservative estimate.

9. Integrated luminosity in 2012

Topic of this chapter is the determination of the integrated luminosity and its uncertainty for the proton-proton collisions at 8 TeV during the year 2012 for ATLAS.

Once a luminosity detector is absolutely calibrated, it can measure the luminosity at all times. The calibration constants σ_{vis} and their uncertainties are determined based on VdM scans. As shown in section 7.4, the most precise calibration in 2012 was achieved for the November VdM scans. Therefore, the November VdM scans are chosen as the basis for the determination of the integrated luminosity.

However, one must consider two effects when determining the luminosity at times different from the times of the VdM scans: the long-term stability of the detector response and the change of running conditions between physics and VdM scan fills.

The long-term stability of the detector response is assessed via the time evolution of ratios between different luminosity measurements. Equivalently, one can compare the ratios of the mean number of interactions per BC as done in figure 9.1. This type of uncertainty assessment is based on the assumption, that it is very unlikely that all algorithms or detectors deviate from linearity in the same way. All detectors found on figure 9.1 are introduced in section 3.3.

The luminosity ratios are plotted with respect to BCMV_EventOR. The BCM and LUCID algorithms are mutually consistent throughout the full year, indicating a stable detector response of BCM and LUCID. However, the luminosity measurements of FCal, Tile and Medipix are also mutually consistent, but seem to drift with respect to the ones of BCM and LUCID. At the time of writing, it is not clear yet, which detectors are drifting and which are stable. Accounting for the drift between the different luminosity measurements, an uncertainty of 2 % is assigned to the long-term stability.

Figure 9.1 contains a step correction to the BCMV_EventOR data taken before LHC fill 3228. This fill took place on October 27, 2012, and also marks the beginning of an increased noise level in the BCMV_EventOR measurements. By comparing the luminosity ratios between different detectors shortly before and after the start of the noise period, it became clear, that the detection efficiency of the BCMV_EventOR algorithm changed by $-0.52\,\%$ at that time. Since the central σ_{vis} is given by the November VdM

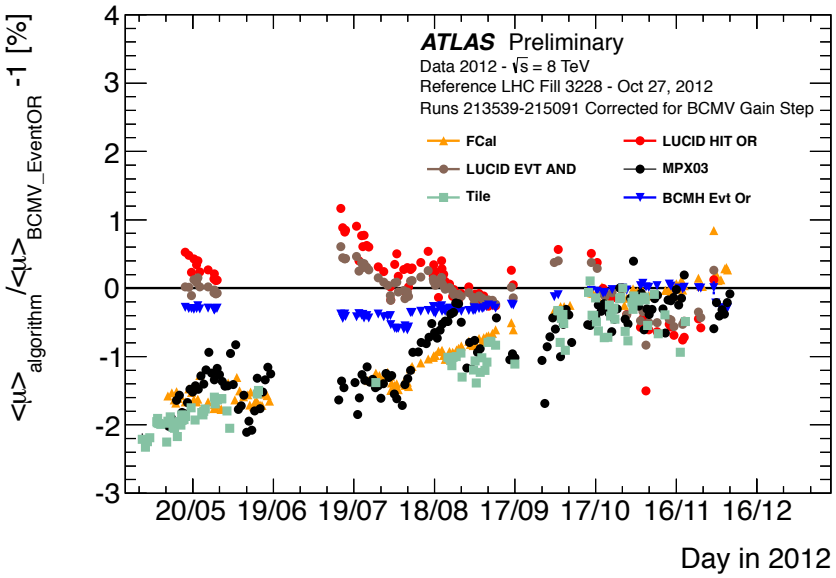

Figure 9.1.: Comparison of the bunch-averaged mean number of interactions versus time measured by various luminosity algorithms, or detectors, with respect to BCMV_EventOR. Each data point corresponds to a different LHC fill. The ratios are shifted to zero at the time of reference fill 3228, which took place on October 27, 2012. Statistical errors are shown, but negligible [67].

scans and hence determined during the noise period, it is scaled up by +0.52 % when converting EventOR rates to luminosity for fills before the noise period.

Via the monitoring of luminosity ratios, it was furthermore detected, that the efficiency of BCMH_EventOR decreased by 0.40 % at the time of the November VdM scans. After the scans, the efficiency went back to normal. Thus, the σ_{vis} for BCMH_EventOR is scaled up by 0.40 % for fills different from the November VdM scan fills. The maximum change of the BCM calibration constants due to the above mentioned efficiency changes, i.e. 0.5 %, is assigned to an uncertainty labelled BCM calibration drift.

The luminosity weighted distribution of the mean number of interactions per BC for the collisions recorded by ATLAS in 2012 is illustrated in figure 9.2. On average, μ is 21, but it can get as small as 5 or as large as 40. By comparison, the maximum μ during the November VdM scans is approximately 0.5.

To assess a possible non-linear response of a luminosity detector or algorithm, a procedure similar to the one for the long-term stability is chosen. In normal LHC physics conditions, the beams are stepwise separated in order to provide collisions over a wide range of μ, also known as μ-scan. The study is done in a dedicated fill, in order to be able to separate the μ-dependence from the long-term stability. The internal consistency of different luminosity measurements as a function of μ allows to assign an uncertainty

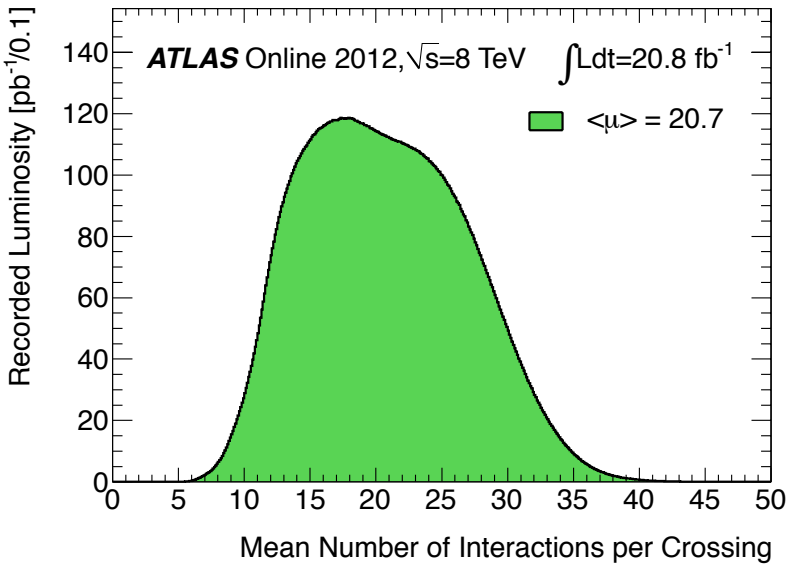

Figure 9.2.: Distribution of the mean number of interactions per BC μ weighted by luminosity. The data corresponds to proton-proton collisions at $\sqrt{s} = 8\,\text{TeV}$ recorded by ATLAS before November 26, 2012. μ is calculated based on equation (5.1), where σ_{inel} is taken as 73 mb [67].

to the μ-dependence of the luminosity. The observed internal consistency of the various luminosity measurements during the μ-scan is 0.6 %. Hence this value is assigned to the μ-dependence uncertainty.

Another effect which needs to be accounted for is afterglow. Its impact on the VdM scans is negligible, because of the large bunch spacing in VdM scan fills. However, standard physics operation involves bunch trains and therefore the luminosity measurements must be corrected for afterglow activity. The luminosity correction procedure for a colliding bunch pair is based on the Poisson probability to observe an event combined with the measured event rate for the immediately preceding BC. The correction and its uncertainty is documented in [17]. Accordingly, an uncertainty of 0.2 % is assigned to the afterglow subtraction.

In order to calculate the total uncertainty, the different uncertainty contributions listed in table 9.1 are added in quadrature. All in all, the total uncertainty on the integrated luminosity amounts to 3.30 %.

The central calibration constants are given by the simple average of the visible cross sections obtained for the November VdM scans 11, 14 and 15. These are listed in table 7.8. Additionally, BCMV_EventOR is corrected for the efficiency drop during the noise period and BCMH_EventOR for the efficiency drop at the time of the November VdM scans. In summary, the central σ_{vis} value for the algorithms BCMV_EventOR

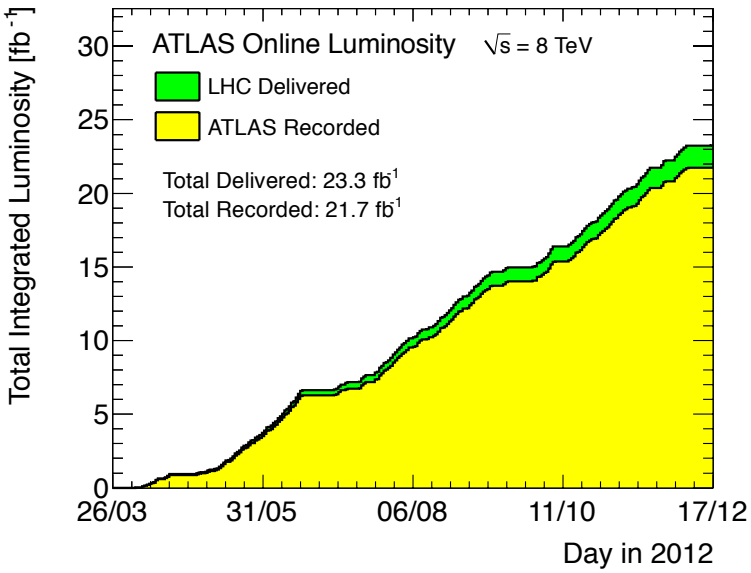

Figure 9.3.: Integrated luminosity versus day in 2012 for proton-proton collisions at $\sqrt{s} = 8\,\text{TeV}$ in ATLAS. The delivered and recorded luminosity correspond to the definitions in section 3.3 [67].

and BCMH_EventOR are 4.937 mb and 4.976 mb, respectively. LUCID_EventOR has a central σ_{vis} value of 34.71 mb.

Figure 9.3 illustrates the integrated ATLAS luminosity versus day in 2012. The difference between the delivered and recorded luminosity is due to inefficiencies in the recording of the collision data.

	Uncertainty on integrated luminosity [%]
Subtotal, uncertainty on σ_{vis}	2.50
Long-term stability	2.00
BCM calibration drift	0.50
μ-dependence during physics running	0.60
Afterglow subtraction	0.20
Subtotal, luminosity monitoring	2.16
Total	3.30

Table 9.1.: Uncertainty on the integrated luminosity in 2012 for proton-proton collisions at $\sqrt{s} = 8\,\text{TeV}$ in ATLAS.

10. Summary and outlook

In the year 2012, the ATLAS detector at the LHC recorded proton-proton collisions at center of mass energies of up to 8 TeV. The relative luminosity is measured with various detectors and algorithms. In this thesis, three luminosity algorithms linked to the two main luminosity detectors are calibrated in an absolute way: BCMH_EventOR, BCMV_EventOR and LUCID_EventOR. The determination of the calibration constants is based on Van der Meer (VdM) scans. In 2012 three calibration campaigns took place: one in April, July and November. In this thesis, the July and November VdM scans are evaluated.

The overall uncertainty on the calibration constants obtained from the July VdM scans is 5.40 %. It is dominated by a 4.90 % uncertainty caused by "transverse correlations". This uncertainty contribution accounts for the violation of one fundamental assumption of the scans which is the factorisation of the transverse particle densities of the colliding bunches into independent horizontal and vertical components. The second largest uncertainty contribution is 1.80 % and originates from the mutual deflection of the beams during the scans. The overall uncertainty on the calibration constants obtained from the November VdM scans is 2.50 %. It is dominated by a 1.80 % uncertainty associated with the mutual deflection of the beams. Compared to the July scans, the uncertainty due to transverse correlations in November is 0.20 % and thus negligible.

Intermediate results of the VdM scan analysis unveiled significant drifts of the beam orbits during some of the scans, degrading the accuracy of the calibration constants. To correct for the impact of orbit drifts, correction formulae were developed and incorporated into the analysis.

The decrease of the transverse correlations in November compared to July is attributed to a dedicated machine development study which targeted the LHC injector chain for improvements and took place at the beginning of November.

Since the November calibration constants are more precise than the July ones, the former are used to determine the integrated luminosity for ATLAS in 2012. In order to account for possible variations of the calibration constants over time or under different conditions, an uncertainty labelled "luminosity monitoring" is introduced. This uncer-

tainty is 2.16 % and dominated by the long-term stability of the calibration constants. The latter amounts to 2.00 % and is given by a drift of the luminosity ratios between the calorimeters, BCM and LUCID. Combining the uncertainties related to the calibration procedure and the luminosity monitoring, the overall uncertainty on the integrated luminosity in 2012 is 3.30 %.

The calibration constants derived in this thesis are used to determine the preliminary official ATLAS luminosity. Furthermore this thesis makes a significant contribution to the estimation of the uncertainties originating from the bunch currents, the drifts of the beam orbits, the scan curve fit model, transverse correlations, and the choice of the reference specific luminosity. Other uncertainties were estimated in dedicated studies carried out by others.

To quantify the bias on the common VdM fit due to transverse correlations, a combined fit was applied to the interaction vertices reconstructed during the scans. This type of fit is partially complementary to the common VdM fit and is based on the rate of reconstructed vertices as well as on the shape of the luminous region. The combined fit relies on a model of the particle densities of the colliding bunches. The model chosen in this thesis overestimates the transverse correlations. If a model is found which better describes the correlations, this may eventually allow to correct the calibration constants obtained from the VdM fit for transverse correlations, and the precision of the July VdM scans would become compatible with the one of the November scans.

Only recently, it was discovered that the beam-beam deflection during VdM scans is non-negligible. Since the time scale was too short to carry out a detailed study, a conservative uncertainty estimation was done. When precise and reliable simulations of beam-beam effects in VdM scans become available, the calibration constants can be corrected for the beam-beam deflection, hence reducing the uncertainty. Furthermore, if it can be found which luminosity detectors are stable over time and which are drifting, an uncertainty on the integrated luminosity of less than 2 % is within reach.

It is anticipated that VdM scans will continue to play an important role for luminosity measurements at the LHC. Due to detector upgrades, the vertexing capabilities will improve over the coming years both in terms of resolution and reconstruction rate, thus it is expected that vertexing based studies of the luminous region during VdM scans will become an increasingly important ingredient of the VdM scan evaluation.

A. Derivation of EventOR probability

$$P_{\text{EventOR}} = \sum_{n=1}^{\infty} \epsilon_n \cdot P(n, \mu) \tag{A.1}$$

$$= \sum_{n=1}^{\infty} (1 - (1-\epsilon)^n) \cdot \frac{\mu^n e^{-\mu}}{n!} \tag{A.2}$$

$$= \sum_{n=1}^{\infty} \frac{\mu^n e^{-\mu}}{n!} - \sum_{n=1}^{\infty} (1-\epsilon)^n \cdot \frac{\mu^n e^{-\mu}}{n!} \tag{A.3}$$

$$= \sum_{n=0}^{\infty} \frac{\mu^n e^{-\mu}}{n!} - e^{-\mu} - \sum_{n=0}^{\infty} (1-\epsilon)^n \cdot \frac{\mu^n e^{-\mu}}{n!} + e^{-\mu} \tag{A.4}$$

$$= e^{-\mu} \sum_{n=0}^{\infty} \frac{\mu^n}{n!} - e^{-\mu} \sum_{n=0}^{\infty} \frac{[(1-\epsilon)\mu]^n}{n!} \tag{A.5}$$

Using the Taylor series of the exponential function

$$e^x = \sum_{n=0}^{\infty} \frac{x^n}{n!} \tag{A.6}$$

one can simplify the equation and obtains:

$$P_{\text{EventOR}} = e^{-\mu} e^{\mu} - e^{-\mu} e^{(1-\epsilon)\mu} \tag{A.7}$$

$$= 1 - e^{-\epsilon\mu} \tag{A.8}$$

B. Bunch-by-bunch σ_{vis} in the July and November 2012 VdM scans

BCMV_EventOR - σ_{vis} in July VdM scans

BCID	σ_{vis} [mb]			
	Scan 4	Scan 5	Scan 6	Scan 8
1	4.847 ± 0.021	4.956 ± 0.024	4.940 ± 0.022	4.825 ± 0.027
41	4.869 ± 0.018	4.977 ± 0.020	4.959 ± 0.020	4.907 ± 0.028
81	4.893 ± 0.021	4.939 ± 0.022	4.966 ± 0.023	4.895 ± 0.028
121	4.886 ± 0.024	4.938 ± 0.026	4.962 ± 0.026	4.825 ± 0.026
161	4.901 ± 0.021	4.952 ± 0.022	4.929 ± 0.022	4.780 ± 0.026
201	4.885 ± 0.021	4.997 ± 0.023	4.963 ± 0.022	4.833 ± 0.027
241	4.846 ± 0.020	4.953 ± 0.021	4.964 ± 0.021	4.814 ± 0.031
721	4.841 ± 0.017	4.911 ± 0.020	4.932 ± 0.020	4.861 ± 0.025
761	4.882 ± 0.025	4.963 ± 0.026	4.948 ± 0.026	4.838 ± 0.028
801	4.828 ± 0.020	4.940 ± 0.021	4.967 ± 0.021	4.822 ± 0.029
841	4.840 ± 0.022	4.911 ± 0.023	4.945 ± 0.023	4.860 ± 0.028
881	4.900 ± 0.021	4.968 ± 0.022	4.939 ± 0.022	4.851 ± 0.027
921	4.861 ± 0.021	4.962 ± 0.023	4.984 ± 0.024	4.844 ± 0.027
961	4.889 ± 0.020	4.941 ± 0.022	5.013 ± 0.022	4.873 ± 0.029
1581	4.877 ± 0.021	4.929 ± 0.023	4.972 ± 0.024	4.831 ± 0.031
1621	4.846 ± 0.018	4.965 ± 0.019	4.908 ± 0.019	4.828 ± 0.028
1661	4.896 ± 0.024	4.952 ± 0.026	4.948 ± 0.027	4.894 ± 0.026
1701	4.861 ± 0.019	4.905 ± 0.021	4.947 ± 0.021	4.883 ± 0.029
1741	4.861 ± 0.023	4.905 ± 0.023	4.972 ± 0.024	4.823 ± 0.030
1781	4.881 ± 0.021	4.949 ± 0.027	4.902 ± 0.024	4.860 ± 0.027
1821	4.876 ± 0.021	4.974 ± 0.022	4.955 ± 0.023	4.824 ± 0.031
2161	4.835 ± 0.019	4.911 ± 0.020	4.931 ± 0.021	4.869 ± 0.026
2201	4.845 ± 0.021	4.956 ± 0.022	4.956 ± 0.023	4.871 ± 0.029
2241	4.901 ± 0.021	4.884 ± 0.022	4.910 ± 0.023	4.872 ± 0.030
2281	4.857 ± 0.023	4.924 ± 0.025	4.946 ± 0.024	4.866 ± 0.028
2321	4.879 ± 0.019	4.903 ± 0.021	4.964 ± 0.021	4.855 ± 0.026
2361	4.848 ± 0.022	4.937 ± 0.024	4.982 ± 0.025	4.845 ± 0.030
2401	4.875 ± 0.022	4.965 ± 0.023	4.892 ± 0.025	4.845 ± 0.028
2881	4.872 ± 0.022	4.950 ± 0.023	4.943 ± 0.023	4.906 ± 0.026
2921	4.919 ± 0.022	4.970 ± 0.024	4.994 ± 0.024	4.895 ± 0.028
2961	4.917 ± 0.021	4.991 ± 0.022	4.960 ± 0.023	4.867 ± 0.025
3001	4.873 ± 0.021	4.979 ± 0.021	5.008 ± 0.022	4.850 ± 0.026
3041	4.870 ± 0.020	4.957 ± 0.022	4.947 ± 0.022	4.851 ± 0.026
3081	4.864 ± 0.020	5.000 ± 0.022	5.018 ± 0.020	4.852 ± 0.026
3121	4.867 ± 0.020	4.986 ± 0.022	5.008 ± 0.023	4.863 ± 0.027

Table B.1.: Bunch-by-bunch σ_{vis} for BCMV_EventOR obtained in the four centred July 2012 VdM scans. The errors are statistical only. Length scale and bunch current corrections are applied.

BCMH_EventOR - σ_{vis} in July VdM scans

BCID	σ_{vis} [mb]			
	Scan 4	Scan 5	Scan 6	Scan 8
1	4.831 ± 0.021	4.955 ± 0.022	4.926 ± 0.022	4.854 ± 0.027
41	4.858 ± 0.018	4.942 ± 0.019	4.946 ± 0.020	4.859 ± 0.028
81	4.903 ± 0.021	4.956 ± 0.022	4.939 ± 0.023	4.808 ± 0.028
121	4.774 ± 0.024	4.926 ± 0.025	4.946 ± 0.025	4.858 ± 0.027
161	4.895 ± 0.020	4.948 ± 0.022	4.929 ± 0.022	4.843 ± 0.026
201	4.861 ± 0.020	4.914 ± 0.022	4.929 ± 0.022	4.855 ± 0.028
241	4.835 ± 0.019	4.910 ± 0.021	4.983 ± 0.023	4.853 ± 0.030
721	4.828 ± 0.018	4.894 ± 0.018	4.902 ± 0.019	4.841 ± 0.025
761	4.875 ± 0.025	4.898 ± 0.026	4.912 ± 0.027	4.773 ± 0.028
801	4.831 ± 0.019	4.984 ± 0.021	4.939 ± 0.020	4.839 ± 0.028
841	4.826 ± 0.022	4.927 ± 0.023	4.943 ± 0.023	4.839 ± 0.028
881	4.852 ± 0.021	4.910 ± 0.022	4.949 ± 0.023	4.840 ± 0.027
921	4.842 ± 0.021	4.918 ± 0.023	4.967 ± 0.024	4.813 ± 0.027
961	4.863 ± 0.020	4.929 ± 0.022	4.984 ± 0.023	4.821 ± 0.028
1581	4.823 ± 0.021	4.893 ± 0.024	4.964 ± 0.024	4.809 ± 0.031
1621	4.844 ± 0.018	4.924 ± 0.019	4.933 ± 0.019	4.789 ± 0.027
1661	4.850 ± 0.023	4.971 ± 0.025	4.947 ± 0.027	4.830 ± 0.028
1701	4.841 ± 0.018	4.943 ± 0.020	4.948 ± 0.020	4.807 ± 0.028
1741	4.927 ± 0.022	4.964 ± 0.023	5.017 ± 0.025	4.835 ± 0.029
1781	4.806 ± 0.021	4.942 ± 0.023	4.934 ± 0.025	4.849 ± 0.027
1821	4.850 ± 0.021	4.897 ± 0.022	4.923 ± 0.022	4.794 ± 0.031
2161	4.829 ± 0.019	4.926 ± 0.020	4.919 ± 0.020	4.838 ± 0.025
2201	4.800 ± 0.021	4.899 ± 0.024	4.910 ± 0.023	4.870 ± 0.028
2241	4.837 ± 0.021	4.893 ± 0.023	4.912 ± 0.023	4.868 ± 0.029
2281	4.813 ± 0.022	4.877 ± 0.024	4.947 ± 0.024	4.824 ± 0.029
2321	4.821 ± 0.019	4.939 ± 0.021	4.923 ± 0.020	4.824 ± 0.027
2361	4.835 ± 0.021	4.927 ± 0.024	4.970 ± 0.027	4.794 ± 0.031
2401	4.818 ± 0.022	4.920 ± 0.024	4.929 ± 0.025	4.811 ± 0.029
2881	4.864 ± 0.021	4.955 ± 0.022	4.957 ± 0.022	4.905 ± 0.025
2921	4.869 ± 0.023	4.996 ± 0.024	4.905 ± 0.024	4.860 ± 0.027
2961	4.854 ± 0.022	4.944 ± 0.022	4.921 ± 0.023	4.853 ± 0.024
3001	4.851 ± 0.020	4.958 ± 0.022	4.949 ± 0.021	4.850 ± 0.027
3041	4.838 ± 0.021	4.928 ± 0.022	4.906 ± 0.023	4.840 ± 0.028
3081	4.845 ± 0.019	4.946 ± 0.021	4.974 ± 0.021	4.851 ± 0.027
3121	4.824 ± 0.020	4.959 ± 0.022	4.943 ± 0.022	4.845 ± 0.027

Table B.2.: Bunch-by-bunch σ_{vis} for BCMH_EventOR obtained in the four centred July 2012 VdM scans. The errors are statistical only. Length scale and bunch current corrections are applied.

LUCID_EventOR - σ_{vis} in July VdM scans

BCID	σ_{vis} [mb]			
	Scan 4	Scan 5	Scan 6	Scan 8
1	34.424 ± 0.058	34.971 ± 0.061	34.972 ± 0.060	34.350 ± 0.074
41	34.432 ± 0.052	35.115 ± 0.055	35.198 ± 0.056	34.347 ± 0.076
81	34.528 ± 0.059	35.069 ± 0.061	35.023 ± 0.061	34.209 ± 0.075
121	34.320 ± 0.065	34.871 ± 0.068	35.185 ± 0.067	34.186 ± 0.073
161	34.523 ± 0.056	35.028 ± 0.060	35.045 ± 0.059	34.356 ± 0.070
201	34.490 ± 0.057	35.120 ± 0.060	35.248 ± 0.061	34.351 ± 0.074
241	34.249 ± 0.054	34.955 ± 0.058	35.195 ± 0.059	34.418 ± 0.081
721	34.234 ± 0.050	34.855 ± 0.053	34.986 ± 0.054	34.298 ± 0.070
761	34.432 ± 0.067	34.994 ± 0.069	34.889 ± 0.070	34.267 ± 0.075
801	34.286 ± 0.054	35.044 ± 0.057	35.065 ± 0.058	34.417 ± 0.078
841	34.442 ± 0.060	34.945 ± 0.063	35.112 ± 0.063	34.387 ± 0.077
881	34.532 ± 0.058	34.976 ± 0.062	34.994 ± 0.061	34.218 ± 0.077
921	34.356 ± 0.059	35.003 ± 0.063	35.129 ± 0.064	34.251 ± 0.073
961	34.478 ± 0.057	35.140 ± 0.059	35.190 ± 0.060	34.293 ± 0.076
1581	34.352 ± 0.059	34.817 ± 0.063	35.176 ± 0.064	34.395 ± 0.082
1621	34.223 ± 0.051	34.922 ± 0.054	34.858 ± 0.054	34.282 ± 0.072
1661	34.601 ± 0.065	35.235 ± 0.068	35.204 ± 0.069	34.337 ± 0.073
1701	34.359 ± 0.054	34.961 ± 0.057	35.043 ± 0.057	34.361 ± 0.075
1741	34.657 ± 0.061	35.008 ± 0.063	35.191 ± 0.063	34.409 ± 0.082
1781	34.177 ± 0.060	34.943 ± 0.063	34.956 ± 0.066	34.460 ± 0.073
1821	34.429 ± 0.059	34.966 ± 0.062	34.967 ± 0.062	34.201 ± 0.085
2161	34.374 ± 0.053	34.897 ± 0.057	34.830 ± 0.057	34.332 ± 0.071
2201	34.215 ± 0.059	34.953 ± 0.063	35.064 ± 0.063	34.251 ± 0.078
2241	34.370 ± 0.059	34.910 ± 0.062	34.977 ± 0.063	34.389 ± 0.079
2281	34.369 ± 0.060	34.900 ± 0.067	34.976 ± 0.067	34.371 ± 0.078
2321	34.401 ± 0.054	34.891 ± 0.058	35.039 ± 0.055	34.466 ± 0.074
2361	34.354 ± 0.060	34.994 ± 0.064	35.143 ± 0.066	34.216 ± 0.082
2401	34.474 ± 0.062	34.892 ± 0.063	35.059 ± 0.066	34.324 ± 0.079
2881	34.498 ± 0.060	35.109 ± 0.063	35.075 ± 0.063	34.455 ± 0.069
2921	34.625 ± 0.061	35.165 ± 0.064	35.127 ± 0.064	34.554 ± 0.075
2961	34.470 ± 0.060	34.909 ± 0.063	34.985 ± 0.063	34.357 ± 0.070
3001	34.638 ± 0.057	35.228 ± 0.059	35.315 ± 0.060	34.373 ± 0.074
3041	34.430 ± 0.058	35.030 ± 0.061	35.071 ± 0.059	34.329 ± 0.075
3081	34.499 ± 0.055	35.040 ± 0.059	35.116 ± 0.059	34.357 ± 0.073
3121	34.454 ± 0.058	35.178 ± 0.060	35.094 ± 0.060	34.540 ± 0.074

Table B.3.: Bunch-by-bunch σ_{vis} for LUCID_EventOR obtained in the four centred July 2012 VdM scans. The errors are statistical only. Length scale and bunch current corrections are applied.

BCMV_EventOR - σ_{vis} in November VdM scans

BCID	σ_{vis} [mb]			
	Scan 10	Scan 11	Scan 14	Scan 15
1	4.879 ± 0.020	4.917 ± 0.021	4.917 ± 0.022	4.960 ± 0.021
41	4.882 ± 0.018	4.946 ± 0.019	4.938 ± 0.020	4.965 ± 0.020
81	4.897 ± 0.019	4.923 ± 0.019	4.992 ± 0.020	4.917 ± 0.019
121	4.872 ± 0.017	4.884 ± 0.017	4.929 ± 0.018	4.924 ± 0.019
161	4.881 ± 0.018	4.902 ± 0.019	4.928 ± 0.020	4.914 ± 0.021
201	4.911 ± 0.018	4.893 ± 0.019	4.911 ± 0.020	4.901 ± 0.019
241	4.861 ± 0.020	4.898 ± 0.021	4.905 ± 0.022	4.936 ± 0.019
721	4.862 ± 0.019	4.928 ± 0.020	4.896 ± 0.021	4.895 ± 0.019
761	4.914 ± 0.017	4.894 ± 0.017	4.926 ± 0.019	4.951 ± 0.020
801	4.934 ± 0.018	4.865 ± 0.018	4.908 ± 0.019	4.947 ± 0.020
841	4.882 ± 0.015	4.901 ± 0.016	4.904 ± 0.016	4.928 ± 0.019
881	4.917 ± 0.018	4.933 ± 0.018	4.892 ± 0.019	4.911 ± 0.019
921	4.913 ± 0.019	4.915 ± 0.019	4.930 ± 0.021	4.940 ± 0.019
961	4.918 ± 0.018	4.880 ± 0.019	4.890 ± 0.020	4.927 ± 0.019
1581	4.858 ± 0.018	4.889 ± 0.019	4.897 ± 0.020	4.937 ± 0.020
1621	4.901 ± 0.018	4.867 ± 0.018	4.928 ± 0.019	4.922 ± 0.019
1661	4.891 ± 0.019	4.890 ± 0.020	4.921 ± 0.021	4.869 ± 0.020
1701	4.881 ± 0.018	4.881 ± 0.018	4.888 ± 0.019	4.924 ± 0.019
1741	4.864 ± 0.021	4.927 ± 0.022	4.874 ± 0.023	4.915 ± 0.021
1781	4.861 ± 0.017	4.879 ± 0.018	4.888 ± 0.019	4.914 ± 0.020
1821	4.906 ± 0.017	4.916 ± 0.017	4.937 ± 0.018	4.916 ± 0.021
2161	4.939 ± 0.019	4.926 ± 0.020	4.945 ± 0.021	4.894 ± 0.019
2201	4.912 ± 0.018	4.928 ± 0.018	4.915 ± 0.019	4.902 ± 0.020
2241	4.867 ± 0.021	4.904 ± 0.021	4.953 ± 0.023	4.910 ± 0.021
2281	4.877 ± 0.016	4.905 ± 0.017	4.917 ± 0.018	4.917 ± 0.018
2321	4.866 ± 0.017	4.907 ± 0.018	4.927 ± 0.019	4.908 ± 0.019
2361	4.867 ± 0.019	4.889 ± 0.019	4.889 ± 0.021	4.909 ± 0.018
2401	4.838 ± 0.020	4.893 ± 0.021	4.876 ± 0.022	4.862 ± 0.021
2881	4.902 ± 0.016	4.905 ± 0.017	4.930 ± 0.018	4.890 ± 0.019

Table B.4.: Bunch-by-bunch σ_{vis} for BCMV_EventOR obtained in the four centred November 2012 VdM scans. The errors are statistical only. Length scale and bunch current corrections are applied.

BCMH_EventOR - σ_{vis} in November VdM scans

BCID	σ_{vis} [mb]			
	Scan 10	Scan 11	Scan 14	Scan 15
1	4.925 ± 0.019	4.953 ± 0.020	4.945 ± 0.021	4.973 ± 0.020
41	4.895 ± 0.017	5.000 ± 0.018	4.976 ± 0.018	4.973 ± 0.019
81	4.882 ± 0.017	4.974 ± 0.018	4.988 ± 0.019	4.962 ± 0.018
121	4.920 ± 0.016	4.955 ± 0.016	4.965 ± 0.017	4.988 ± 0.018
161	4.898 ± 0.017	4.918 ± 0.018	4.950 ± 0.019	4.975 ± 0.019
201	4.907 ± 0.017	4.948 ± 0.018	4.941 ± 0.018	4.944 ± 0.018
241	4.863 ± 0.019	4.955 ± 0.020	4.964 ± 0.020	4.989 ± 0.018
721	4.912 ± 0.018	4.922 ± 0.019	4.983 ± 0.020	4.938 ± 0.018
761	4.965 ± 0.016	4.936 ± 0.017	4.956 ± 0.017	4.958 ± 0.019
801	4.949 ± 0.017	4.933 ± 0.017	4.976 ± 0.018	4.950 ± 0.018
841	4.895 ± 0.014	4.989 ± 0.015	4.969 ± 0.016	4.939 ± 0.018
881	4.909 ± 0.017	4.921 ± 0.017	4.966 ± 0.018	4.954 ± 0.018
921	4.927 ± 0.018	4.946 ± 0.018	4.963 ± 0.019	4.929 ± 0.018
961	4.931 ± 0.017	4.943 ± 0.018	4.962 ± 0.018	4.959 ± 0.018
1581	4.866 ± 0.017	4.918 ± 0.018	4.948 ± 0.019	4.974 ± 0.019
1621	4.901 ± 0.017	4.907 ± 0.017	4.958 ± 0.018	5.003 ± 0.018
1661	4.925 ± 0.018	4.967 ± 0.018	5.009 ± 0.019	4.968 ± 0.019
1701	4.906 ± 0.017	4.929 ± 0.017	4.948 ± 0.018	4.963 ± 0.018
1741	4.936 ± 0.020	4.944 ± 0.020	4.930 ± 0.021	4.925 ± 0.019
1781	4.884 ± 0.016	4.938 ± 0.017	5.004 ± 0.018	4.960 ± 0.019
1821	4.932 ± 0.016	4.937 ± 0.016	4.972 ± 0.017	4.934 ± 0.020
2161	4.947 ± 0.018	4.978 ± 0.019	4.970 ± 0.020	4.956 ± 0.018
2201	4.910 ± 0.017	4.936 ± 0.017	4.987 ± 0.018	4.959 ± 0.019
2241	4.898 ± 0.019	4.953 ± 0.020	4.954 ± 0.021	4.931 ± 0.020
2281	4.887 ± 0.016	4.954 ± 0.016	4.943 ± 0.017	4.967 ± 0.017
2321	4.962 ± 0.017	4.971 ± 0.017	4.972 ± 0.018	4.971 ± 0.018
2361	4.924 ± 0.018	4.927 ± 0.018	4.976 ± 0.019	4.932 ± 0.017
2401	4.939 ± 0.019	4.933 ± 0.019	4.933 ± 0.020	4.951 ± 0.020
2881	4.930 ± 0.016	4.956 ± 0.016	4.984 ± 0.017	4.941 ± 0.018

Table B.5.: Bunch-by-bunch σ_{vis} for BCMH_EventOR obtained in the four centred November 2012 VdM scans. The errors are statistical only. Length scale and bunch current corrections are applied.

LUCID_EventOR - σ_{vis} in November VdM scans

BCID	σ_{vis} [mb]			
	Scan 10	Scan 11	Scan 14	Scan 15
1	34.327 ± 0.046	34.771 ± 0.047	34.661 ± 0.048	34.878 ± 0.047
41	34.328 ± 0.041	34.913 ± 0.042	34.909 ± 0.044	34.854 ± 0.045
81	34.307 ± 0.042	34.811 ± 0.043	34.776 ± 0.044	34.813 ± 0.043
121	34.312 ± 0.039	34.651 ± 0.040	34.719 ± 0.042	34.762 ± 0.043
161	34.365 ± 0.042	34.594 ± 0.043	34.703 ± 0.045	34.855 ± 0.046
201	34.403 ± 0.042	34.581 ± 0.043	34.691 ± 0.044	34.726 ± 0.043
241	34.389 ± 0.045	34.661 ± 0.046	34.633 ± 0.048	34.708 ± 0.044
721	34.343 ± 0.045	34.723 ± 0.046	34.655 ± 0.047	34.729 ± 0.044
761	34.469 ± 0.040	34.606 ± 0.041	34.546 ± 0.042	34.780 ± 0.045
801	34.458 ± 0.042	34.624 ± 0.042	34.667 ± 0.043	34.762 ± 0.044
841	34.269 ± 0.036	34.670 ± 0.037	34.630 ± 0.039	34.747 ± 0.044
881	34.396 ± 0.041	34.599 ± 0.042	34.685 ± 0.043	34.735 ± 0.043
921	34.527 ± 0.043	34.658 ± 0.044	34.741 ± 0.046	34.748 ± 0.044
961	34.432 ± 0.042	34.646 ± 0.043	34.571 ± 0.044	34.837 ± 0.044
1581	34.241 ± 0.042	34.521 ± 0.043	34.593 ± 0.044	34.774 ± 0.045
1621	34.267 ± 0.041	34.593 ± 0.042	34.605 ± 0.043	34.865 ± 0.044
1661	34.398 ± 0.043	34.680 ± 0.044	34.777 ± 0.046	34.727 ± 0.046
1701	34.377 ± 0.041	34.586 ± 0.042	34.610 ± 0.044	34.799 ± 0.044
1741	34.459 ± 0.047	34.815 ± 0.048	34.672 ± 0.049	34.747 ± 0.046
1781	34.218 ± 0.040	34.675 ± 0.042	34.694 ± 0.043	34.740 ± 0.046
1821	34.373 ± 0.039	34.544 ± 0.040	34.634 ± 0.041	34.761 ± 0.047
2161	34.486 ± 0.044	34.700 ± 0.045	34.818 ± 0.046	34.733 ± 0.044
2201	34.420 ± 0.041	34.765 ± 0.042	34.767 ± 0.044	34.839 ± 0.046
2241	34.461 ± 0.047	34.640 ± 0.048	34.685 ± 0.049	34.782 ± 0.047
2281	34.295 ± 0.039	34.718 ± 0.040	34.699 ± 0.042	34.796 ± 0.043
2321	34.438 ± 0.041	34.569 ± 0.042	34.679 ± 0.043	34.891 ± 0.045
2361	34.283 ± 0.043	34.630 ± 0.045	34.810 ± 0.046	34.731 ± 0.041
2401	34.360 ± 0.045	34.670 ± 0.047	34.726 ± 0.048	34.746 ± 0.047
2881	34.383 ± 0.039	34.619 ± 0.040	34.614 ± 0.041	34.830 ± 0.044

Table B.6.: Bunch-by-bunch σ_{vis} for LUCID_EventOR obtained in the four centred November 2012 VdM scans. The errors are statistical only. Length scale and bunch current corrections are applied.

Bibliography

[1] The ATLAS Collaboration, "Observation of a new particle in the search for the Standard Model Higgs boson with the ATLAS detector at the LHC," *Physics Letters B*, vol. 716, no. 1, pp. 1 – 29, 2012.

[2] The CMS Collaboration, "Observation of a new boson at a mass of 125 GeV with the CMS experiment at the LHC," *Physics Letters B*, vol. 716, no. 1, pp. 30 – 61, 2012.

[3] M. Mangano, "LHC Lumi Days: Motivations and precision targets for an accurate luminosity determination at the LHC," 2011.

[4] J.-L. Caron, "LHC Layout." Sep 1997.

[5] M. Ferro-Luzzi, W. Herr, and T. Pieloni, "LHC bunch filling schemes for commissioning and initial luminosity optimization," Tech. Rep. CERN-LHC-Project-Note-415, CERN, Geneva, Jun 2008.

[6] L. Evans and P. Bryant, "LHC Machine," *Journal of Instrumentation*, vol. 3, no. 08, p. S08001, 2008.

[7] O. S. Brüning, P. Collier, P. Lebrun, S. Myers, R. Ostojic, J. Poole, and P. Proudlock, *LHC Design Report*. CERN.

[8] The ALICE Collaboration, "The ALICE experiment at the CERN LHC," *Journal of Instrumentation*, vol. 3, no. 08, p. S08002, 2008.

[9] The ATLAS Collaboration, "The ATLAS Experiment at the CERN Large Hadron Collider," *Journal of Instrumentation*, vol. 3, no. 08, p. S08003, 2008.

[10] The CMS Collaboration, "The CMS experiment at the CERN LHC," *Journal of Instrumentation*, vol. 3, no. 08, p. S08004, 2008.

[11] The LHCb Collaboration, "The LHCb Detector at the LHC," *Journal of Instrumentation*, vol. 3, no. 08, p. S08005, 2008.

[12] J. Pequenao, "Image of the ATLAS detector." Mar 2008.

[13] R. Achenbach *et al.*, "The ATLAS Level-1 Calorimeter Trigger," *Journal of Instrumentation*, vol. 3, no. 03, p. P03001, 2008.

[14] S. Mättig, "The Online Luminosity Calculator of ATLAS," Tech. Rep. ATL-DAQ-PROC-2011-009, CERN, Geneva, Jan 2011.

[15] The ATLAS Collaboration, "Image of the ATLAS luminosity detectors." 2012.

[16] V. Cindro *et al.*, "The ATLAS Beam Conditions Monitor," *Journal of Instrumentation*, vol. 3, no. 02, p. P02004, 2008.

[17] The ATLAS Collaboration, "Improved luminosity determination in pp collisions at sqrt(s) = 7 TeV using the ATLAS detector at the LHC," 2013.

[18] J. Bouchami *et al.*, "Estimate of the neutron fields in ATLAS based on ATLAS-MPX detectors data," *Journal of Instrumentation*, vol. 6, no. 01, p. C01042, 2011.

[19] U. Amaldi *et al.*, "The energy dependence of the proton-proton total cross-section for centre-of-mass energies between 23 and 53 GeV," *Physics Letters B*, vol. 44, no. 1, pp. 112 – 118, 1973.

[20] W. Herr and B. Muratori, "Concept of luminosity," *Proceedings of CERN Accelerator School*, 2003.

[21] C. Møller, "General Properties of the Characteristic Matrix in the Theory of Elementary Particles," *Danske Vidensk. Selsk. Mat.-Fys. Medd*, 1945.

[22] V. Khoze, A. Martin, R. Orava, and M. Ryskin, "Luminosity measuring processes at the LHC," *The European Physical Journal C - Particles and Fields*, vol. 19, pp. 313–322, 2001.

[23] V. Budnev, I. Ginzburg, G. Meledin, and V. Serbo, "The process $pp \to ppe^+e^-$ and the possibility of its calculation by means of quantum electrodynamics only," *Nuclear Physics B*, vol. 63, no. 0, pp. 519 – 541, 1973.

[24] J. Anderson, "LHC Lumi Days: Prospects for indirect luminosity measurements at LHCb," no. CERN-LHCb-PROC-2011-055.

[25] M. Schott, "LHC Lumi Days: Determination of Integrated Luminosity via W and Z Boson Production with the ATLAS Detector," no. arXiv:1108.2230.

[26] The ATLAS Collaboration, *ATLAS Forward Detectors for Measurement of Elastic Scattering and Luminosity.* Technical Design Report, Geneva: CERN, 2008.

[27] The TOTEM Collaboration, *Total cross-section, elastic scattering and diffraction dissociation at the Large Hadron Collider at CERN.* Technical Design Report, Geneva: CERN, 2004.

[28] G. Latino, "Hadron Collider Physics Symposium: Summary of Physics Results from the TOTEM Experiment," 2012.

[29] K. Hiller, "LHC Lumi Days: Status and prospects of ALFA Roman Pot Stations," 2011.

[30] M. Ferro-Luzzi, "Proposal for an absolute luminosity determination in colliding beam experiments using vertex detection of beam-gas interactions," *Nuclear Instruments and Methods in Physics Research Section A: Accelerators, Spectrometers, Detectors and Associated Equipment*, vol. 553, no. 3, pp. 388 – 399, 2005.

[31] V. Balagura, "Moriond QCD and High Energy Interactions: Luminosity measurement in the first LHCb data," 2010.

[32] S. Van der Meer, "Calibration of the Effective Beam Height in the ISR," Tech. Rep. CERN-ISR-PO-68-31, CERN, Geneva, 1968.

[33] C. Rubbia, "Measurement of the luminosity of $p\overline{p}$ collider with a (generalized) Van der Meer Method," Tech. Rep. CERN-p$\overline{p}$-Note-38, CERN, Geneva, Nov 1977.

[34] G. H. Hoffstätter, "8th European Particle Accelerator Conference: Luminosity scans at HERA," no. DESY-M-02-01-U.

[35] A. Drees and S. White, "1st International Particle Accelerator Conference: Vernier Scan Results from the First RHIC Proton Run at 250 GeV," 2010.

[36] V. Papadimitriou, "LHC Lumi Days: Luminosity determination at the Tevatron," no. arXiv:1106.5182.

[37] H. Burkhardt and P. Grafström, "Absolute Luminosity from Machine Parameters," Tech. Rep. CERN-LHC-PROJECT-Report-1019, 2007.

[38] S. M. White, *Determination of the Absolute Luminosity at the LHC*. PhD thesis, Orsay, Université Paris-Sud 11, Orsay, 2010.

[39] The ATLAS Collaboration, "Luminosity determination in pp collisions at $\sqrt{s} = 7$ TeV using the ATLAS detector at the LHC," *The European Physical Journal C*, vol. 71, pp. 1–37, 2011.

[40] F.-J. Decker, "Beam distributions beyond RMS," *AIP Conference Proceedings*, vol. 333, no. 1, pp. 550–556, 1995.

[41] L. Tomlinsen and S. Webb, "Modified gaussian definitions." Private communication.

[42] V. Balagura, "Notes on Van der Meer scan for absolute luminosity measurement," *Nuclear Instruments and Methods in Physics Research Section A: Accelerators, Spectrometers, Detectors and Associated Equipment*, vol. 654, no. 1, pp. 634 – 638, 2011.

[43] G. Anders *et al.*, "LHC Bunch Current Normalisation for the April-May 2010 Luminosity Calibration Measurements," *CERN-ATS-Note-2011-004 PERF*, Feb 2011.

[44] A. Alice *et al.*, "LHC Bunch Current Normalisation for the October 2010 Luminosity Calibration Measurements," *CERN-ATS-Note-2011-016 PERF*, Mar 2011.

[45] K. Fischer and R. Schmidt, "On the measurements of the beam current, lifetime and decay rate in the LHC rings." LHC-BCT-ES-0001, EDMS 359172.

[46] K. Unser, "Beam current transformer with d.c. to 200 MHz range," *IEEE Trans.Nucl.Sci.*, vol. 16, pp. 934–938, 1969.

[47] P. Odier, M. Ludwig, and S. Thoulet, "The DCCT for the LHC Beam Intensity Measurement," Tech. Rep. CERN-BE-2009-019, CERN, Geneva, May 2009.

[48] C. Barschel, M. Ferro-Luzzi, J.-J. Gras, M. Ludwig, P. Odier, and S. Thoulet, "Results of the LHC DCCT Calibration Studies," *CERN-ATS-Note-2012-026 PERF*, Feb 2012.

[49] G. Anders *et al.*, "Study of the relative LHC bunch populations for luminosity calibration," *CERN-ATS-Note-2012-028 PERF*, Feb 2012.

[50] C. Ohm and T. Pauly, "TIPP09: The ATLAS beam pick-up based timing system," 2009.

[51] G. Anders, "LHC Lumi Days: Using the BPTX for relative bunch population measurements," 2012.

[52] D. Belohrad, L. Jensen, O. Jones, M. Ludwig, and J. Savioz, "The LHC Fast BCT system: A comparison of Design Parameters with Initial Performance," Tech. Rep. CERN-BE-2010-010, CERN, Geneva, May 2010.

[53] A. Alici *et al.*, "Study of the LHC ghost charge and satellite bunches for luminosity calibration," *CERN-ATS-Note-2012-029 PERF*, Feb 2012.

[54] P. Hopchev, *Absolute luminosity measurements at LHCb*. PhD thesis, Grenoble U., Grenoble, 2011.

[55] The LHCb Collaboration, "Absolute luminosity measurements with the LHCb detector at the LHC," *Journal of Instrumentation*, vol. 7, no. 01, p. P01010, 2012.

[56] A. Jeff, M. Andersen, A. Boccardi, S. Bozyigit, E. Bravin, T. Lefevre, A. Rabiller, F. Roncarolo, C. P. Welsch, and A. S. Fisher, "Longitudinal density monitor for the LHC," *Phys. Rev. ST Accel. Beams*, vol. 15, p. 032803, Mar 2012.

[57] J. Wenninger and W. Kozanecki, "Orbit stability at IP1 during July 12 VdM scans." Private communication.

[58] The ATLAS Collaboration, "Luminosity Determination in pp Collisions at sqrt(s)=7 TeV Using the ATLAS Detector at the LHC," *Eur.Phys.J.*, vol. C71, p. 1630, 2011.

[59] S. Mättig, *Luminosity Measurements with the ATLAS Detector*. PhD thesis, University of Hamburg, 2012.

[60] M. Venturini and W. Kozanecki, "The Hourglass effect and the measurement of the transverse size of colliding beams by luminosity scans," *Conf.Proc.*, vol. C0106181, pp. 3573–3575, 2001.

[61] C. Barschel, *Precision luminosity measurement at LHCb with beam-gas imaging*. PhD thesis, RWTH Aachen University, III. Physikalisches Institut A, Aachen, Germany, 2013.

[62] W. Herr, "LHC Lumi Days: Beam-beam and dynamic beta," 2012.

[63] D. Berge, A. Hoecker, A. Messina, and G. Piacquadio, "Determination of absolute luminosity using a global fit to the Van der Meer data based on spatial vertex information." Private communication.

[64] J. Back *et al.*, "A User's Guide to the RooFitTools Package for Unbinned Maximum Likelihood Fitting," tech. rep., 2001.

[65] W. Verkerke and D. Kirkby, "The RooFit toolkit for data modeling," *arXiv:physics/0306116*, 2003.

[66] The ATLAS Collaboration, "Characterization of Interaction-Point Beam Parameters Using the pp Event-Vertex Distribution Reconstructed in the ATLAS Detector at the LHC," Tech. Rep. ATLAS-CONF-2010-027, CERN, Geneva, May 2010.

[67] The ATLAS Collaboration, "Public luminosity plots." 2012.

Acknowledgements

I would like to express my deep gratitude to the many people who have contributed to the completion of this thesis. I am extremely grateful to

- Prof. Dr. Hans-Christian Schultz-Coulon for giving me the opportunity to conduct my doctoral research under his supervision and for his tremendous support.
- Dr. Thilo Pauly for being my supervisor at CERN and for his contagious enthusiasm, guidance and persistent help.
- Dr. Witold Kozanecki for countless enlightening discussions on the theory of VdM scans, the systematic uncertainties impacting the calibration precision and on luminosity in general.

Furthermore I would like to thank everyone else in the CTP group at CERN, in the KIP ATLAS group at Heidelberg and in the ATLAS luminosity working group for the excellent company and support.

I am grateful to the Wolfgang-Gentner-Programme of the BMBF for making my stay at CERN and this work possible, in this context I would also like to acknowledge Dr. Michael Hauschild for always having an open door.

I would like to deeply thank Dr. Taylor Childers, Dr. Witold Kozanecki and Felix Müller for proofreading parts of the thesis.

And finally, to my wife Juliane, thanks for too many things to mention here, and to my children, Gregor and Eva, for enriching my life.